Issue 2 2018 | Volume 14

The Journal on Advanced Studies in Theoretical and Experimental Physics, including Related Themes from Mathematics

PROGRESS IN PHYSICS

"All scientists shall have the right to present their scientific research results, in whole or in part, at relevant scientific conferences, and to publish the same in printed scientific journals, electronic archives, and any other media." — Declaration of Academic Freedom, Article 8

ISSN 1555-5534

The Journal on Advanced Studies in Theoretical and Experimental Physics, including Related Themes from Mathematics

PROGRESS IN PHYSICS

A quarterly issue scientific journal, registered with the Library of Congress (DC, USA). This journal is peer reviewed and included in the abstracting and indexing coverage of: Mathematical Reviews and MathSciNet (AMS, USA), DOAJ of Lund University (Sweden), Scientific Commons of the University of St. Gallen (Switzerland), Open-J-Gate (India), Referativnyi Zhurnal VINITI (Russia), etc.

Electronic version of this journal:
http://www.ptep-online.com

Postal Address

Department of Mathematics and Science,
University of New Mexico,
705 Gurley Ave., Gallup, NM 87301, USA

ISSN: 1555-5534 (print)
ISSN: 1555-5615 (online)

Standard Address Number: 297-5092
Printed in the United States of America

April 2018 **Vol. 14, Issue 2**

CONTENTS

Information for Authors

Progress in Physics has been created for rapid publications on advanced studies in theoretical and experimental physics, including related themes from mathematics and astronomy. All submitted papers should be professional, in good English, containing a brief review of a problem and obtained results.

All submissions should be designed in LaTeX format using *Progress in Physics* template. This template can be downloaded from *Progress in Physics* home page http://www.ptep-online.com

Preliminary, authors may submit papers in PDF format. If the paper is accepted, authors can manage LaTeXtyping. Do not send MS Word documents, please: we do not use this software, so unable to read this file format. Incorrectly formatted papers (i.e. not LaTeXwith the template) will not be accepted for publication. Those authors who are unable to prepare their submissions in LaTeXformat can apply to a third-party payable service for LaTeX typing. Our personnel work voluntarily. Authors must assist by conforming to this policy, to make the publication process as easy and fast as possible.

Abstract and the necessary information about author(s) should be included into the papers. To submit a paper, mail the file(s) to the Editor-in-Chief.

All submitted papers should be as brief as possible. Short articles are preferable. Large papers can also be considered. Letters related to the publications in the journal or to the events among the science community can be applied to the section *Letters to Progress in Physics*.

All that has been accepted for the online issue of *Progress in Physics* is printed in the paper version of the journal. To order printed issues, contact the Editors.

Authors retain their rights to use their papers published in *Progress in Physics* as a whole or any part of it in any other publications and in any way they see fit. This copyright agreement shall remain valid even if the authors transfer copyright of their published papers to another party.

Electronic copies of all papers published in *Progress in Physics* are available for free download, copying, and re-distribution, according to the copyright agreement printed on the titlepage of each issue of the journal. This copyright agreement follows the *Budapest Open Initiative* and the *Creative Commons Attribution-Noncommercial-No Derivative Works 2.5 License* declaring that electronic copies of such books and journals should always be accessed for reading, download, and copying for any person, and free of charge.

Consideration and review process does not require any payment from the side of the submitters. Nevertheless the authors of accepted papers are requested to pay the page charges. *Progress in Physics* is a non-profit/academic journal: money collected from the authors cover the cost of printing and distribution of the annual volumes of the journal along the major academic/university libraries of the world. (Look for the current author fee in the online version of *Progress in Physics*.)

Birkeland Currents and Dark Matter

Donald E. Scott
Dept. of Electrical Engineering (Retired), University of Massachusetts, Amherst, Massachusetts, USA
E-mail: dascott3@cox.net

A straight-forward application of basic electrical definitions and one of Maxwell's divergence equations provide an extension of the Bessel function model of force-free, field-aligned currents (FAC). This extended model offers descriptions of the charge density, electric-field strength, velocity profile, and voltage profile, each as a function of radial value, r, within the cross-section of the FAC structure. The resulting model exhibits an obvious correspondence with the results of the Marklund convection process in plasma filaments. Most importantly, it shows that observed stellar velocity profiles in galaxies are now accurately predicted without invocations of Dark Matter, WIMPs, or MACHOs.

1 Introduction

Kristian Birkeland's hypothesis [1] that Earth's auroras are powered by electric charges flowing from the Sun was shown to be correct in the late 1960's [2]. Since that time there has been a growing interest in the exact structure of those streams. What are the precise shapes and physical properties of these currents that cascade down into Earth's polar regions? NASA calls them "magnetic flux-ropes". A more proper name is Birkeland Currents [3]. The general form of those tube-like flux-ropes is best visualized as being a set of concentric, counter- rotating, cylinders made up of various electric currents and magnetic fields. One mathematical description of these structures is called the "Bessel Function Model". Its derivation was initiated in 1950 by physicist Stig Lundquist [4,5]. This derivation was completed and its physical consequences further defined by Scott in 2015 [6].

2 Force-free plasmas are field-aligned

The mechanism by which each moving charge magnetically affects its neighbors is called the Lorentz magnetic force [7]. If these Lorentz forces can be reduced to zero-value everywhere through out the plasma, then the overall current will proceed placidly with increased structural integrity, and not be diverted from its original direction. If, at every point in the flow, the magnetic-flux, **B**, and the electric-current density, **j**, are aligned in the same direction (thus the adjective "field-aligned"), all disruptive Lorentz forces within the plasma will be eliminated and the system is then termed a "Force-Free, Field-Aligned Current" (FAC).

3 Basic properties of field-aligned currents

The Bessel function model of a FAC explicitly involves only two canonical variables: the magnetic-field, $\mathbf{B}(r)$, and electric current density $\mathbf{j}(r)$. The model requires these two vector quantities to be everywhere parallel (non-interacting). Cylindrical coordinates (with fixed unit vectors r, θ, z) are used to describe the resulting shape. Because the flow is assumed to be of unlimited extent in length and have a circular cross-section, the model assumes no variation of either **B** or **j** in the θ, or z directions. The mathematical results of this modeling process are:

$$B_z(r) = B_z(0)\, J_0(\alpha r)\,, \tag{1}$$

$$B_\theta(r) = B_z(0)\, J_1(\alpha r)\,, \tag{2}$$

$$j_z(r) = \frac{\alpha B_z(0)}{\mu}\, J_0(\alpha r)\,, \tag{3}$$

$$j_\theta(r) = \frac{\alpha B_z(0)}{\mu}\, J_1(\alpha r)\,, \tag{4}$$

$$B_r(r) = j_r(r) = 0\,, \tag{5}$$

where J_0 and J_1 are Bessel functions of the first kind and of order zero and one respectively. The physical consequences of these equations are: The magnetic-field, **B**, at any point inside the current stream, has two components, one in the axial, z direction (1), and one in the "wrap-around" or θ direction (2). The vector sum of these two orthogonal components at any point located at a distance r out from the central z-axis is the net resulting magnetic field vector, $\mathbf{B}(r)$. The same is true about the current density, **j**; it is made up of two orthogonal components (3) and (4) in the same way that **B** is.

Comparing expressions (1) and (3) shows that magnitudes B_z and j_z have the same shape except for a difference in scale (size). The same is true for B_θ and j_θ as seen in expressions (2) and (4). In general, both **B** and **j** take on parallel, concentric spiral shapes.

Expression (5) reveals that neither the magnetic-field nor current density component is radiated (nothing leaves the cylindrical flow in the outward — radial, r — direction). This preserves the structural integrity of the flow over extreme distances, z. A full derivation of these properties and equations (1) through (5) is contained in Scott's 2015 paper [6].

4 Extension of the Bessel function FAC model

The only physical quantities modeled in the original Bessel function FAC analysis are magnetic-field vector, **B**, and electric current density vector, **j**. But,if there are electric currents present, there must also be electric charges present to create those currents. If there are electric charges in a given region, there may also be electric-fields.

By extending the Bessel function FAC model, the goal of this paper is to determine:

- The scalar charge density profile, $\rho(r)$, that exists within the FAC.
- The electric-field vector, $E(r)$, that may result from this $\rho(r)$ in the FAC.
- The scalar voltage profile, $V(r)$, that may exist over any cross-section of the FAC.
- Whether the Bessel function FAC model is consistent with the Marklund Convection mechanism.
- The extent to which observed stellar rotational profiles in galaxies are explicable by physical properties of the FAC without invoking the presence of hypothetical dark matter.

5 Components of an electric current density

At every point within a FAC, a single current density vector, $\mathbf{j}(r)$, is assumed to exist. It is a vector quantity. Both the magnitude and the direction of this vector will vary only as the radial distance, r, of the point changes. There is no variation of current density or magnetic field with either z or θ.

A way to visualize this $\mathbf{j}(r)$ structure is the following: if one looks inward toward the central z-axis of the flow from any point, r,and then backs away, outward, with increasing distance from the axis, the net current density vector, $\mathbf{j}(r)$, will appear to rotate smoothly clockwise, and its magnitude will gradually decrease (as $1/\sqrt{r}$). This fact (the monotonic decrease of total current density with $1/\sqrt{r}$) is of significant importance in what follows. See figure 1.

The SI dimensional units of an electric current density, $\mathbf{j}(r)$, are Amperes per square meter. [i.e., the number of Amperes of current that are passing through a unit area determines the value of the "current density" there.]

1. The charge density, $\rho(r)$, describes how much charge is contained in a unit volume located at point r. Therefore its SI units are Coulombs per cubic meter (C/m^3).
2. The velocity, $\mathbf{v}(r)$, of this unit volume is the second factor. A one Ampere current is defined as being one Coulomb moving past an observation point each second. SI units of velocity are m/sec.

Therefore the current density at any point, r, is given by

$$\mathbf{j}(r) = \rho(r)\mathbf{v}(r)\,, \tag{6}$$

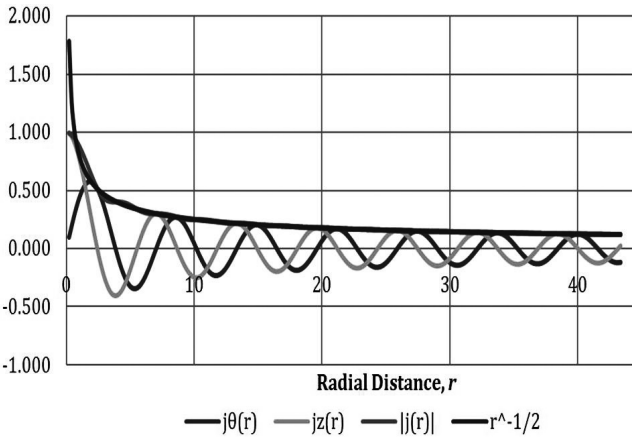

Fig. 1: Current density and its two components. The magnitude of the total current density varies as $1/\sqrt{r}$.

$$j = \frac{\mathrm{C}}{\mathrm{m}^3}\frac{\mathrm{m}}{\mathrm{s}} = \frac{\mathrm{C/s}}{\mathrm{m}^2} = \frac{\mathrm{A}}{\mathrm{m}^2}\,. \tag{7}$$

In expression 6, $\mathbf{j}(r)$ and $\mathbf{v}(r)$ are both vector quantities and, since $\rho(r)$ is a scalar, it follows that $\mathbf{j}(r)$ and $\mathbf{v}(r)$ are collinear (parallel). Thus the charge density, $\rho(r)$, is defined as being the ratio of the magnitude of the current density vector at point r divided by the magnitude of the velocity vector at that same point. Therefore

$$\rho(r) = \frac{|\mathbf{j}(r)|}{|\mathbf{v}(r)|}\,. \tag{8}$$

Note that in the numerator of (8) it is the *magnitude of the total vector sum* of the current density that is used. The vector components, $j_z(r)$ and $j_\theta(r)$ each vary with r with their oscillating Bessel function shapes, but the magnitude of their vector sum decreases smoothly with increasing radius as $1/\sqrt{r}$ (see figure 1). This value of the magnitude of the total current density, $|\mathbf{j}(r)|$, at every point within the FAC is obtained as the sum of its components, (3) and (4), described above. It is evident from that figure that the magnitude of the current density $|\mathbf{j}(r)|$ varies as $1/\sqrt{r}$.

$$|\mathbf{j}(r)| = \sqrt{j_z^2(r) + j_\theta^2(r)}\,. \tag{9}$$

In order to obtain an evaluation of the charge density, $\rho(r)$, in expression (8), it is necessary to obtain a valid expression for $|\mathbf{v}(r)|$.

6 Estimating the velocity profile of a FAC

It has been suggested [8] that galaxies form on and along cosmic Birkeland currents. Consistent with that hypothesis, we assume that the velocity profiles of stars rotating around a galaxy's center have a conformation similar to the FAC on which that galaxy formed. Galactic velocity profiles have

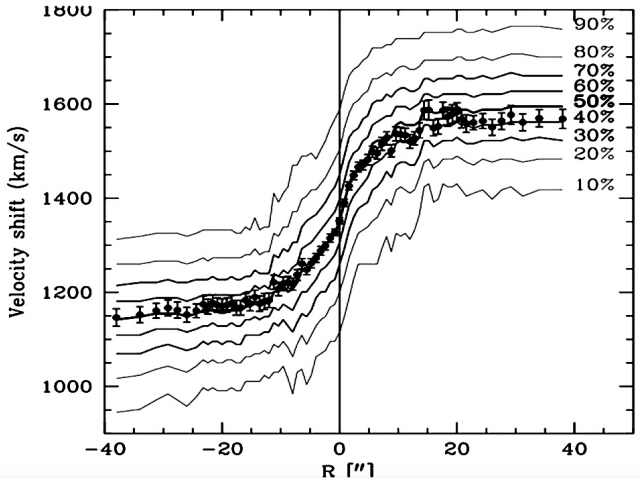

Fig. 2: Observed (measured) velocity profile of a typical galaxy. NGC 1620. [9]

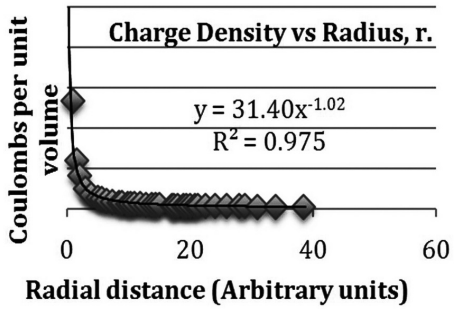

Fig. 3: Charge density produced by the known $|\mathbf{j}(r)|$ from the FAC model and the $|\mathbf{v}(r)|$ of the observed galaxy from (8).

been extensively measured both in the past and presently because of their being offered as evidence of the existence of dark-matter, e.g. figure 2.

If using a typical empirically obtained galaxy velocity profile, $|\mathbf{v}(r)|$, in expression (8) results in a realistic charge density, $\rho(r)$, this would constitute supporting evidence for this hypothesis of galaxy formation.

7 A sample stellar velocity profile $|\mathbf{v}(r)|$ for a typical galaxy

The data in figure 2 [9] was sampled (the abscissa and ordinate of each data point was recorded). This empirical data was incorporated into a spreadsheet database. In this way a data series for $|\mathbf{v}(r)|$ was obtained.

Then a numerical data series for $|\mathbf{j}(r)|$ as given by (9) (shown in figure 1) was also entered into the database. Expression (8) was used together with those data sequences for $|\mathbf{j}(r)|$ and $|\mathbf{v}(r)|$ to obtain the charge density, $\rho(r)$. The result is shown in figure 3.

Figure 3 indicates that the observed stellar rotation profile in this sample galaxy (figure 2) will be correctly produced by the Bessel function model FAC if its internal charge density varies with r as

$$\rho(r) = \frac{k}{r}\,. \tag{10}$$

8 Charge density determines the electric-field

One of Maxwell's equations describes the relationship between the electric charge density, $\rho(r)$, at any point, r, and the electric field, $\mathbf{E}(r)$, that diverges outward from any such point.

$$\nabla \cdot \mathbf{E}(r) = \frac{\rho(r)}{\epsilon}\,. \tag{11}$$

In this expression, $\rho(r)$ is the electric charge density at the point r and ϵ is the permittivity of the surrounding medium. Therefore the electric-field in a region (such as within this FAC) may be obtained by solving (11) using the $\rho(r)$ arrived at in (10).

The general form of the divergence operator in cylindrical coordinates is

$$Div\,\mathbf{E} = \nabla \cdot \mathbf{E}(r) = \frac{1}{r}\frac{\partial}{\partial r}(rE_r) + \frac{1}{r}\left(\frac{\partial E_\theta}{\partial \theta}\right) + \frac{\partial E_z}{\partial z}\,. \tag{12}$$

As before, it was assumed that, in a Birkeland current there is no variation of $\mathbf{E}$ with respect to axial distance z, nor with angular displacement θ, around that axis. There is no preferred location along the unboundedly long z-axis, and there is no angle, θ, around that axis that is preferred over any other. Using these simplifications in (12) and substituting into (11) yields

$$\frac{1}{r}\frac{\partial}{\partial r}\,(rE_r) = \frac{\rho(r)}{\epsilon}\,, \tag{13}$$

$$\frac{\partial}{\partial r}\,(rE_r) = \frac{r\rho(r)}{\epsilon}\,, \tag{14}$$

$$E_r = \frac{1}{\epsilon r}\int_0^r r\,\rho(r)\,dr\,. \tag{15}$$

Substituting (10) into (15) and integrating results in

$$E_r(r) = \frac{k}{\epsilon}\,. \tag{16}$$

Therefore the electric-field has a constant value across the entire cross-section of the FAC. The force per unit + charge is outward.

9 The voltage profile is determined by the electric-field, $E(r)$

Using the definition of the electric-field,

$$E_r(r) = -\frac{\partial V(r)}{\partial r}\,, \tag{17}$$

$$V(r) = -\int_0^r \frac{k}{\epsilon}\,dr = -\frac{kr}{\epsilon} + C. \tag{18}$$

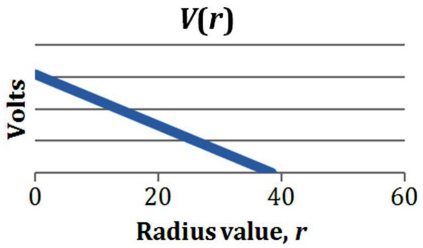

Fig. 4: Voltage profile of cross-section of a FAC.

The constant of integration, C, is chosen such that at the outer boundary of the FAC, $V(R) = 0$. The force per unit charge (16) thus creates a linear, uniformly decreasing voltage profile (18) across the FAC cross-section.

10 Marklund Convection

The voltage profile, $V(r)$, shown in figure 4 is fully consistent with the process known as Marklund Convection [10] wherein elements become sorted radially within a plasma filament according to their ionization potential. Neutral atoms diffuse into the FAC and become ionized due to a temperature gradient which is coolest at the center of the filament and hottest at its outer edge. This temperature gradient is caused by the voltage profile of figure 4 which accelerates ions outward to larger values of r. The turbulence (measured as temperature) of this radial flow at its periphery ionizes high V_i elements more easily than at the lower temperatures found near the center of the filament.

Hannes Alfvén [op. cit.] showed that elements with the lowest ionization potential are brought closest to the axis, and form concentric hollow cylinders whose radii increase with ionization potential. He said, "The drift of ionized matter from the surroundings into the rope means that the rope acts as an ion pump, which evacuates surrounding regions, producing areas of extremely low density."

In 2013 it was reported by Merrifield [11] that the outer rim of a counter-rotating galaxy (NGC 4550) had a collection of hydrogen-rich stars. This prompted him to say these outer stars were younger than the others: "Analysis of the populations of the two separate stellar components shows that the secondary disc has a significantly younger mean age than the primary disc, consistent with later star formation from the associated gaseous material. In addition, the secondary disc is somewhat brighter, also consistent with such additional star formation. However, these measurements cannot be self-consistently modeled by a scenario in which extra stars have been added to initially identical counter-rotating stellar discs, which rules out the Evans and Collett's elegant 'separatrix-crossing' model for the formation of such massive counter-rotating discs from a single galaxy, leaving some form of unusual gas accretion history as the most likely formation mechanism."

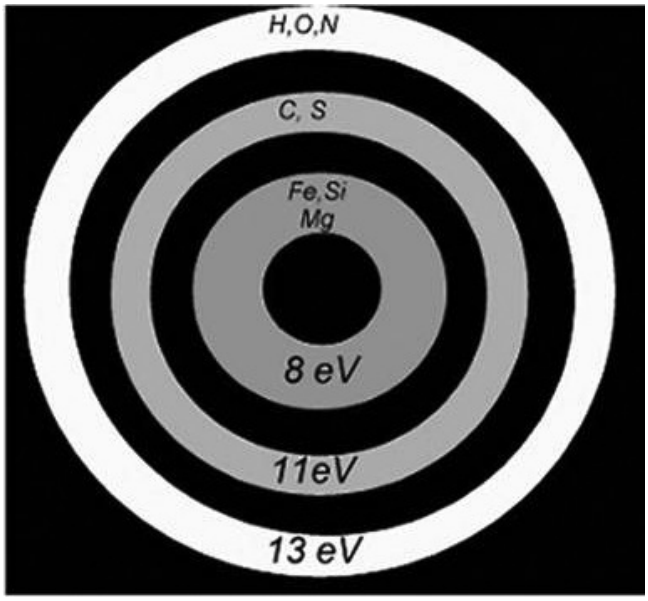

Fig. 5: Elements sorted in a plasma filament in order of their ionization voltage via the Marklund convection process.

Marklund convection stipulates that hydrogen and helium, two elements with the highest ionization voltage, will indeed be found at the outer rim of a plasma filament. The observation of this phenomenon by Merrifield suggests that a Birkeland current is likely to be responsible for the hydrogen-rich band that he discovered.

In 2012 Merrifield [12] had said in his explanation of the presence of these two different counter-rotating populations of stars in NGC 4550 that first, one uni-directional stellar disk formed and then "later on in its life, gas started flowing in, rotating around in the other direction". But, this leaves unanswered the questions of: from where did this new stream of oppositely rotating gas come? And this new gas, being highly collisional, would quickly smash into gas already there and fall into the galactic center. Thus, the question of "from where do the counter rotating stars come" remains unanswered.

In his earlier paper Scott [6] showed that the oscillations in the J_1 Bessel function that controls the spatial behavior of the current density component, j_θ, in a Birkeland Current produces counter-rotating bands in its cross-section (and presumably also in the galaxy it flows into). These bands are analogous to a multi-lane round-about (traffic circle) where adjacent lanes may be going in opposite directions without collisions.

11 Velocity profile predictions of the FAC Bessel model

If it is assumed that the charge density of a typical FAC is similar to the result of expression (10) and figure 3, $\left(\rho(r) \approx \frac{k_1}{r}\right)$, and also that $|\mathbf{j}(r)| = \frac{k_2}{\sqrt{r}}$ as given by the model, then it follows from (8)that the FAC's velocity profile ought to have the

following functional form:

$$|\mathbf{v}(r)| = \frac{|\mathbf{j}(r)|}{\rho(r)} = \frac{k_2}{k_1}\sqrt{r}\,. \tag{19}$$

Using the empirical data for our example galaxy (figure 2), we compare this actual observed $|\mathbf{v}(r)|$ data of the example galaxy with our derived velocity profile (19). See figure 6.

12 Results and Comments

One incidental result of this work strongly supports the existence of the voltage profile necessary for Marklund convection to occur in plasma filaments. See sections 9 and 10 above. However, the principal result presented here is the revelation of the actual cause of "anomalous" stellar rotation profiles in galaxies. Since the beginning of space research, most astrophysicists have asserted that electric fields, and currents, are not important in space phenomena [13]. Because of this rejection of electrical science and experimental plasma engineering, all efforts to explain why the outer stars in galaxies revolve around their galactic centers with velocities that, according to Newtonian dynamics, are too high have failed. This fruitless search has lasted for decades [14]. Invisible dark matter (DM) was first proposed by astronomers Jan Oort (1932) and Fritz Zwicky (1933). Subsequently several different types of DM have been hypothesized [15]:

- Cold collisionless dark matter (CCDM) [16];
- Warm dark matter (WDM) [17];
- Strongly self-interacting dark matter (SIDM) [18, 19, 20];
- Repulsive dark matter (RDM) [21];
- Self annihilating dark matter (SADM) [22];
- Fuzzy dark matter (FDM) [23];
- WIMPs Weakly interacting massless particles [24, 25];
- MACHOs Massive (astrophysical) compact halo objects [26, 27];
- Chameleon and Condensed Scalar Fields (not found as of 2015) [28, 29];
- Proposal to modify Newton's Laws [30].

This eighty-five year quest for a dark matter explanation of galactic stellar rotation profiles has produced only null results. Inserting a galaxy's charge density profile into the Birkeland Current Bessel function model [see expression (19)] now provides an elegantly simple answer shown in figure 6. Recently, scientific attention is becoming focused on discoveries of linkages among galaxies previously thought to be isolated from each other. Wide-field telescope observations of the remote universe, have revealed an immense string of galaxies about 300 million light-years long [31]. New research [32, 33, 34] suggests that galaxies are connected to one another with streams of hot thin ionized gas (hydrogen plasma) called the intergalactic medium or IGM.

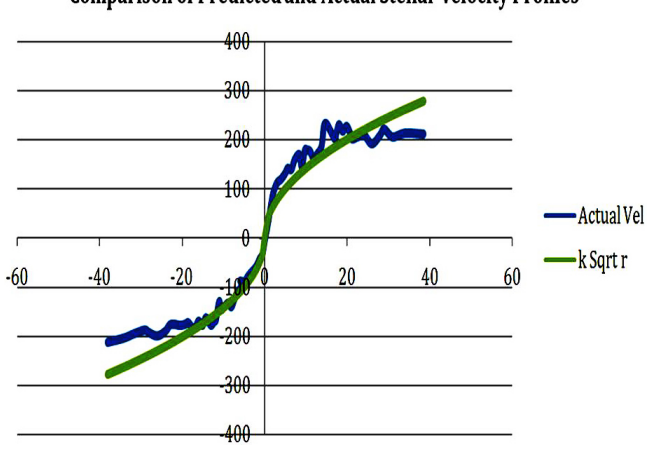

Fig. 6: Comparison of the example galaxy's measured velocity profile with the Bessel function model's Sqrt r profile.

Observations show a narrow filament, one million light-years long, flowing into a quasar, perhaps fueling the growth of the galaxy that hosts the quasar. Caltech's new Cosmic Web Imager has already detected one possible spiral-galaxy-in-the-making that is three times the size of our Milky Way [35].

An observation that is "anomalous" is one that is inconsistent with accepted hypotheses. In real science this requires the replacement of the falsified hypothesis, not an eighty-five year hunt for invisible entities that will preserve it. The work being presented here demonstrates that the root cause of the now vast collection of observed "anomalous" galactic stellar rotation profiles is the electrical nature of the Birkeland Currents on which those galaxies have been or are being formed.

Acknowledgment

The author wishes to express his sincere and heartfelt thanks to Dr. Jeremy Dunning-Davies and Dr. Michael Clarage for their crucial help in this effort.

Submitted on January 4, 2018

References

1. Birkeland K. The Norwegian Polaris Expedition 1902-1903. Vol. 1, Sect. 1, Aschehoug, Oslo, 1908.
2. Zmuda A. et. al. Characteristics Of Transverse Magnetic Disturbances Observed At 1100 Kilometers. *Auroral Oval Journal of Geophysical Research*, 1970, v.75, issue 25, 4757.
3. Alfvén H. Cosmic Plasma. Boston, D. Reidel, 1981, pages 16, 15–26, 36.
4. Lundquist S. Magneto-Hydrostatic Fields. *Arch. Fys.*, 1950, v. 2, 361–365.
5. Lundquist S. On the Stability of Magneto-Hydrostatic Fields. *Phys. Rev.*, 1951, v. 83(2), 307–311.
6. Scott D. Consequences Of The Lundquist Model Of A Force-Free Field Aligned Current. *Prog. Phys.*, 2015, v. 10(1), 167–178.
7. Peratt A. Physics Of The Plasma Universe. Springer-Verlag, New York, 1992, pages 43–44, 95, 103, 229. Repprinted in 2015.

8. ICRA, Astronomers find faint strings of galaxies inside empty space. International Center for Radio Astronomy Research, Perth, Western Australia. Published: March 11, 2014. http://www.astronomy.com/news/2014/03/astronomers-find-faint-strings-of-galaxies-inside-empty-space
9. NGC 1620, https://www.aanda.org/articles/aa/full/2004/35/aa0183-04/img97.gif
10. Marklund G. Plasma convection in force-free magnetic fields as a mechanism for chemical separation in cosmical plasma. *Nature*, 1979, v. 277, 370–371.
11. Johnson E., Merrifield M. Disentangling the Stellar Populations in the counter-rotating disc galaxy NGC 4550. *Monthly Notices of the Royal Astronomical Society*, 2013, v. 428(2), 1296–1302; arXiv: 1210.0535 [astro-ph.CO].
12. Merrifield M. Strange Galaxy (NGC 4550). https://www.youtube.com/watch?v=0oie90j989kδt=1sδlist=PLGJ6ezwqAB2a4RP8hWEWAGB9eT2bmaBsyδindex=40 Published 10/2012.
13. Scott D. Real Properties of Electromagnetic Fields and Plasma in the Cosmos. *IEEE Transactions on Plasma Science*, 2007, v. 35(4), 822–827.
14. Scoles S. How Vera Rubin Confirmed Dark Matter. *Astronomy*, October 4, 2016. http://www.astronomy.com/news/2016/10/vera-rubin
15. Ostriker J.P. and Steinhardt P. New Light on Dark Matter. *Science*, 2003, v. 300(5627), 1909–1913.
16. Ma C-P. Are Halos of Collisionless Cold Dark Matter Collisionless? *Phys. Rev. Letters*, 2004, v. 93(2), 021301.
17. Viel M., et al. Constraining warm dark matter candidates including sterile neutrinos and light gravitinos with WMAP and the Lyman-α forest. *Phys. Rev. D*, 2005, v. 71, 063534.
18. Wandelt BD. Self-Interacting Dark Matter, arXiv:astro-ph/0006344.
19. Zavala J. Constraining self-interacting dark matter with the Milky Way's dwarf spheroidals. *Monthly Not. RAS*, 2013, v. 431(1), L20–L24.
20. Hui L., Unitarity bounds and the cuspy halo problem. *Physical Review Letters*, 2001, v. 86, 3467.
21. Fan J. Ultralight Repulsive Dark Matter and BEC. *Physics of the Dark Universe*, 2016, v. 14, 1-126.
22. Natarajan P. Consequences of dark matter self-annihilation for galaxy formation, arXiv:0711.2302 [astro-ph].
23. Is Dark Matter "Fuzzy", Astronomy Now, Chandra X-ray Center press release, 2 May 2017.
24. Kochanek CS., White M. A Quantitative Study of Interacting Dark Matter in Halos. *The Astrophysical Journal*, 2000, v. 543(2).
25. Alcock C. The Dark Halo of the Milky Way. *Science*, 2000, v. 287(5450), 74–79.
26. Alcock C. et al. The MACHO Project: Microlensing Results from 5.7 Years of Large Magellanic Cloud Observations. *The Astrophysical Journal*, 2000, v. 542(1), 281–307.
27. Zeyher A. MACHOs may be out of the running as a dark matter candidate, Astronomy (2016); http://www.astronomy.com/news/2016/08/machos-may-be-out-of-the-running-as-a-dark-matter-candidate
28. Wilkinson R. The search for "dark matter" and "dark energy" just got interesting, Aug. 21, 2015. The Conversation: https://phys.org/news/2015-08-dark-energy.html; also: http://theconversation.com/the-search-for-dark-matter-and-dark-energy-just-got-interesting-46422.
29. Bohua L. Cosmological constraints on Bose-Einstein-condensed scalar field dark matter. *Phys. Rev. D*, 2014, v. 89, 083536.
30. Milgrom M. MOND — A Pedagogical Review. The XXV International School of Theoretical Physics "Particles and Astrophysics — Standard Models and Beyond", Ustron, Poland, September 10-16, 2001. arXiv: astro-ph/0112069
31. Palunas P. Giant Galaxy String Defies Models Of How Universe Evolved, NASA; https://www.nasa.gov/centers/goddard/news/topstory/2004/0107filament.html
32. Fesenmaier K. Astronomers unveil a distant protogalaxy connected to the cosmic web. https://phys.org/news/2015-08-astronomers-unveil-distant-protogalaxy-cosmic.html.
33. Coutinho B. The Network Behind The Cosmic Web. arXiv:1604.03236 [Astro-Ph.Co].
34. Gott J. The Cosmic Web (book). Princeton University Press, forthcoming Jun 2018.
35. Martin D.C. Intergalactic Medium Emission Observations with the Cosmic Web Imager. *Astrophysical Journal* v. 768(2), Art. No. 106. arXiv:1402.4809.

Can Cold Fusion Be Explained by Quantised Inertia?

M.E. McCulloch
Plymouth University, Plymouth, PL4 8AA, UK
E-mail: mike.mcculloch@plymouth.ac.uk

When electrolysis is performed using deuterium and a palladium cathode, more heat can be generated than can be explained by chemical processes, implying that deuterons are fusing but without the typical products of hot fusion (a phenomenon called Low-Energy Nuclear Reactions, LENR, or cold fusion). Fusion between deuterons usually requires temperatures of 100 MK to overcome the repulsive Coulomb forces. Here it is shown that a theory called quantised inertia predicts that in cracks in the metal with diameters less than 28 nm, the temperature is 27,000 K and mutual sheltering by the deuterons can produce an attractive radiation recoil force strong enough to push them together through their Coulomb barriers. This offers a potential explanation for cold fusion or LENR.

1 Introduction

Many attempts are underway to initiate nuclear fusion between atoms such as deuterium, releasing useful energy [1]. The main challenge is to overcome the Coulomb barrier: deuterons have a charge equal to the charge on the proton, and they repel each other with a force given by

$$F_C = \frac{q_P^2}{4\pi\varepsilon_0 d^2} \tag{1}$$

where $q_P = 1.6 \times 10^{-19}$ C is the charge on the proton, $\varepsilon_0 = 8.85 \times 10^{-12}$ $m^{-3}kg^{-1}s^4A^2$ is the permittivity of free space and d is the distance between the deuterons. Overcoming the Coulomb barrier between the two deuterons in this process usually requires a high momentum and therefore temperatures in excess of 100 MK which are thought to only be possible in gravitationally-confined systems such as the Sun or magnetically-confined fusion reactors.

This is why the results of Fleischmann and Pons [2] were so surprising. When they used a palladium cathode to electrolyse heavy water (containing deuterium) they noticed that more heat was given off than was possible from chemical processes, implying that fusion was occuring (so called cold fusion). The expected product of deuterium fusion: helium-4, was also produced, but the nuclear emissions (neutrons and gamma rays) expected from hot fusion were not seen and so cold fusion was dismissed by all but a small minority. However, over the years there have been many successful reproductions of the Pons-Fleischmann effect, or variations of it [3], and many unsuccessful ones as well, and the topic has been renamed LENR (Low-Energy Nuclear Reactions). A good summary is available in [4].

Aoyama [5], Storms [6], [7] and others have noted an intriguing pattern which is that a common feature to the successful experiments are the cracks or defects in the metals, which are on the order of the nanoscale.

McCulloch [8], [9], [10] has shown that a number of dynamical anomalies such as galaxy rotation and cosmic acceleration can be explained by a theory called quantised inertia which assumes that inertial mass is due to Unruh radiation (a radiation seen only by accelerating objects) when this radiation is made non-uniform in space by horizons. These horizons can be caused by acceleration (relativistic horizons) or they can be metal structures or cavities [11].

Another interesting anomaly down at the nuclear scale is that of [12] who showed that when the proton radius is measured with a orbiting muon rather than an electron, an extra unexplained binding energy is present. The muon orbits 200 times closer than the electron, and quantised inertia can explain 55% of this extra binding energy by assuming that the thermal Unruh radiation seen by the muon is blocked (sheltered) from the direction of the proton, leading to a net radiation pressure from outside its orbit, and a new attractive force [13]. Quantised inertia also predicts high temperatures within small horizons, for example in the early universe [14]. This may also apply to small metal cracks and so it may have relevence for LENR.

In this paper it is shown that quantised inertia predicts that cracks or defects in metals of 28 nm diameter or less should be hot enough to cause an attractive radiation recoil force on the deuterons strong enough to overcome their Coulomb repulsion. This suggests a mechanism for cold fusion and LENR.

2 Method & Results

The uncertainty principle of Heisenberg states that the uncertainty in momentum (Δp) times the uncertainty in position (Δx) must be greater than or equal to half the reduced Planck's constant

$$\Delta p \Delta x > \frac{\hbar}{2} \tag{2}$$

so that if the uncertainty in position (Δx) is reduced in a metal cavity of diameter D, then the momentum uncertainty (Δp) should increase. Quantised inertia assumes that this in-

crease in momentum can become real [15], and since $E = pc$ then a new energy becomes available, given by

$$\Delta E > \frac{\hbar c}{2D}. \tag{3}$$

For thermalised energy $E = \frac{3}{2}kT$ we can write an expression for temperature:

$$T > \frac{\hbar c}{3kD}. \tag{4}$$

Eq. 4 predicts that the temperature in tiny volumes is high. Figure 1 shows two deuterons (the black circles) close together inside a defect (the grey area) within a palladium lattice (the mottled area). If the temperature within the defect is as given in Eq. 4 then this radiation will be absorbed by each deuteron only on the side away from the other deuteron, assuming there is a mutual sheltering process (see the white radiation-free area in Figure 1) and so the absorption of this radiation will produce a radiation recoil force (see also [16]) that will push them together. This force is

$$F_R = \frac{P}{c} = \frac{\sigma T^4}{c} \tag{5}$$

where σ is the Stefan-Boltzmann constant and c is the speed of light. In order for this radiative force to cause the deuterons to fuse, it must be larger than the repulsive Coulomb force at the seperation where the attractive strong force can take over and fuse the two deuterons, a distance of $d_s = 1.6 \times 10^{-15}$ m. For this to happen, $F_R > F_C$ at distance d_s, and so using Eqs. 1 and 5, and using Eq. 4 for T we get

$$\frac{\sigma\left(\frac{\hbar c}{3kD}\right)^4}{c} > \frac{q^2}{4\pi\varepsilon_0 d_s^2}. \tag{6}$$

We can now predict the crack size D needed to produce a temperature high enough to cause fusion in this new way:

$$D < (4\pi\varepsilon_0\sigma)^{\frac{1}{4}}\, c^{\frac{3}{4}}\, \frac{\hbar}{3k}\sqrt{\frac{d_s}{q}} = 28 \text{ nm}. \tag{7}$$

Therefore, quantised inertia predicts that deuterons in cracks or defects in palladium of a size less than 28 nm will see temperatures of $\hbar c/3kD \geq 27000$ K and be pushed together by radiation in the crack strongly enough that their Coulomb barrier can be breached, causing fusion. Cracks of this size are present in palladium after being stressed [17].

3 Discussion

Quantised inertia also suggests a way to account for the lack of emitted neutrons in LENR. The inwards force on all particles in the defect may keep them confined, but it does not directly explain the lack of gamma rays.

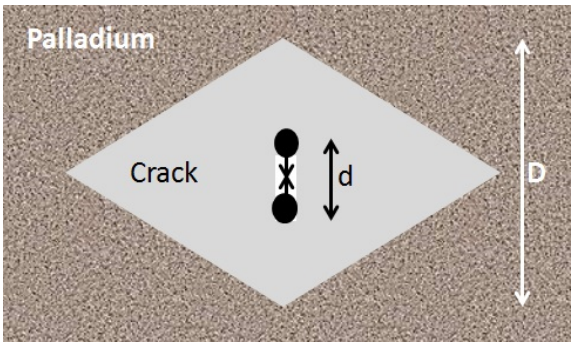

Fig. 1: A schematic showing two deuterons (the black circles) located a distance d apart within a crack/defect of width D (the grey area) in a palladium lattice (the mottled area). The metal radiates, and the mutual sheltering of the deuterons causes the white sheltered zone. The non-uniformity of the thermal radiation then forces the deuterons together (the arrows).

As a test, this theory predicts that metals with cracks or defects of size D should emit radiation of wavelength D. X-rays were indeed seen by [6] and [7] during LENR, with wavelengths in the nanometre range.

This mechanism also suggests a possible reason for sonoluminescence which similarly involves particles being confined to a small region, in this case a bubble collapsing to a size of 0.5 micron and attaining an apparent temperature of between 2300 K to 5100 K, as measured by the radiation given off (see [18]). Eq. 4 predicts a temperature of 1500K.

This application of quantised inertia predicts that a nanometal manufactured to have regular cracks of a size less than 28 nm should show far more uniform LENR.

4 Conclusion

When electrolysis is performed using heavy water (deuterium) and a palladium cathode, unexpected heat and Helium-4 can be generated indicating that nuclear fusion is taking place without the usual products of hot fusion (this is called LENR or cold fusion).

Quantised inertia predicts that deuterons in cracks or defects less than 28 nm in width should heat up enough that, through mutual sheltering, they feel an attractive radiation recoil force that overcomes their Coulomb barrier, allowing fusion. This is a possible explanation for cold fusion.

As a test this model predicts that a metal with cracks should emit radiation of a wavelength similar to the size of its cracks, and that a nanometal manufactured with cracks of size 28 nm or less should produce LENR more uniformly.

Acknowledgements

Many thanks to Bob McIntyre who pointed out that an earlier paper by the author on the proton radius anomaly [13] might also apply to LENR. Also many thanks to A. Dubourg and LENR pioneers Ed Storms and Russ George for advice.

Submitted on January 20, 2018

References

1. Clery D. ITER's $12 billion gamble. *Science*, 2006 v. 214, 5797.
2. Fleischmann M., Pons S. and Hawkins M. Elecrochemically induced nuclear fusion of deuterium. *J. Electroanal. Chem.*, 1989, v. 261, 301–308 and errata in v. 263, 187–188.
3. Kitamura A., Takayoshi N., Yu S., Akira T., Akito T., Reiko S., Yushi F. Anomalous effects in charging of Pd powders with high density hydrogen isotopes. *Phys. Letters A*, 2009, v. 373(35), 3109–3112.
4. Storms E.K. How basic behaviour of LENR can guide a search for an explanation. *J. Condensed Matter Nucl. Sci.*, 2016, v. 20, 1–39.
5. Aoyama T. et al. Highly reliable low-level neutron detection using 3He proportional counters. *Radioisotopes*, 1991, v. 40, 188.
6. Storms E.K. and Scanlan B. Detection of radiation emitted from LENR. ICCF-14. Conference on Condensed Matter Nuclear Science, 2008. Washington, DC.
7. Storms E.K. and Scanlan B. Nature of energetic radiation emitted from metal exposed to H2. *J. Condensed Matter Nucl. Sci.*, 2013, v. 11, 142–156.
8. McCulloch M.E. Modelling the Pioneer anomaly as modified inertia. *MNRAS*, 2007, v. 376, 338–342.
9. McCulloch M.E. Testing quantised inertia on galactic scales. *ApSS*, 2012, v. 342(2), 575–578.
10. McCulloch M.E. Galaxy rotations from quantised inerta and visible matter only. *Astrophys. Space Sci.*, 2017, v. 362, 149.
11. McCulloch M.E. Testing quantised inertia on the emdrive. *EPL*, 2015, v. 111, 60005.
12. Pohl R. et al. Laser spectroscopy of muonic deuterium. *Nature*, 2010, v. 466, 213.
13. McCulloch M.E. The proton radius anomaly from the sheltering of Unruh radiation. *Progress in Physics*, 2017, v. 13(2), 100–101.
14. McCulloch M.E. A toy cosmology using a Hubble-scale Casimir effect. *Galaxies*, 2014, v. 2, 81–88.
15. McCulloch, M.E. Quantised inertia from relativity and the uncertainty principle. *EPL*, 2016, v. 115, 69001.
16. Haslinger P., Jaffe M., Xu V., Schwartz O., Sonnleitner M., Ritsch-Marte M., Ritsch H. and Mueller H. Attractive force on atoms due to blackbody radiation. *Nature*, 2017, doi: 10.1038/s41567-017-0004-9.
17. Kim S., Lee H.-S., Jang B. and Cho S. Strain-controlled nanocrack formation in a Pd film on polydimethylsiloxane for the detection of low H2 concentrations. *J. Mater. Sci.*, 2016, v. 51(9), 4530–4537.
18. Brenner M.P., Hilgenfeldt S. and Lohse D. Single-bubble sonoluminescence. *Rev. Mod. Phys.*, 2002, v. 74(2), 425–484.

Global Scaling of Planetary Atmospheres

Hartmut Müller

E-mail: hm@interscalar.com

We derive a model of the stratification of planetary atmospheres as application of our scale-invariant model of matter as fractal chain system of oscillating protons and electrons. Model claims are verified by aerological, geophysical and planetological data.

Introduction

The vertical stratification of the Earth's atmosphere is caused by very different processes and it is a complex field of research. In general, air pressure and density decrease exponentially with altitude, but temperature, ionization and chemical composition have more complicated profiles. The standard division into troposphere, stratosphere, mesosphere, thermosphere, ionosphere and exosphere is based on satellite, airplane and ground measurements and considers aerodynamic, hydrodynamic, thermodynamic, chemical, electromagnetic, gravitational factors in their complex interaction.

New measurements of the atmospheres of solar system planets and moons over the past four decades from various spacecraft missions have been used to characterize the structure and dynamics of these atmospheric environments and to compare them to one another. A corresponding evolution of modeling tools occurs, from simple to complex frameworks.

Terrestrial modeling frameworks like HAMMONIA [1], ECHAM [2], IRI [3] and CMAM [4] of numerical modeling have been used to launch simulations [5] of other planetary upper atmospheres and ionospheres. The primary benefit of the Earth paradigm can be realized for other planetary upper atmospheres having similarities in their fundamental planetary parameters, basic processes and vertical domains (atmospheric layers).

In fact, stratification as atmospheric feature is associated not only with Earth, but occurs on any other planet or moon that has an atmosphere as well. Furthermore, stable atmospheric boundaries like tropopause, stratopause, thermopause and mesopause have similar vertical distributions at different celestial bodies in atmospheres of very different chemical compositions.

In this paper we apply our scale-invariant model [6] of matter as fractal chain system of oscillating protons and electrons and develop a general model of planetary atmospheric stratification that might help to understand the processes sustaining the observed stable atmospheric structures.

Methods

In [7] we have shown that the set of natural frequencies of a fractal chain system of similar harmonic oscillators can be described as set of finite continued fractions $\mathcal{F}$ (1), which are natural logarithms, where ω_{jk} is the set of angular frequencies and ω_{00} is the fundamental frequency of the set. The denominators are integer: $n_{j0}, n_{j1}, n_{j2}, \ldots, n_{jk} \in \mathrm{Z}$, the cardinality $j \in \mathrm{N}$ of the set and the number $k \in \mathrm{N}$ of layers are finite:

$$\ln(\omega_{jk}/\omega_{00}) = n_{j0} + \cfrac{z}{n_{j1} + \cfrac{z}{n_{j2} + \ddots + \cfrac{z}{n_{jk}}}} = [z, n_{j0}; n_{j1}, n_{j2}, \ldots, n_{jk}] = \mathcal{F}. \quad (1)$$

In the canonical form, the numerator z equals 1 and for finite continued fractions the distribution density of the eigenvalues reaches maxima near reciprocal integers 1, 1/2, 1/3, 1/4, ... which are the attractor points of the fractal set $\mathcal{F}$ of natural logarithms (fig. 1).

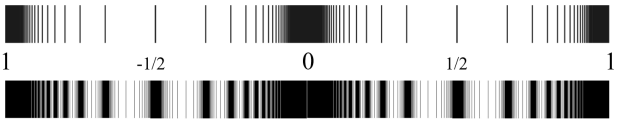

Fig. 1: The canonical form of $\mathcal{F}$ for $k = 1$ (above) and for $k = 2$ (below) in the range $-1 \leqslant \mathcal{F} \leqslant 1$.

Any finite continued fraction represents a rational number [8]. Therefore, all natural frequencies ω_{jk} in (1) are irrational, because for rational exponents the natural exponential function is transcendental [9]. This circumstance provides for high stability of eigenstates in a fractal chain system of harmonic oscillators because it prevents resonance interaction between the elements of the system [10]. Already in 1987 we have applied continued fractions of the type $\mathcal{F}$ as criterion of stability in engineering [11, 12].

In the case of harmonic quantum oscillators, the continued fractions $\mathcal{F}$ define not only fractal sets of natural angular frequencies ω_{jk}, angular accelerations $a_{jk} = c \cdot \omega_{jk}$, oscillation periods $\tau_{jk} = 1/\omega_{jk}$ and wavelengths $\lambda_{jk} = c/\omega_{jk}$ of the chain system, but also fractal sets of energies $\mathrm{E}_{jk} = \hbar \cdot \omega_{jk}$ and masses $\mathrm{m}_{jk} = \mathrm{E}_{jk}/c^2$ which correspond with the eigenstates of the system. For this reason, we call the continued fraction $\mathcal{F}$ the "fundamental fractal" of eigenstates in chain systems of harmonic quantum oscillators.

In the canonical form ($z = 1$) of the fundamental fractal $\mathcal{F}$, shorter continued fractions correspond with more stable eigenstates of a chain system of harmonic oscillators. Therefore, integer logarithms represent the most stable eigenstates (main attractor nodes).

Property	Electron	Proton
rest mass m	$9.10938356(11) \cdot 10^{-31}$ kg	$1.672621898(21) \cdot 10^{-27}$ kg
energy $E = mc^2$	0.5109989461(31) MeV	938.2720813(58) MeV
angular frequency $\omega = E/\hbar$	$7.76344071 \cdot 10^{20}$ Hz	$1.42548624 \cdot 10^{24}$ Hz
angular oscillation period $\tau = 1/\omega$	$1.28808867 \cdot 10^{-21}$ s	$7.01515 \cdot 10^{-25}$ s
angular wavelength $\lambda = c/\omega$	$3.8615926764(18) \cdot 10^{-13}$ m	$2.1030891 \cdot 10^{-16}$ m

Table 1: The basic set of physical properties of the electron and proton. Data taken from Particle Data Group [13]. Frequencies, oscillation periods and the proton wavelength are calculated.

As the cardinality and number of layers of the continued fractions $\mathcal{F}$ are finite but not limited, in each point of the space-time occupied by the chain system of harmonic quantum oscillators the scalar $\mathcal{F}$ is defined. Therefore, any chain system of harmonic quantum oscillators can be seen as source of the scalar field $\mathcal{F}$, the fundamental field of the system.

Normal matter is formed by nucleons and electrons because they are exceptionally stable quantum oscillators. In the concept of isospin, proton and neutron are viewed as two states of the same quantum oscillator. Furthermore, they have similar rest masses. However, a free neutron decays into a proton, an electron and antineutrino within 15 minutes while the life-spans of the proton and electron top everything that is measurable, exceeding 10^{29} years [13].

The exceptional stability of electron and proton predestinate their physical characteristics as fundamental units. Table 1 shows the basic set of electron and proton units that can be considered as a fundamental metrology (c is the speed of light in a vacuum, $\hbar$ is the Planck constant, k_B is the Boltzmann constant). In [14] was shown that the fundamental metrology (tab. 1) is compatible with Planck units [15].

We hypothesize that scale invariance of the fundamental field $\mathcal{F}$ calibrated on the physical properties of the proton and electron (tab. 1) is a universal characteristic of organized matter and criterion of stability. This hypothesis we have called 'global scaling' [16, 17].

Results

Within our scale-invariant model of matter [18], atoms and molecules emerge as eigenstates of stability in fractal chain systems of harmonically oscillating protons and electrons.

Andreas Ries [19] demonstrated that this model allows for the prediction of the most abundant isotope of a given chemical element. From this point of view, any physical body, being solid, liquid or gas can be seen as fractal chain system of oscillating molecules, atoms, ions, protons and electrons that generates its fundamental field $\mathcal{F}$.

Therefore, in the framework of our fractal model of matter, the fundamental field $\mathcal{F}$ affects any type of physical interaction, including the gravitational. In [20] we applied our model to the analysis of gravimetric and seismic characteristics of the Earth and could show [21] that our estimations correspond well with established empiric models of the Earth interior.

In this paper we demonstrate that the vertical sequence of stable atmospheric layers corresponds with the sequence of main equipotential surfaces of the fundamental field $\mathcal{F}$, not only at Earth, but also at Venus, Mars and Titan. Table 2 gives an overview of this correspondence.

The lowest layer of Earth's atmosphere is the troposphere where nearly all weather conditions take place. The average height of the troposphere is 20 km in the tropics, 12 km in the mid latitudes, and 7 km in the polar regions in winter [22]. Table 2 and fig. 2 show the correspondence of these tropospheric levels with the main equipotential surfaces [37; 2] = 7.5 km, [38; ∞] = 12 km and [38; 2] = 20 km of the fundamental field $\mathcal{F}$, calibrated on the electron wavelength.

At its lowest part, the planetary boundary layer (PBL), the troposphere displays turbulence and strong vertical mixing due to the contact with the planetary surface. The top of the PBL in convective conditions is often well defined by the existence of a stable capping inversion, into which turbulent motions from beneath are generally unable to penetrate [23]. The height of this elevated stable layer is quite variable, but is generally below 3 km. Over deserts in mid-summer under strong surface heating the PBL may rise to 4 - 5 km. In the temperate zones, it can be defined by the quite sharp decrease of aerosol concentration at the height of about 1600 m. Over the open oceans, but also at night over land, under clear skies and light winds, with a capping stratocumulus, the depth of the PBL may be no more than 600 m.

Table 2 and fig. 2 show the correspondence of the PBL features with the main equipotential surfaces [35; ∞] = 600 m, [36; ∞] = 1600 m and [37; ∞] = 4.5 km of the fundamental field $\mathcal{F}$, calibrated on the electron wavelength. It is noticeable that in 1992 Hess [24] already reviewed scaling aspects of the boundary layer.

Above the PBL, where the wind is nearly geostrophic, vertical mixing is less and the free atmosphere density stratification initiates. The jet stream flows near the boundary

BOUNDARY OF ATMOSPHERIC LAYER	ALTITUDE h, KM	$\ln(h/\lambda_e)$	$\mathcal{F}$
van Allen outer electron belt max density	13000	44.96	[45; ∞]
	8200		[44; 2]
	5000		[44; ∞]
van Allen inner proton belt max density	3000	43.50	[43; 2]
Earth exopause	1800	42.99	[43; ∞]
	1100		[42; 2]
Earth thermopause	650	41.97	[42; ∞]
	400		[41; 2]
Venus & Mars thermopause, Venus atmospheric entry	250	41.01	[41; ∞]
Earth atmospheric entry, Venus mesopause	150	40.50	[40; 2]
Earth & Titan mesopause, Venus tropopause, Mars stratopause & entry	90	39.99	[40; ∞]
Earth & Titan stratopause	55	39.50	[39; 2]
Titan tropopause	33	38.99	[39; ∞]
Earth tropic tropopause	20	38.49	[38; 2]
Earth temperate tropopause	12	37.98	[38; ∞]
Earth polar tropopause	7.5	37.51	[37; 2]
desert summer PBL inversion	4.5	37.00	[37; ∞]
continental PBL inversion	1.6	35.96	[36; ∞]
marine PBL inversion	0.6	34.98	[35; ∞]

Table 2: Altitudes of the boundaries of various atmospheric layers on Earth, Venus, Mars and Titan and their correspondence with main equipotential surfaces of the fundamental field $\mathcal{F}$, calibrated on the electron wavelength.

between the troposphere and the stratosphere. As altitude increases, the temperature of the troposphere generally decreases until the tropopause.

At the bottom of the stratosphere, above the tropopause, the temperature doesn't change much, but at the inverse layer at altitudes between 20 and 33 km the temperature increases from -50°C to 0°C. Then at the stratopause at 55 km altitude the temperature stabilizes. It is the boundary between two layers: the stratosphere and the mesosphere [25]. The ozone layer (ozonosphere) of the stratosphere absorbs most of the Sun's ultraviolet radiation and is mainly found at altitudes between 12 and 30 km, with the highest intensity of formation at 20 km height [26].

Table 2 and fig. 2 show the correspondence of the main stratosphere layers with the main equipotential surfaces [39; ∞] = 33 km and [39; 2] = 55 km of the fundamental field $\mathcal{F}$, calibrated on the electron wavelength.

Above the stratopause, in the mesosphere between 55 and 90 km altitude [27], the temperature decreases again, reaching about -100 °C at the mesopause [28]. This altitude coincides with the turbopause: above this level the atmosphere is of extremely low density so that the chemical composition is not mixed but stratified and depends on the molecular masses. Table 2 and fig. 2 show the correspondence of the mesopause with the main equipotential surface [40; ∞] = 90 km of the fundamental field $\mathcal{F}$, calibrated on the electron wavelength.

Above the mesopause, in the thermosphere, the (kinetic) temperature increases and can rise to 1000 °C (depending on solar activity) at altitudes of 250 km remaining quasi stable with increasing height. Due to solar radiation, gas molecules dissociate into atoms: above 90 km dissociate carbon dioxygen and dihydrogen, above 150 km dissociates dioxygen and above 250 km dissociates dinitrogen. Above 150 km, the density is so low that molecular interactions are too infrequent to permit the transmission of sound. Table 2 and fig. 2 show the correspondence of these thermosphere layers with the main equipotential surfaces [40; 2] = 150 km and [41; ∞] = 250 km of the fundamental field $\mathcal{F}$, calibrated on the electron.

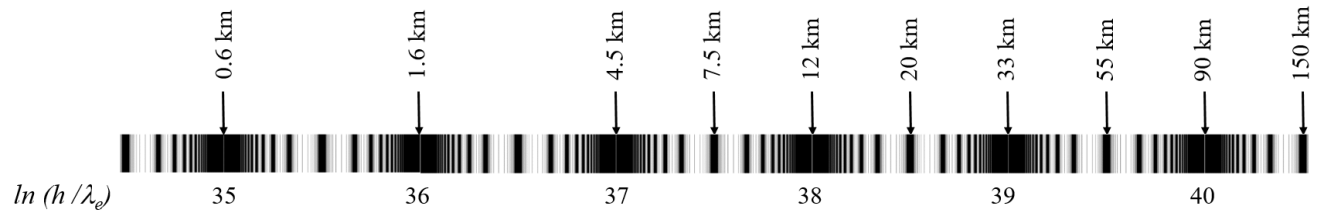

Fig. 2: The fundamental field $\mathcal{F}$ (natural logarithmic presentation) calibrated on the electron wavelength in the range $35 \leq \mathcal{F} \leq 40$ and the corresponding altitudes h in km.

The Karman line [29] is considered by the Federation Aeronautique Internationale (FAI) [30] as the border between the atmosphere and outer space, as altitude where the atmosphere becomes too thin to support aeronautical flight, since a vehicle at this altitude would have to travel faster than orbital velocity to derive sufficient aerodynamic lift to support itself. On Earth, atmospheric effects become noticeable during atmospheric entry of spacecraft already at an altitude of around 120 - 150 km, while on Venus atmospheric entry occurs at 250 km and on Mars at about 80 - 90 km above the surface. These heights mark also the bases of the anacoustic zones.

The location of the thermopause is near altitudes of 600 – 700 km and depends on solar activity [31]. Above starts the exosphere, where the atmosphere (mostly consisting of hydrogen atoms) thins out and merges with interplanetary space. This uppermost layer, until 13000 km observable from space as the geocorona, extends up to 100000 km. Table 2 and fig. 2 show the correspondence of the thermopause with the main equipotential surface [42; ∞] = 650 km of the fundamental field $\mathcal{F}$, calibrated on the electron wavelength.

The van Allen radiation belts [32] are features of Earth's magnetosphere. The inner belt consists of high energetic protons which reach their maximum concentration at altitudes of 3000 km. The outer belt consists of high energetic electrons with maximum concentration at altitudes of 13000 km.

While the outer belt maximum corresponds with the main equipotential surface [45; ∞] = 13000 km of the fundamental field $\mathcal{F}$, calibrated on the electron wavelength, the inner belt maximum corresponds with the equipotential surface [43; 2] = 3000 km that is the main equipotential surface [51; ∞] of the fundamental field $\mathcal{F}$, calibrated on the proton wavelength. In fact, the natural logarithm of the electron-to-proton wavelength ratio is approximately 7.5 and consequently, $\mathcal{F}$ calibrated on the proton will be shifted by 7.5 logarithmic units relative to the $\mathcal{F}$ calibrated on the electron:

$$\ln\left(\frac{\lambda_{\text{electron}}}{\lambda_{\text{proton}}}\right) = \ln\left(\frac{3.8615926764 \cdot 10^{-13}\ \text{m}}{2.1030891 \cdot 10^{-16}\ \text{m}}\right) \approx 7.5.$$

This circumstance, probably, can explain the high proton concentration at the inner belt.

Conclusion

The correspondence of the atmospheric stratification on the Earth, Venus, Mars and Titan with main equipotential surfaces of $\mathcal{F}$ demonstrates that the fundamental field affects very different types of physical interaction and is a strong confirmation of global scaling and our model of matter as fractal chain system of oscillating protons and electrons.

Probably, in future our model can be applied for estimation of the atmospheric stratification at ice giants like Uranus and Neptune and gas giants like Jupiter, Saturn and extrasolar planets as well.

Acknowledgements

I'm thankful to Leili Khosravi and Oleg Kalinin for valuable discussions.

Submitted on February 21, 2018

References

1. Schmidt H., Brasseur G. P. The response of the middle atmosphere to solar cycle forcing in the Hamburg Model of the neutral and ionized atmosphere. Space Science Reviews, 1–12, 2006.
2. Roeckner E. et al. Report No. 349. The atmospheric general circulation model ECHAM5. Max Planck Institute for Meteorology, Hamburg, 2003.
3. Bilitza D. et al. The International Reference Ionosphere 2012 – a model of international collaboration. Journal of Space Weather and Space Climat, 4, A07, 2014.
4. Grandpre J. de, Beagley S. R. et al. Ozone climatology using interactive chemistry: Results from the Canadian Middle Atmosphere Model. Journal of Geophysical Research, Vol. 105, No. D21, 475–491, 2000.
5. Bougher S. W. et al. Neutral Upper Atmosphere and Ionosphere Modeling. Space Science Reviews, 139: 107–141, 2008.
6. Müller H. Fractal Scaling Models of Natural Oscillations in Chain Systems and the Mass Distribution of Particles. *Progress in Physics*, vol. 3, 61–66, 2010.
7. Müller H. Fractal Scaling Models of Resonant Oscillations in Chain Systems of Harmonic Oscillators. *Progress in Physics*, vol. 2, 72–76, 2009.
8. Khintchine A.Ya. Continued fractions. University of Chicago Press, Chicago, 1964.
9. Hilbert D. Über die Transcendenz der Zahlen e und π. *Mathematische Annalen* 43, 216–219, 1893.
10. Panchelyuga V. A., Panchelyuga M. S. Resonance and Fractals on the Real Numbers Set. *Progress in Physics*, vol. 4, 48–53, 2012.

11. Müller H. The general theory of stability and objective evolutionary trends of technology. Applications of developmental and construction laws of technology in CAD. Volgograd, VPI, 1987 (in Russian).
12. Müller H. Superstability as a developmental law of technology. Technology laws and their Applications. Volgograd-Sofia, 1989 (in Russian).
13. Olive K.A. et al. (Particle Data Group), *Chin. Phys. C*, 38, 090001, 2016.
Patrignani C. et al. (Particle Data Group), *Chin. Phys. C*, 40, 100001, 2016.
14. Müller H. Scale-Invariant Models of Natural Oscillations in Chain Systems and their Cosmological Significance. *Progress in Physics*, vol. 4, 187–197, 2017.
15. Max Planck. Über Irreversible Strahlungsvorgänge. In: Sitzungsbericht der Königlich Preußischen Akademie der Wissenschaften. 1899, vol. 1, 479–480.
16. Müller H. Scaling as Fundamental Property of Natural Oscillations and the Fractal Structure of Space-Time. Foundations of Physics and Geometry. Peoples Friendship University of Russia, 2008 (in Russian).
17. Müller H. Scaling of body masses and orbital periods in the Solar System as consequence of gravity interaction elasticity. Abstracts of the XII. International Conference on Gravitation, Astrophysics and Cosmology, dedicated to the centenary of Einstein's General Relativity theory. Moscow, PFUR, 2015.
18. Müller H. Emergence of Particle Masses in Fractal Scaling Models of Matter. *Progress in Physics*, vol. 4, 44–47, 2012.
19. Ries A. Qualitative Prediction of Isotope Abundances with the Bipolar Model of Oscillations in a Chain System. *Progress in Physics*, vol. 11, 183–186, 2015.
20. Müller H. Gravity as Attractor Effect of Stability Nodes in Chain Systems of Harmonic Quantum Oscillators. *Progress in Physics*, vol. 1, 19–23, 2018.
21. Müller H. Quantum Gravity Aspects of Global Scaling and the Seismic Profile of the Earth. *Progress in Physics*, vol. 1, 41–45, 2018.
22. Danielson, Levin, and Abrams, Meteorology, McGraw Hill, 2003.
23. Garratt J. R. Review: the atmospheric boundary layer. Earth-Science Review, 37, pp. 89–134, 1994.
24. Hess G. D. Observations and scaling of the atmospheric boundary layer. Australian Meteorological Magazine. 41, 79–99 (1992).
25. Brasseur G. P., Solomon S. Aeronomy of the Middle Atmosphere. Chemistry and Physics of the Stratosphere and Mesosphere. ISBN-10 1-4020-3824-0, Springer, 2005.
26. Stolarski R. et al. Measured Trends in Stratospheric Ozone. Science, New Series, Vol. 256, Issue 5055, 342–349, 1992.
27. Holton J. R. The Dynamic Meteorology of the Stratosphere and Mesosphere. ISBN 978-1-935704-31-7, 1975.
28. Beig G., Keckhut P. Lowe R. P. et al. Review of mesospheric temperature trends. Rev. Geophys. 41 (4), 1015, 2003.
29. Karman T., Edson L. The Wind and Beyond. Little, Brown, Boston, 1967.
30. Cordoba S. F. The 100 km Boundary for Astronautics. Federation Aeronautique Internationale, 2011.
31. Beig G., Scheer J., Mlynczak M. G., Keckhut P. Overview of the temperature response in the mesosphere and lower thermosphere to solar activity. Reviews of Geophysics, 46, RG3002, July 2008.
32. Schaefer H. J. Radiation Dosage in Flight through the Van Allen Belt. Aerospace Medicine, Vol. 30, No. 9, 1959.

LETTERS TO PROGRESS IN PHYSICS

On the Possible Nature of Dark Matter and Dark Energy

Analtoly V. Belyakov
E-mail: belyakov.lih@gmail.com

It is assumed that the dark matter particle can be a structural unit of cosmological scale (superphoton) emitted by the active center of galaxies, analogous to a photon and ball lightning (macrophoton), which are structural units of micro- and macroscales. The low density, potential and temperature of superphotons make them invisible during astronomical observations, and their negative charge prevents the galaxies from approaching each other which can explain the phenomenon of dark energy. It is shown that the existence of superphotons together with the presence of cosmic rays indicates the conservation of the electric charge as a whole in cosmological scales. It is assumed that the superphoton, like a giant ball lightning with energy of 1.03×10^{17} J, could collide with the Earth which could explain the Tunguska phenomenon.

1 Introduction. On the natural range of the unit structural objects

In nature, as the scale changes, a regular range of certain single structural objects is observed. Let us consider them from the point of view of the mechanistic interpretation of J. Wheeler's geometrodynamic [1].

So, in the microcosm opposite charges (the proton and the electron, for example) are connected by a current vortex tube, forming as a whole a closed contour based on the *balance of magnetic and gravitational forces*; its structural unit is a *photon* (wave). The number of these units depends on the contour size, i.e. on the main quantum number n. The size of the "standard" contour $r_{st} = 1.25 \times 10^{-9}$ m. It contains approximately 137 photons (the inverse of the fine structure constant) [1,2]. In the limit, the contour can have one photon, that is, being identical to the photon itself.

A photon, like the contour itself, is a one-dimensional object; the photon does not exist at rest alone.

In the area of Earth's scales between charged macroobjects — a thundercloud and Earth — a linear lightning arises, also a kind of the current tube that generates a ball lightning, which, in turn, can be regarded as a structural unit. Calculation of the parameters of a typical ball lightning, provided that it has a mass close to the Planck mass (quasiparticle) is described in [3]. It is assumed that the ball lightning consists of many single elements — photons or of one long closed contour packed into a spherical shape, forming a *macrophoton*. A macrophoton is a multilayer spherical capacitor, i.e. a kind of two-dimensional object; the lifetime of a macrophoton is limited.

As for cosmic scales, there was shown in [4] that the structure of quasars can contain very long open vortex tubes with opposite currents carrying charges of different signs at the place of their rupture that resembles a kind of a superatom. Vortex tubes consist of vortex threads, which, supposedly, can be transformed into compact structural units — *superphotons* emitted by a quasar. Accordingly, continuing the analogy, the superphoton should be a three-dimensional object, and its lifetime is unlimited.

Indeed, galaxies form a homologous generation — from galaxies with a quasar in the center to galaxies with a black hole in the center. Thus, if a black hole absorbs matter, then the quasar as a white hole (the superdense body according to Ambartsumyan) generates matter. Then galaxies with quasars passing into a state of galaxies with black holes should radiate (to split off) part of its mass in the form of some particles.

2 On the possible super-photon structure

In [4] some parameters of the "standard" quasar were calculated, namely such ones, where the speed of the medium along the vortex tubes is that of "standard" proton-electronic contour. In particular, the following are defined:

quasar mass M, kg	4.76×10^{42}
quasar total energy E, J	9.61×10^{53}
length of the quasar vortex tube l, m	1.58×10^{21}
mass of 1 vortex threads of a quasar tube m_i, kg	5.10×10^{5}
number of unit threads const. the vortex tube, z	9.33×10^{36}

If the vortex thread forms a certain stable structure, then, obviously, certain balances of interactions must exist to maintain such a structure in equilibrium.

So, in [4] it is calculated that there is a *balance of the vortex tube kinetic energy and the electrostatic energy* of all single charges (not necessary electrons) placed along the vortex tube length, provided the distance between the vortex threads is equal to the size of the "standard" proton-electronic contour $r_s t$ and the maximum single charges number must be

$$z_{ie} = l/r_e = 5.6 \times 10^{35}, \quad (1)$$

where r_e is the electron classical radius (2.82×10^{-15} m).

At the same time, when the vortex threads are split off from the vortex tube, for a pair of threads a *balance of electric*

and magnetic forces must be realized that leads to a geometric mean [5]:

$$(l_i\, r_{st})^{1/2} = 7.52 \times 10^8 \text{ m}, \tag{2}$$

from which follows $l_i = 4.52 \times 10^{26}$ m.

Let us assume that this extended one-dimensional structure, i.e. a double vortex thread with charges of opposite signs can somehow be packed into a compact volume (similar to a double helix of DNA). In the most dense packing its linear dimension D can be estimated as

$$D = \left(l_i\, r_{st}^2\right)^{1/3} = 890\,\text{m}. \tag{3}$$

Further one can find other averaged parameters of the object — density, energy, charge and potential:

$$\rho = m_i/D^3 = 0.72 \times 10^{-3} \text{ kg/m}^3, \tag{4}$$

$$E_i = E/z = 1.03 \times 10^{17} \text{ J}, \tag{5}$$

$$Q_i = z_{ie}\, e_0 = 9.0 \times 10^{16} \text{ K}, \tag{6}$$

where e_0 is the electron charge,

$$U_i = E_i/Q_i = 1.14 \text{ V}. \tag{7}$$

It is important that in this volume the average distance between charges d is close to the size of the "standard contour" r_{st}, i.e. the *balance characteristic of the proton-electronic contour is also realized*. Really,

$$d = \left(D^3/z_{ie}\right)^{1/3} = 1.08 \times 10^{-9} \text{ m}. \tag{8}$$

Recall that all of the above calculated values are the result of using only the fundamental values.

Thus, when carrying out these balances, one can expect that such an object is stable and exists for a long time. Let's estimate this time, assuming that its object radiates as an absolutely black body and has a surface temperature close to the cosmic background radiation temperature $T = 2.7^\circ$ K (otherwise such objects would be seen in the process of astronomical observations). The power radiated by its surface is determined from the well-known formula:

$$N_i = T^4 \sigma S, \tag{9}$$

where σ is the Stefan-Boltzmann constant, equal to 5.67×10^{-8} $\text{Wm}^{-2}\,(^0\text{K})^{-4}$, and S is the sphere area of diameter D equal to πD^2. Substituting the data, we get $N_i = 7.5$ W and than the lifetime of the object is:

$$\tau = E_i/N_i = 1.37 \times 10^{16} \text{ sec or } 442 \text{ million years}, \tag{10}$$

which in order of magnitude corresponds to the lifetime of a quasar. Obviously, such an object can exist for a longer time, since it gradually dissipates its power and reduces the radiation temperature.

3 Superphoton as a candidate for the role of dark matter

A superphoton, unlike a ball lightning, has an insignificant density, potential, and surface temperature, hence it interacts with other bodies only *in a collision or through gravity*. Therefore, this object, inconspicuous against the background of relic radiation, can claim the role of the desired dark matter. The generality of its origin with ordinary baryonic matter is obvious; this possibility is also allowed in [6]. Let us assume that as the quasar "burns out" (before becoming into a galaxy), most of its mass is radiated in the form of superphotons (dark matter), and less of its mass remains in the form of a conventional galaxy (baryonic matter). Then the ratio of these masses should be close to the mass ratio of the quasar to the galaxy minus one. The calculated mass of the "standard" quasar is about five times greater than the baryon mass of our Milky Way galaxy [4]; for most other galaxies, less massive, this ratio is even greater. Thus, the ratio of the mass of superphotons to the mass of the average galaxy is generally consistent with the ratio of the dark matter mass to the baryonic matter mass. According to WMAP (Wilkinson Microwave Anisotropy Probe, 2003), the universe contains: dark matter of 22%, baryonic matter of 4%.

Apparently, young galaxies as the most massive and active should gradually lose their mass and reduce activity. This provision is consistent with the recently discovered of very massive young galaxies, about one billion years of age that produce stars with intensity much higher than the rate of star formation in our galaxy the Milky Way [7].

If the superphoton has kinetic energy relative to the point of origin (the quasar center) equal to its internal energy, then its relative velocity is equal to the circulation velocity of the medium along the vortex tube (for the "standard" quasar, $v = 448,000$ m/sec), i.e. it is close to the escape velocity. If particles are emitted mainly in the disk plane, then in this case their total velocity (peripheral velocity plus particle one) exceeds the escape velocity. Thus, during its lifetime (quasar activity), super-photons can move away from galaxies and fill the halo of galaxies, thereby playing the role of dark matter. In this case, in the most remote galaxies, i.e. the youngest from the point of view of observers, dark matter should be less. Indeed, this fact is established [8, 9].

According to the model, the super-photon is a cold and slowly moving formation that corresponds to the model of Cold dark matter. And just in favor of this particular model, the results obtained by a group of astronomers led by Vid Iršič, who analyzed the distribution of dark matter in the universe, based on observations of the lyman alpha radiation from distant galaxies obtained with the help of the Keck Telescope (Hawaii) and the Very Large Telescope Observatory (Chile) indicate [10].

Some features of the behavior of dark matter is not yet amenable to computer simulation: the cosmological models of formation and evolution of disk Galaxies, the distribution

of the density of dark matter in the galaxy disk (the problem of the central cusp), coplanarity dwarf galaxies-satellites relative to central galaxies, weak interaction of clouds of dark matter among themselves and others [11]. Therefore, it would be interesting to perform computer simulation, believing that dark matter particles have the properties of superphotons and move mainly in the plane of the galaxy disk.

The average density of particles in the form of superphotons in a galaxies interior, including the halo of diameter 10^5 light years, is very small, about one particle per cubic with a side of 0.5 million kilometers, which gives 5×10^{-24} g /cm^3. And, having the same charge, superphotons repel each other and can not form clusters. Therefore clouds of dark matter can freely intersect without significant interaction. At this density of dark matter and even several orders of magnitude greater (in the case of dark matter distribution mainly in the disc plane), its presence in the solar system can not be detected, which corresponds with the conclusions [12].

Let's try roughly to estimate the probability of a superphoton collision with the Earth. Let's assume that during our existence (1.3×10^{10} years) our galaxy has lost 4/5 of its baryonic matter due to the uniform radial radiation of superphotons on its inner spherical surface with a diameter of 10^5 light years. Then the number of super-photons from the total number of them ($\frac{1}{2} \times \frac{4}{5} \times 9.33 \times 10^{36} = 3.73 \times 10^{36}$) that fall per unit sphere area is 10^{-16} units per m^2 per year. Accordingly, 0.013 units per year (one superphoton at 77 years) fall on the globe cross-section or, in terms of unit charges, there are 1.46×10^{34} charges per year.

This is a reasonable value, but in reality this probability is much less and not only because of shading of the Earth by other cosmic bodies, dust, etc. The main reason is obviously the age of our galaxy and the presence of a black hole at its center; so we can assume that by now the radiation of superphotons is replaced by the reverse process — the absorption of matter by a black hole. Superhotons are carriers of namely negative charges, since there simultaneously are streams of positively charged particles — *cosmic rays*; at the same time negative and positive charges should be compensated in space as a whole. Obviously, there is some physical mechanism that separates the primary plasma into particles of opposite signs. Positive particles (mainly protons) form cosmic rays, and electrons are decelerated in interstellar magnetic fields (the material basis of the vortex tubes in our model).

The intensity of cosmic rays at the surface of the Earth is approximately one particle per cm^2 per second or 1.6×10^{26} particles per year on the entire Earth surface that is eight orders of magnitude less than the number of negative charges. However, the characteristic scale of the propagation of slow superphotons is the size of the galaxy (10^5 light years), and the similar propagation scale of cosmic rays, provided that they are uniformly distributed throughout the cosmic space, is the size of a larger structure — the cell of the cosmological network or the vault (10^7–10^8 light years). Thus, the unit density of particles in the corresponding volumes, i.e. cube ratio of linear scales, corresponds to the same order of magnitude.

4 On the forces of repulsion and dark energy

If the hypothesis of a superphoton is correct, then the galaxies periphery, where dark matter is mainly accumulated, should be surrounded by a distributed negative charge, which should counteract the "clumping" of galaxies between each other and also the walls of galactic vaults as a whole. Considering the masses and charges of galaxies at very great distances as point ones, it is possible to determine the magnitude of the equilibrium negative charge, at which electric forces are compared with gravitational ones:

$$Q = 2M\,(\pi\,\varepsilon_0\,\gamma)^{1/2}\,, \tag{11}$$

where ε_0 and γ are known electric and gravitational constants. Substituting the data, we find for the "standard" mass of the quasar $Q = 4.08 \times 10^{32}$ Coulomb.

Neither the charge distribution around galaxies nor its fraction responsible for the repulsive force between them is known. Therefore, for a rough estimate of the smallest value of the acting charge it suffices to restrict oneself to only the fraction of superphotons enclosed in a single spherical layer along the halo periphery, and — in the superphotons themselves — to a single spherical layer of negative charges along the periphery of superphotons. It was previously calculated that in the halo volume of 10^5 light years in size, the superphoton occupies the cell of 5×10^8 m; then, based on the areas ratio, one can find that 1.13×10^{25} superphotons can be placed in a single peripheral layer of the halo. Similarly, bearing in mind the dimensions of the superphoton D and the standard contour r_{st}, one can find that 1.59×10^{24} charges can be placed in the peripheral layer of the superphoton. Thus, the effective minimum charge of the "standard" galaxy will be $1.13 \times 10^{25} \times 1.59 \times 10^{24} \times e_0 = 2.87 \times 10^{30}$ Coulomb or 0.7% of the equilibrium charge. This is already an appreciable value; therefore, with more number of active charges, for example, with the expansion of the halo surface, the repulsive forces between galaxies can increase up to exceeding them above the forces of gravitational attraction.

So, if this hypothesis is correct, then in the space between galaxies and their clusters the electric field also acts, and the electrostatic repulsive forces beyond the galaxies have the same distance dependence as the gravitational ones, i.e. inverse quadratic form. This is consistent with the opinion of some researchers that "the physical nature of dark energy is determined by the interaction of gravitation and electroweak forces" [13]. These forces manifest themselves as antigravity, which in total can be interpreted as a *modification of the theory of gravity at extremely long distances and cosmological durations* [6], which is one of the explanations of dark energy accepted to date.

Conclusion

Thus, the super-photon, bearing in mind its properties, may turn out to be the desired dark matter or the missing substance of the universe. Its existence as a carrier of negative charges is indirectly confirmed in the existence of cosmic rays — carriers of positive charges that correspond to the condition of the charge conservation in the universe as a whole. In the case of correctness of the model presented, the problem of dark matter and dark energy finds the most rational explanation: dark matter (superphotons having a negative charge) is a product of the evolution of ordinary matter, and dark energy (repulsive forces) is the property of dark matter.

Of course, the superphoton is such a "particle" that clearly does not meet the expectations of researchers studying dark matter. Perhaps direct evidence of the existence of superphotons can be detected by observations during their interaction with the Sun or against the background of the Sun's disk, the probability of which is four orders of magnitude higher than when super-photons interact with the Earth.

There is only one event that could be explained by the collision of the superphoton with the earth — this is the Tunguska phenomenon. Indeed, the superphoton as the analog of a giant ball lightning with an energy of 1.03×10^{17} J, in size of 890 m and moving at cosmic speed could produce the specific effects of the Tunguska catastrophe, including those that are not explained by the currently dominant meteorite hypothesis [14].

Submitted on December 22, 2017

References

1. Belyakov A.V. Charge of the electron, and the constants of radiation according to J. A. Wheeler's geometrodynamic model. *Progress in Physics*, 2010, v. 6, issue 4, 90–94.
2. Belyakov A.V. Macro-analogies and gravitation in the micro-world: further elaboration of Wheeler's model of geometrodynamics. *Progress in Physics*, 2012, v. 8, issue 2, 47–57.
3. Belyakov A.V. On the nature of ball lightning. *Progress in Physics*, 2016, v.12, issue 3, 276–279.
4. Belyakov A.V. Are quazars white holes? *Progress in Physics*, 2017, v.13, issue 1, 7–10.
5. Belyakov A.V. Evolution of stellar objects according to J. Wheeler's geometrodynamic concept. *Progress in Physics*, 2013, v.9, issue 1, 25–40.
6. Lukash V.N., Rubakov V.A. Dark energy: myths and reality. *Physics-Uspekhi*, March 2008, v.178, issue 3, 301–308.
7. Discovered: Fast-growing galaxies from early universe. Carnegie Institution for Science, Public Release: 24 May 2017.
8. Swinbank M. Astrophysics: distant galaxies lack dark matter. *Nature*, 16 March 2017, v.543, 318–319.
9. Genzel R. et al. Strongly baryon-dominated disk galaxies at the peak of galaxy formation ten billion years ago. *Nature*, 16 March 2017, v. 543, 397–401.
10. Iršič V. et al. First constraints on fuzzy dark matter from Lyman-α forest data and hydrodynamical simulations. *Physical Review Letters*, 2017, v.119, 031302; arXiv: 1703.04683.
11. Khoperskov S.A., Shustov B.M., Khoperskov A.V. The interaction of dark matter cusp with the baryon component in disk galaxies. arXiv: 1204.4917 [astro-ph.CO].
12. Pitjev N.P., Pitjeva E.V. Constraints on Dark Matter in the Solar System. arXiv: 1306.5534 [astro-ph.EP].
13. Chernin A.D. Dark energy and universal antigravity. *Physics-Uspekhi*, 2008, v.178, issue 3, 267–300.
14. Bronshten V.A. Tunguska meteorite: the history of the study. Moscow, Selyanov A. D. Publisher, 2000.

Kinetic Theory: Flatlining of Polyatomic Gases

Kent W. Mayhew

68 Pineglen Cres., Ottawa, Ontario, K2G 0G8, Canada. E-mail:Kent.Mayhew@gmail.com

By redefining a gas' kinetic energy as translational plus rotational, an alternative kinetic theory was disclosed by this author that was a superior fit with empirical findings than the accepted kinetic theory. This alternative kinetic theory's fit for monatomic, diatomic and triatomic gases is exceptional, however the same cannot be said of large polyatomic gases. Accordingly, a new consideration called "*flatlining*" is proposed in order to explain the discrepancy between theory and the known empirical finding for heat capacities of large polyatomic gases.

1 Introduction

Traditionally accepted kinetic theory is based upon equipartition and degrees of freedom [1,2,3]. Mathematically speaking equipartition uses the concept that a gaseous molecule with n'' atoms has $3n''$ degrees of freedom (f), [4,5] i.e.:

$$f = 3n''. \tag{1}$$

This leads to the isometric molar heat capacity (C_v) for large polyatomic gases being

$$C_v = \frac{3}{2} n'' R \tag{2}$$

where $n"$ signifies the *polyatomic number* i.e. the number of atoms in each gas molecule. Numerous explanations for traditional kinetic theory's failure in properly describing empirically determined heat capacities, have been proposed [1,6-10]. Interestingly, Einstein thought that such failures in explaining empirical findings demonstrated the need for quantum theory [11-12].

This author proposed a new alternative kinetic theory [1]. The basis of this alternative theory was that the surrounding walls molecule's mean vibrational energy, as defined by (kT), is continually pumped onto the gaseous molecules that they surround. Where (k) is Boltzmann's constant and (T) is the absolute temperature.

After numerous impacts between the gaseous molecules and walls, the above pumping results in the total kinetic energy ($E_{kT(t,r)}$) of an N-molecule monatomic gas being defined by [1]:

$$E_{kT(t,r)} = \frac{3}{2} NkT. \tag{3}$$

Traditional kinetic theory considers that the kinetic energy as defined by eqn (3) represents purely translational energy.

In terms of this author's alternative kinetic theory, the above stated total kinetic energy consists of the gas' translational plus its rotational energy [1]. Interestingly, this author's theory is a superior fit with various heat capacities studies for gases [1,13-18], when compared to accepted theory.

In order to better understand, consider that you hit a tennis ball with a suitable racquet. If the ball impacts the racquet's face at a 90 degree angle then the ball will have significant translational energy in comparison to any rotational energy.

Conversely, if the ball impacts the racquet at an acute angle, although the same force is imparted onto that ball, the ball's rotational energy can be significant in comparison to its translational energy. The point becomes, that both the translational and rotational energy, are due to the same impact [1].

Now apply the above macroscopic considerations to the microscopic world. When vibrating wall molecules pump their mean vibrational energy onto the gas molecules that they surround it, it only makes sense that this results in both translational and rotational energy of the gas [1].

This author also pointed out that all kinetic theory only holds for sufficiently dilute gases because the predominate energy exchange is due to gas-wall molecule collisions, where wall molecules that act as massive energy pumps, i.e. gas molecules tend to take on the wall's energy with every gas-wall collision [1]. However this would not necessarily be the case for gases that are not sufficiently dilute i.e. gases where inter-gas molecular collisions are the dominate interaction [1].

This author has further asserted [1,19,20] that inter-gas molecular collisions tend to obey conservation of momentum, rather than adhere to kinetic theory. And, when inter-gas collisions dominate over gas-wall collisions then kinetic theory, the ideal gas law, Avogadro's hypothesis, Maxwell's distributions/velocities etc. all start to lose their validity [1].

For a system of diatomic gas molecules, the wall molecules still pass the same mean kinetic energy onto the diatomic gas molecule's center of mass with each collision. Therefore the diatomic gas' kinetic energy is still defined by eqn (3) [1].

The diatomic gas molecule's vibrational energy would be related to the absorption and/or emission of its surrounding blackbody/thermal radiation at temperature (T). The vibrational energy (E_v) of an N-molecule diatomic gas in a closed system becomes [1]

$$E_v = NkT. \tag{4}$$

And the total energy (E_{tot}) for an N molecule diatomic gas becomes [1]

$$E_{tot} = E_{kT(t,r)} + E_v = \frac{3}{2}NkT + NkT = \frac{5}{2}NkT. \quad (5)$$

Similarly, for N molecules of $n"$-polyatomic gas, the total vibrational energy is [1]

$$E_v = (n'' - 1)NkT. \quad (6)$$

And, the total energy (E_{tot}) for the polyatomic gas molecule becomes [1]:

$$E_{tot} = E_{kT(t,r)} + E_v = \frac{3}{2}NkT + (n'' - 1)NkT. \quad (7)$$

Hence,

$$E_{tot} = \left(n'' + \frac{1}{2}\right)NkT. \quad (8)$$

Dividing both sides by temperature and rewriting in terms of per mole: (N=6.022×10^{23}), equation (8) becomes [1]:

$$\frac{E_{tot}}{T} = Nk\left(n'' + \frac{1}{2}\right) = R\left(n'' + \frac{1}{2}\right). \quad (9)$$

For most temperature regimes, the heat capacity of gases remains fairly constant, hence equation (9) can be rewritten in terms of the isometric molar heat capacity (C_v) [1], i.e.

$$C_v = R\left(n'' + \frac{1}{2}\right). \quad (10)$$

The difference between molar isobaric heat capacity (C_p) and molar isometric heat capacity (C_v) for gases is the ideal gas constant (R). Therefore, a gas's isobaric heat capacity C_p becomes

$$C_p = R\left(n'' + \frac{1}{2}\right). \quad (11)$$

Interestingly this author realized that the above difference between molar heat capacities allows for a relationship between the ideal gas constant (R) and the ability of a mole of gas molecules to do work against a gravitational field [1, 20-21], as a function of temperature.

Based upon equations (10) and (11) the gas's molar specific heats were plotted against its polyatomic number ($n"$) as is shown by Fig. 1 and compared to the traditional accepted values for large polyatomic gases as given by eqn (2). Note the empirical data used in plotting Fig. 1 can be found in the Tables (1) and (2) provided in this author's previous paper [1] concerning kinetic theory.

Moreover, there was a discrepancy, between our model and empirical findings for relatively large polyatomic gases. It becomes a goal of this paper to provide a plausible explanation for the moderate discrepancy between this author's plots based upon equations (10) and (11) and the accepted empirical findings for large polyatomic molecules i.e. those whose polyatomic number is greater than four ($n"$> 4).

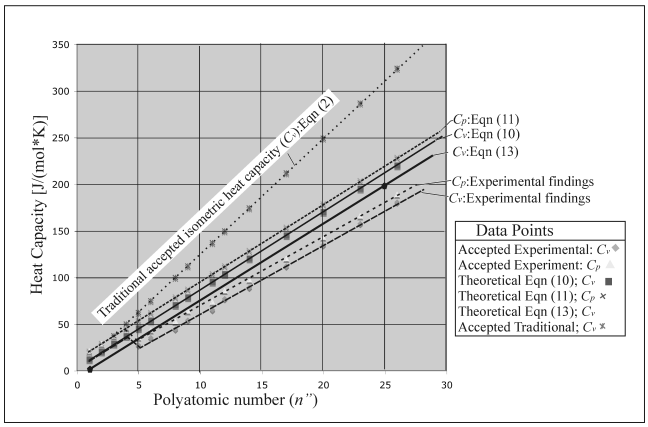

Fig. 1: Empirical versus theoretical heat capacities.

2 Flatlining

Why does the discrepancy exist for $n"$> 4? Let us consider that the gas molecule's size influences the exchange of kinetic energy (translational plus rotational) with the wall molecule's vibrational energy. How do we model this?

Consider the small monatomic gas molecule hitting the wall at location C, in Fig 2. Here the wall molecule is moving outward from the wall thus instantly imparting momentum, hence pumping its kinetic energy onto the gas molecule during the collision.

Next consider the gas molecule hitting the wall at location B. The wall molecule and gas molecule are initially moving in the same direction, i.e. both into the wall. However, since the wall molecule is vibrating at a very high frequency then within a fraction of a nanosecond, the wall molecule will start moving in the opposite direction. At this point the wall molecule imparts its momentum hence imposes kinetic energy (translational plus rotational) onto the impacting gas molecule.

Understandably, small gas molecules will tend to interact cleanly with the wall molecules, i.e. the significantly larger vibrating wall molecules cleanly pumps/imposes their mean vibrational energy directly onto the much smaller gas molecules. Seemingly, this is not the case for larger mole-cules. Perhaps vibrating wall molecules simply cannot clean-ly pump kinetic energy onto the larger gas molecules.

It can be envisioned that elongated linear gas molecules and/or large gas molecules tend to "*flatline*" against the wall, as is illustrated in Fig 2 at location A. The implication being that such large and/or elongated gas molecules tend to strike two or more (several) vibrating wall molecules at an instant, when some wall molecules are moving inwards, while their neighboring wall molecules are moving outwards, with respect to the wall as a whole. Note: The motions of the molecules are indicated by the arrows in Fig. 2.

Clearly the above should alter the dynamics of any kine-

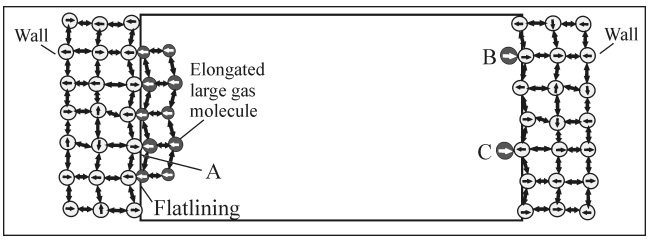

Fig. 2: Shows an elongated linear gas molecule flatlining against a wall at location A and the relative motions of the wall's molecules or atoms plus the relative motions of the gas' atoms. Also shown are smaller gas molecules hitting the wall at locations B and C.

matic energy exchange! The expectation is that a large polyatomic gas molecule's mean kinetic energy would no longer be simply defined in terms of the vibrating wall molecule's mean energy! Furthermore, the expectation is that polyatomic gases still interact with any surrounding blackbody/thermal radiation, thus continually striving for thermal equilibrium.

Consider that the primary energy exchange is between large polyatomic gases and their surroundings is with their surrounding blackbody/thermal radiation. The total energy (E_{tot}) imparted onto the gas molecule becomes the purely vibrational energy as defined by eqn (6). Accordingly:

$$\frac{E_{tot}}{T} = (n'' - 1)Nk. \tag{12}$$

Based upon eqn (12), the expected isometric molar heat capacity becomes:

$$C_v = (n'' - 1)R. \tag{13}$$

The graph for eqn. (13) is shown on Fig. 1; based upon $C_v = 0$ when $n"$=1, and C_v= 19×8.314 =158.00 when $n"$=20. The fit for the isometric molar heat capacity (C_v) based upon eqn. (10) was very good, if not exceptional, for monatomic through triatomic gases ($n" < or = 4$) but not so much larger polyatomic gases i.e. $n" > 4$. Certainly eqn (13) is a better fit for the larger polyatomic gases than eqn. (10) was but the fit is only fairly good at best!

Reconsider what all might be happening. As previously stated, flatlining implies that large polyatomic gas' kinetic energy is no longer defined/controlled by the pumping of the wall molecule's vibrational energy onto the them. Remember by kinetic energy herein we mean the gas' translational plus rotational energy. In such a situation it becomes cumbersome to infer any net direction of energy flow being exchanged during collisions.

As previously stated, this author [1] understands that a limitation for the isometric molar heat capacity being defined by eqn (10) was the gas being *sufficiently dilute*, i.e. dilute enough that gas-wall molecule collisions are dominate in comparision to inter-gas molecule collisions. Part of the reasoning being that inter gas molecule collisions will obey conservation of momentum but not necessarily conservation of energy [1] i.e. inter-gas collisions tend to be inelastic. With further modelling this may help explain what is witnessed.

This author's insight that inter-gas collisions may generally be inelastic requires that radiation is given off during such collisions thus enabling inelastic collisions to adhere to conservation of energy [1]. Such collision induced radiation, whether it be considered as part of the system's blackbody and/or thermal energy, becomes part of the system being in thermal equilibrium i.e. the walls adsorb as much radiation energy as they emit.

The above is not to say that the walls and/or polyatomic gases necessarily emit the identical spectrum that they adsorb! It is, however to say that the total rate of energy of emission approximates that of the adsorption! Note; the total energy associated with radiation, whether it is blackbody, thermal or otherwise, can often be considered as insignificant, when compared to the energy associated with kinematics of matter. This is not saying that it can simply be ignored as is too often traditionally done in thermodynamics!

It should also be stated that large polyatomic gases will have large cross-sectional areas hence the concept of being sufficiently dilute may require higher mean molecular volumes in the gaseous state i.e. relatively low pressures.

Can we now claim that large polyatomic gas molecules tend to attain their kinetic energy from inter-gas collisions that obey conservation of momentum? No we cannot! However our expectation becomes that large polyatomic gases will not have the specified kinetic energies that smaller gases possess.

To further emphasize; the conceptualization of small gases having their kinetic energy pumped into to them by surrounding vibrating wall molecules, does not necessitate that gas-wall molecules collisions are elastic. On the contrary, it just implies that the gas' mean kinetic energy is driven into them via numerous collisions with wall molecules.

3 Addressing traditional dogma

As previously stated traditional kinetic theory is based upon equipartition and degrees of freedom arguments. We can go back further and acknowledge that for most of us, our learning started with considering a gas molecule's momentum and that momentum is conserved in elastic wall-gas molecule collisions.

The main problem with the above approach being that elastic collisions are a rarity i.e. it is rare to have a collision where both momentum and kinetic energy are conserved. The one simple exception being the case of two balls of equal mass colliding, with the second ball being stationary before the collision and that second ball then attains all the kinetic energy from the first ball, after the collision, i.e. first ball is stationary after the collision.

Rather than address the elephant in the room, traditional kinetic theory simply considered that all collisions are elastic,

as well as, the gas molecule leaves the wall with the same magnitude of momentum as it has prior to hitting the wall. Realizing that walls impose their energetics onto the dilute gas implies that traditional teaching may have put the cart ahead of the horse!

Certainly considering all collisions as being elastic avoids having to contemplate the various frequencies of radiation that would be associated with inelastic collisions. And when in equilibrium; since the mean kinetic energy of the gas molecules is constant then yes the mean magnitude of momentum remains constant but this is no longer a requirement for an elastic gas-wall collision!

The situation is no more complicated if it is considered that a dilute gas in thermal equilibrium requires that all of the following three states remain related to the same temperature (T). Basically, as previously stated by this author [1]:

1. The walls are in thermal equilibrium with the enclosed radiation i.e. blackbody, thermal or otherwise.
2. The gas' translational plus rotational energy is pumped into the gas by the more massive vibrating wall molecules.
3. The gas' vibrational energies are in thermal equilibrium with the enclosed radiation i.e. blackbody, thermal or otherwise.

Remember: Part of this radiation surrounding the gas molecules will now be a result of the various inelastic intermolecular collisions.

4 Atmospheric gases

At first glance considering that walls impose/pump their vibrational energy onto relatively small gases' kinetic energy, may feel counter-intuitive in part because gases are routinely put into, and/or removed from containers without any real noticeable temperature changes. However, if we realize that the above does not necessarily hold for enclosed larger polyatomic gases and that such gases generally obtain their vibrational energy from the surrounding blackbody/thermal radiation, then the mean energetics of such gases will not change significantly by placing them into, nor removing them from enclosures.

Certainly small gas molecules in our atmosphere will hit the Earth's rough surface and have a certain amount of their kinetic energy pumped/imposed upon them in various inelastic collisions with Earth's surface. Even so, for atmospheric gases inter-gas collisions still should dominate.

Next consider the collision of a small gas molecule with a larger polyatomic gas. The expectation becomes that the larger gas molecule will behave as a massive wall molecule does, i.e. the large polyatomic gas molecule will use its vibrational energies to pump/impose some fairly well-defined mean kinetic energy (translational plus rotational) onto the colliding small gas molecules.

5 Other proofs for inelastic collisions

There is more proof to inelastic intermolecular collisions than just the awkwardness of the mathematical justification for elastic intermolecular collisions. Some examples being:

1. Viscous dissipation i.e. heat being generated by gases squeezed through a valve.
2. Natural P-T relationships i.e. temperature increases with increasing pressure.
3. Joule's weight experiment i.e. Although designed to demonstrate a correlation between work and energy, what it really shows is that imposed increases to a liquid's flow (due to the paddles attached to weights) resulted in increased intermolecular friction, which generated heat.

All of the above is readily explained in terms of inelastic intermolecular collisions, but all are not so readily explainable in terms of traditional understandings.

6 Conclusions

This author's previous conclusion [1]; kinetic theory needs to be redrafted based upon the previous understanding that a gas' kinetic energy has both translational and rotational components that are pumped/imposed onto them due to the same wall molecule's vibrational energy. Moreover, it seemingly holds for most small gaseous molecules i.e. gas' whose polyatomic number is 4 or less.

For larger polyatomic gases, *flatlining* helps explain what is witnessed. Specifically flatlining means that larger polyatomic gases tend to strike two or more vibrating wall molecules at some instant. Therefore any kinetic energy transfer between impacting gas molecule and vibrating wall molecule, is not clean. Moreover it becomes awkward to even determine what direction the net flow of energy exchange actually goes, assuming that there is any actual a net energy exchange!

This certainly improves the fit between accepted empirical findings for large polyatomic gases and the kinetic theory as previously proposed [1], combined with what is currently described herein, by this author.

Interestingly, it can be contemplated that atmospheric gases will tend to follow similar dynamics where large polyatomic gases adsorb surrounding radiation (blackbody and/or thermal) thus increasing their vibrational energy. This vibrational energy is then pumped/imposed onto any small gas molecules that collide with the larger polyatomic gases.

Furthermore, we asserted that most inter-molecular collisons probably are inelastic. In which case radiation (thermal, blackbody or otherwise) will be a byproduct of such collisions, and as such must be considered as part of a system's state, whether or not, that system is in thermal equilibrium. And this does alter our consideration of thermal equilbrium!

The overall implication being that traditional theorists unwittingly put the cart ahead of the horse by beginning the

teaching of kinetic theory in terms of gas molecule's momentum and elastic collisions. This ignores the fact that elastic collisions are rare hence may be an unnecessary, illogical, unrealistic, conceptualization when applied to kinetic theory!

Submitted on February 12, 2018

References

1. Mayhew K.W. A new perspective for kinetic theory and heat capacity. *Progress in Physics*, 2017, v.13(4), 166–173.
2. Reif F. Fundamentals of Statistical and Thermal Physics. McGraw-Hill, New York, 1965.
3. Carey V. Statistical Thermodynamics and Microscale Thermophysics. Cambridge University Press, 1999.
4. Goldstein H. Classical Mechanics (2nd. ed.). Addison-Wesley, 1980.
5. Wüller A. Lehrbuch der Experimentalphysik (Textbook of Experimental Physics). Leipzig, Teubner, 1896, v.2, 507ff.
6. Boltzmann L. On certain Questions of the Theory of Gases. *Nature* 1895, v.51(1322), 413–415.
7. Planck M. On the Law of the Energy Distribution in the Normal Spectrum. *Ann. Phys.*, 1901, v.4(553), 1–11.
8. Enstein A. and Stern O. Einige Argumente Für die Annahme einer molekularen Agitation beim absolute Nullpunk (Some Arguments for the Assumption of Molecular Agitation at Absolute Zero). *Ann. Phys.*, 1913, v.40(551), 551–560.
9. Dahl J.P. On the Einstein–Stern model of rotational heat capacities. textitJ. of Chem. Physics, 1998, v.109, 10688.
10. Thomson W. Baltimore Lectures. Baltimore: Johns Hopkins University Press. Sec. 27. Re-issued in 1987 by MIT Press as *Kelvin's Baltimore Lectures and Modern Theoretical Physics: Historical and Philosophical Perspectives*, 1904.
11. Pais A. Subtle is the Lord. Oxford University Press. Oxford, 1982.
12. Hermann Armin (1971). The Genesis of Quantum Theory (1899–1913). Original title: Frühgeschichte der Quantentheorie (1899–1913), translated by Claude W. Nash ed., Cambridge, MA.
13. Masi J.F., Petkof B. *J. Res. Natl. Bur. Stand.*, 1952, v.48(3).
14. Scott R.B., Mellors J.W. *J. Res. Natl. Bur. Stand.*, v.34, March 1945.
15. Prydz R., Goodwin R.D. *J. Res. Natl. Bur. Stand.*, 1970, v.74A(5).
16. Giguere P.A. Heat capacities for water-hydrogen peroxide systems between 25 and 60 C. *J. Chem. Eng. Data*, 1962, v.7(4), 526–527.
17. Chapman S., Cowling T.G. The mathematical theory of non-uniform gases, third edition. Cambridge University Press, 1970.
18. Wu L., White C., Scanlon T.J., Reese J.M. and Zhang Y. A kinetic model of the Boltzmann equation for non-vibrating polyatomic gases. *J. Fluid Mechanics*, 2015, v.763, 24–50.
19. Mayhew K. Latent heat and critical temperature: A unique perspective. *Phys. Essays*, 2013, v.26, 4, 604–611.
20. Mayhew K. Second law and lost work. *Phys. Essays*, 2015, v.28, issue 1, 152–155.
21. Mayhew K. Entropy: an ill-conceived mathematical contrivance? *Phys. Essays*, 2015, v.28, issue 3, 352–357.
22. Mayhew K. Changing our perspective: Part 1: A New Thermodynamics (Self-published 2015) Available at:
http://www.newthermodynamics.com
https://createspace.com/5277845
23. Mayhew K. Improving our thermodynamic perspective. *Phys. Essays*, 2011, v.24, issue 3, 338–344.

Helical Solenoid Model of the Electron

Oliver Consa
Department of Physics and Nuclear Engineering, Universitat Politècnica de Catalunya
Campus Nord, C. Jordi Girona, 1-3, 08034 Barcelona, Spain
E-mail: oliver.consa@gmail.com

A new semiclassical model of the electron with helical solenoid geometry is presented. This new model is an extension of both the Parson Ring Model and the Hestenes Zitterbewegung Model. This model interprets the Zitterbewegung as a real motion that generates the electron's rotation (spin) and its magnetic moment. In this new model, the g-factor appears as a consequence of the electron's geometry while the quantum of magnetic flux and the quantum Hall resistance are obtained as model parameters. The Helical Solenoid Electron Model necessarily implies that the electron has a toroidal moment, a feature that is not predicted by Quantum Mechanics. The predicted toroidal moment can be tested experimentally to validate or discard this proposed model.

1 Introduction

Quantum mechanics (QM) is considered the most accurate physics theory available today. Since its conception, however, QM has generated controversy. This controversy lies not in the theory's results but in its physical interpretation.

One of the most controversial interpretations of QM was postulated by Bohr and Heisenberg. The "Copenhagen Interpretation" described QM as a system of probabilities that became definite upon the act of measurement. This interpretation was heavily criticized by many of the physicists who had participated in the development of QM, most notably Albert Einstein. Because of its probability features, Einstein believed that QM was only valid for analyzing the behavior of groups of particles and that the behavior of individual particles must be deterministic. In a famous quote from a 1926 letter to Max Born, Einstein stated, "He (God) does not play dice with the universe".

A major flaw in QM becomes apparent when the theory is applied to individual particles. This leads to logical contradictions and paradoxical situations (e.g., the paradox of Schrödinger's Cat). Einstein believed that QM was incomplete and that there must be a deeper theory based on hidden variables that would explain how subatomic particles behave individually. Einstein and his followers were not able to find a hidden variable theory that was compatible with QM, so the Copenhagen Interpretation was imposed as the interpretation of reference. If we assume that Einstein was correct, and that QM is only applicable to groups of particles, it is necessary to develop a new deterministic theory to explain the behavior of individual particles.

2 Spinning models of the electron

2.1 Ring Electron Model

In 1915, Parson [1] proposed a new model for the electron with a ring-shaped geometry where a unitary charge moves around the ring generating a magnetic field. The electron behaves not only as the unit of electric charge but also as the unit of magnetic charge or magneton. Several important physicists, including Webster, Gilbert, Grondahl and Page, conducted studies that supported Parson's Ring Electron Model. The most important of these studies was conducted by Compton [2], who wrote a series of papers showing that his newfound Compton Effect was better explained with Parson's Ring Electron Model than with the classical model that depicted the electron as a sphere. All these studies were compiled in 1918 by Allen [3] in "The Case for a Ring Electron" and discussed at a meeting of the Physical Society of London.

The Ring Electron Model was not widely accepted and was invalidated in 1923 by Schrödinger's wave equation of the electron. The Ring Electron Model has been unsuccessfully revisited several times by investigators like Iida, Carroll, Giese, Caesar, Bergman and Wesley [4], Lucas [5], Ginzburg or Kanarev [6]. Other researchers, such as Jennison [7], Gauthier [8], and Williamson and van der Mark [9], proposed similar models, with the additional assumption that the electron is a photon trapped in a vortex.

The Ring Electron Model proposes that the electron has an extremely thin, ring-shaped geometry that is about 2000 times larger than a proton. A unitary charge flows through the ring at the speed of light, generating an electric current and an associated magnetic field. This model allows us to combine experimental evidence that the electron has an extremely small size (corresponding to the thickness of the ring) as well as a relatively large size (corresponding to the circumference of the ring).

The Ring Electron Model postulates that the rotational velocity of the electric charge will match the speed of light and that the angular momentum will match the reduced Planck constant:

$$v_r = c, \tag{1}$$

$$L = mRv_r = \hbar. \tag{2}$$

As a consequence of (1) and (2), the radius of the ring will match the reduced Compton wavelength and the circum-

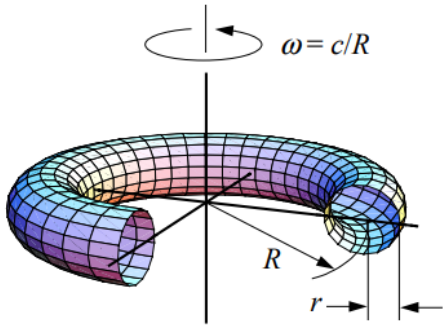

Fig. 1: Ring Electron Model.

ference will matches the Compton wavelength

$$R = \frac{\hbar}{mv_r} = \frac{\hbar}{mc} = \lambda\!\!\!^{-}_c \,, \tag{3}$$

$$2\pi R = \frac{h}{mc} = \lambda_c \,. \tag{4}$$

Meanwhile, the frequency, angular frequency and rotation time period of the ring electron are defined by:

$$f_e = \frac{v_r}{2\pi R} = \frac{mc^2}{h} \,, \tag{5}$$

$$w_e = 2\pi f_e = \frac{mc^2}{\hbar} \,, \tag{6}$$

$$T_e = \frac{1}{f_e} = \frac{h}{mc^2} \,. \tag{7}$$

The electron's ring acts as a circular antenna. In this type of antenna, the resonance frequency coincides with the length of the antenna's circumference. In the case of the electron ring, the resonance frequency coincides with the electron's Compton frequency.

Substituting the electron's frequency (5) in the Planck equation ($E = hf$), we obtain the Einstein's energy equation

$$E = hf_e = h\,\frac{mc^2}{h} = mc^2. \tag{8}$$

The moving charge generates a constant electric current. This electric current produces a magnetic moment that is equal to the Bohr magneton:

$$I = ef_e = \frac{emc^2}{h} \,, \tag{9}$$

$$\mu_e = IS = \frac{emc^2}{h}\,\pi R^2 = \frac{e}{2m}\,\hbar = \mu_B \,. \tag{10}$$

The relationship between the magnetic moment and the angular momentum is called the "gyromagnetic ratio" and has the value "$e/2m$". This value is consistent with the magnetic moment generated by an electric current rotating on a circular surface of radius R. The gyromagnetic ratio of the electron can be observed experimentally by applying external magnetic fields (for example, as seen in the "Zeeman effect" or in the "Stern-Gerlach experiment"):

$$E = \frac{e}{2m}\,B. \tag{11}$$

The energy of the electron is very low, but the frequency of oscillation is extremely large, which results in a significant power of about 10 gigawatts:

$$P = \frac{E}{T} = \frac{m^2c^4}{h} = 1.01 \times 10^7 \text{ W}. \tag{12}$$

Using the same line of reasoning, the electric potential can be calculated as the electron energy per unit of electric charge, resulting in a value of approximately half a million volts:

$$V = \frac{E}{e} = \frac{mc^2}{e} = 5.11 \times 10^5 \text{ V}. \tag{13}$$

The electric current has already been calculated as 20 amps ($I = ef = 19.83$ A). Multiplying the voltage by the current, the power is, again, about 10 gigawatts ($P = VI$).

The Biot-Savart Law can be applied to calculate the magnetic field at the center of the ring, resulting in a magnetic field of 30 million Tesla, equivalent to the magnetic field of a neutron star:

$$B = \frac{\mu_0 I}{2R} = 3.23 \times 10^7 \text{ T}. \tag{14}$$

For comparison, the magnetic field of the Earth is 0.000005 T, and the largest artificial magnetic field created by man is only 90 T.

The electric field in the center of the electron's ring matches the value of the magnetic field multiplied by the speed of light:

$$E = \frac{e}{4\pi\epsilon_0 R^2} = cB = 9.61 \times 10^{12} \text{ V/m}. \tag{15}$$

The Ring Electron Model implies the existence of a centripetal force that compensates for the centrifugal force of the electron orbiting around its center of mass:

$$F = m\,\frac{v_r^2}{R} = \frac{m^2c^3}{\hbar} = 0.212 \text{ N}. \tag{16}$$

Electromagnetic fields with a Lorentz force greater than this centripetal force should cause instabilities in the electron's geometry. The limits of these electric and magnetic fields are:

$$F = eE + evB, \tag{17}$$

$$E = \frac{m^2c^3}{e\hbar} = 1.32 \times 10^{18} \text{ V/m}, \tag{18}$$

$$B = \frac{m^2c^2}{e\hbar} = 4.41 \times 10^9 \text{ T}. \tag{19}$$

In quantum electrodynamics (QED), these two values are known as the Schwinger Limits [10]. Above these values, electromagnetic fields are expected to behave in a nonlinear way. While electromagnetic fields of this strength have not yet been achieved experimentally, current research suggests that electromagnetic field values above the Schwinger Limits will cause unexpected behavior not explained by the Standard Model of Particle Physics.

2.2 Helical Electron Model

In 1930, while analyzing possible solutions to the Dirac equation, Schrödinger identified a term called the Zitterbewegung that represents an unexpected oscillation whose amplitude is equal to the Compton wavelength. In 1953, Huang [11] provided a classical interpretation of the Dirac equation in which the Zitterbewegung is the mechanism that causes the electron's angular momentum (spin). According to Huang, this angular momentum is the cause of the electron's magnetic moment. Bunge [12], Barut [13], Zhangi [14], Bhabha, Corben, Weyssenhoff, Pavsic, Vaz, Rodrigues, Salesi, Recami, Hestenes [15, 16] and Rivas [17] have published papers interpreting the Zitterbewegung as a measurement of the electron's oscillatory helical motion that is hidden in the Dirac equation. We refer to these electron theories as the Hestenes Zitterbewegung Model or the Helical Electron Model.

The Helical Electron Model assumes that the electron's charge is concentrated in a single infinitesimal point called the center of charge (CC) that rotates at the speed of light around a point in space called the center of mass (CM).

The Helical Electron Model shares many similarities with the Ring Electron Model, but in the case of the Helical Electron Model, the geometric static ring is replaced by a dynamic point-like electron. In this dynamic model, the electron's ring has no substance or physical properties. It need not physically exist. It is simply the path of the CC around the CM.

The CC moves constantly without any loss of energy so that the electron acts as a superconducting ring with a persistent current. Such flows have been experimentally detected in superconducting materials.

The CC has no mass, so it can have an infinitesimal size without collapsing into a black hole, and it can move at the speed of light without violating the theory of relativity. The electron's mass is not a single point. Instead, it is distributed throughout the electromagnetic field. The electron's mass corresponds to the sum of the electron's kinetic and potential energy. By symmetry, the CM corresponds to the center of the electron's ring.

We can demonstrate the principles of the Helical Electron Model with an analogy to the postulates of the Bohr Atomic Model:

- The CC always moves at the speed of light, tracing circular orbits around the CM without radiating energy.

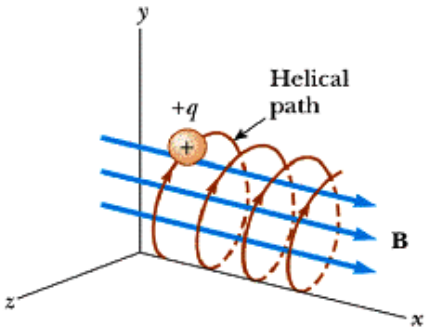

Fig. 2: Helical Electron Model.

- The electron's angular momentum equals the reduced Planck constant.
- The electron emits and absorbs electromagnetic energy that is quantized according to the formula $E = hf$.
- The emission or absorption of energy implies an acceleration of the CM.

The electron is considered to be at rest if the CM is at rest, since in that case the electric charge has only rotational movement without any translational movement. In contrast, if the CM moves with a constant velocity (v), then the CC moves in a helical motion around the CM.

The electron's helical motion is analogous to the observed motion of an electron in a homogeneous external magnetic field.

It can be parameterized as:

$$\begin{cases} x(t) = R\cos(wt)\,, \\ y(t) = R\sin(wt)\,, \\ z(t) = vt\,. \end{cases} \tag{20}$$

The electron's helical motion can be deconstructed into two orthogonal components: a rotational motion and a translational motion. The velocities of rotation and translation are not independent; they are constrained by the electron's tangential velocity that is constant and equal to the speed of light. As discussed above, when the electron is at rest, its rotational velocity is equal to the speed of light. As the translational velocity increases, the rotational velocity must decrease. At no time can the translational velocity exceed the speed of light. Using the Pythagorean Theorem, the relationship between these three velocities is:

$$c^2 = v_r^2 + v_t^2\,. \tag{21}$$

Then the rotational velocity of the moving electron is:

$$v_r = c\sqrt{1-(v/c)^2}\,, \tag{22}$$

$$v_r = c/\gamma\,. \tag{23}$$

Where gamma is the coefficient of the Lorentz transformation, the base of the Special Relativity Theory:

$$\gamma = \frac{1}{\sqrt{1-(v/c)^2}}\,. \tag{24}$$

Multiplying the three components by the same factor $(\gamma mc)^2$:

$$(\gamma mc)^2 c^2 = (\gamma mc)^2 v_r^2 + (\gamma mc)^2 v_t^2. \tag{25}$$

Substituting the value of the rotational velocity ($v_r = c/\gamma$) and linear momentum ($p = \gamma mv$), results in the relativistic energy equation:

$$E^2 = (\gamma mc^2)^2 = (mc^2)^2 + (pc)^2. \tag{26}$$

With this new value of the rotational velocity, the frequency, angular frequency and rotational time period of the helical electron are defined by:

$$f_e = \frac{v_r}{2\pi R} = \frac{mc^2}{\gamma h}\,, \tag{27}$$

$$w_e = 2\pi f_e = \frac{mc^2}{\gamma \hbar}\,, \tag{28}$$

$$T_e = \frac{1}{f_e} = \frac{\gamma h}{mc^2}\,. \tag{29}$$

The rotation time period of the electron acts as the electron's internal clock. As a result, although there is no absolute time in the universe, each electron is always set to its proper time. This proper time is relative to the electron's reference frame and its velocity with respect to other inertial reference frames.

The electron's angular momentum is always equal to the reduced Planck constant. This implies that the electron's mass has to increase γ times in order to compensate for the decrease in its rotational velocity:

$$L = mRv_r = (\gamma m)\, R\, (c/\gamma) = mRc = \hbar. \tag{30}$$

If the electron moves at a constant velocity, the particle's trajectory is a cylindrical helix. The geometry of the helix is defined by two constant parameters: the radius of the helix (R) and the helical pitch (H). The helical pitch is the space between two turns of the helix. The electron's helical motion can be interpreted as a wave motion with a wavelength equal to the helical pitch and a frequency equal to the electron's natural frequency. Multiplying the two factors results in the electron's translational velocity:

$$\lambda_e f_e = v\,, \tag{31}$$

$$\lambda_e = H = \frac{v}{f_e} = v\,\frac{\gamma h}{mc^2} = \gamma\beta\lambda_c\,. \tag{32}$$

The rest of the parameters representative of a cylindrical helix can also be calculated, including the curvature (κ) and the torsion (τ), where $h = 2\pi H = \gamma\beta\lambda\!\!\!^{-}_c$:

$$\begin{cases} \kappa = \dfrac{R}{R^2+h^2} = \dfrac{1}{\gamma^2 R}\,, \\[2ex] \tau = \dfrac{h}{R^2+h^2} = \dfrac{\beta}{\gamma R}\,. \end{cases} \tag{33}$$

According to Lancret's Theorem, the necessary and sufficient condition for a curve to be a helix is that the ratio of curvature to torsion must be constant. This ratio is equal to the tangent of the angle between the osculating plane with the axis of the helix:

$$\tan\alpha = \frac{\kappa}{\tau} = \frac{1}{\gamma\beta}\,. \tag{34}$$

2.3 Toroidal Solenoid Electron Model

In 1956, Bostick, a disciple of Compton, discovered the existence of plasmoids. A plasmoid is a coherent toroidal structure made up of plasma and magnetic fields. Plasmoids are so stable that they can behave as individual objects and interact with one another. From Parson's Ring Electron Model, Bostick [21] proposed a new electron structure, similar to that of the plasmoids. In his model, the electron takes the shape of a toroidal solenoid where the electric charge circulates at the speed of light. In the Toroidal Solenoid Electron Model, we assume that the electric charge is a point particle and that the toroidal solenoid represents the trajectory of that point electric charge.

In a toroidal solenoid, any magnetic flux is confined within the toroid. This feature is consistent with the idea that the mass of a particle matches the electromagnetic energy contained therein. Storage of electromagnetic energy in a toroidal solenoid superconductor without the loss of energy is called superconducting magnetic energy storage (SMES). According to the Toroidal Solenoid Electron model, an electron is a microscopic version of a SMES system.

Toroidal solenoid geometry is well known in the electronics field where it is used to design inductors and antennas. A toroidal solenoid provides two additional degrees of freedom compared to the ring geometry. In addition to the radius (R) of the torus, two new parameters appear: the thickness of the torus (r) and the number of turns around the torus (N) with N being an integer.

The toroidal solenoid can be parameterized as:

$$\begin{cases} x(t) = (R + r\cos Nwt)\cos wt\,, \\ y(t) = (R + r\cos Nwt)\sin wt\,, \\ z(t) = r\sin Nwt. \end{cases} \tag{35}$$

Where the tangential velocity is:

$$|r'(t)|^2 = (R + r\cos Nwt)^2 w^2 + (rNw)^2. \tag{36}$$

We postulate that the tangential velocity is always equal to the speed of light ($|r'(t)| = c$). For $R \gg rN$, the rotational

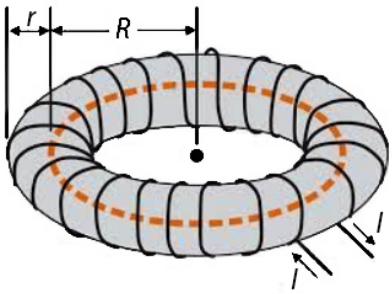

Fig. 3: Helical Toroidal Electron Model.

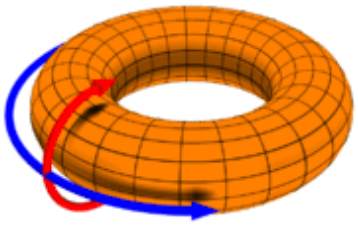

Fig. 4: Toroidal and Poloidal currents.

velocity can be obtained as:

$$c^2 = (Rw)^2 + (rNw)^2, \tag{37}$$

$$c/v_r = \sqrt{1 + \left(\frac{rN}{R}\right)^2}\,. \tag{38}$$

The second factor depends only on the geometry of electron. We call this value the helical g-factor. If $R \gg rN$, the helical g-factor is slightly greater than 1,

$$g = \sqrt{1 + \left(\frac{rN}{R}\right)^2}\,. \tag{39}$$

As a result, the rotational velocity is dependent on the helical g-factor and slightly lower than the speed of light:

$$v_r = c/g. \tag{40}$$

With this new value of the rotational velocity, the frequency, angular frequency and time period are defined by:

$$f_e = \frac{v_r}{2\pi R} = \frac{mc^2}{gh}\,, \tag{41}$$

$$w_e = 2\pi f_e = \frac{mc^2}{g\hbar}\,, \tag{42}$$

$$T_e = \frac{1}{f_e} = \frac{gh}{mc^2}\,. \tag{43}$$

The length of a turn of the toroidal solenoid is called the arc length. To calculate the arc length, we need to perform the integral of the toroidal solenoid over one turn:

$$\begin{aligned} l &= \int \sqrt{|r'(t)|^2}dt \\ &= \int \sqrt{(R + r\cos Nwt)^2 w^2 + (rNw)^2}\; dt\,. \end{aligned} \tag{44}$$

Approximating for $R \gg Nr$ and replacing the helical g-factor (39) results in:

$$\begin{aligned} l &= \int \sqrt{(Rw)^2 + (rNw)^2}dt \\ &= \int Rw\sqrt{1 + (rN/R)^2}\; dt = gR\int wdt = 2\pi gR\,. \end{aligned} \tag{45}$$

This means that the arc length of a toroidal solenoid is equivalent to the length of the circumference of a ring of radius $R' = gR$:

$$l = 2\pi gR = 2\pi R'. \tag{46}$$

In calculating the electron's angular momentum, we must take into consideration the helical g-factor. The value of the rotational velocity is reduced in proportion to the equivalent radius, so that the angular momentum remains constant:

$$L = mR'v_r = m\,(gR)\left(\frac{c}{g}\right) = \hbar. \tag{47}$$

The electric current flowing through a toroidal solenoid has two components, a toroidal component (red) and a poloidal component (blue).

By symmetry, the magnetic moment due to the poloidal components (red) is canceled, while the toroidal component (blue) remains fixed. No matter how large the number of turns in the toroidal solenoid, a toroidal component generates a corresponding axial magnetic moment [22]. This effect is well known in the design of toroidal antennas and can be canceled with various techniques. The exact value of the axial magnetic moment is:

$$m = I\pi R^2\left[1 + \frac{1}{2}\left(\frac{r}{R}\right)^2\right]. \tag{48}$$

A comparison of the Toroidal Solenoid Electron Model ($v = 0, r > 0$) with the Ring Electron Model ($v = 0, r = 0$) reveals that the radius still coincides with the reduced Compton wavelength. The electric current is slightly lower, since the electron's rotational velocity is also slightly lower:

$$I\pi R^2 = ef\pi R^2 = \frac{ev_rR}{2} = \frac{ec\hbar}{2gmc} = \frac{e\hbar}{2mg} = \frac{\mu_B}{g}, \tag{49}$$

$$m = \frac{\mu_B}{g}\left[1 + \frac{1}{2}\left(\frac{r}{R}\right)^2\right], \tag{50}$$

$$m \simeq g\mu_B. \tag{51}$$

In calculating the angular momentum, the rotational velocity decreases in the same proportion as the equivalent radius increase, compensating for the helical g-factor. However, in

the calculation of magnetic moment, the rotational velocity decreases by a factor of g, while the equivalent radius increases by a factor approximately equal to g squared. This is the cause of the electron's anomalous magnetic moment.

2.4 Helical Solenoid Model

The geometries of both the Ring Electron Model and the Toroidal Solenoid Electron Model represent a static electron ($v = 0$). For a moving electron with a constant velocity ($v > 0$), the ring geometry becomes a circular helix, while the toroidal solenoid geometry becomes a helical solenoid. On the other hand, if the thickness of the toroid is negated ($r = 0$), the toroidal solenoid is reduced to a ring, and the helical solenoid is reduced to a helix.

Experimentally, the electron's magnetic moment is slightly larger than the Bohr magneton. In the Ring Electron Model, it was impossible to explain the electron's anomalous magnetic moment. This leads us to assume that the electron has a substructure. The Toroidal Solenoid Electron Model allows us to obtain the electron's anomalous moment as a direct consequence of its geometry.

Geometry	$v = 0$	$v > 0$
$r = 0$	Ring	Helix
$r > 0$	Toroidal Solenoid	Helical Solenoid

The universe generally behaves in a fractal way, so the most natural solution assumes that the electron's substructure is similar to the main structure, that is, a helix in a helix.

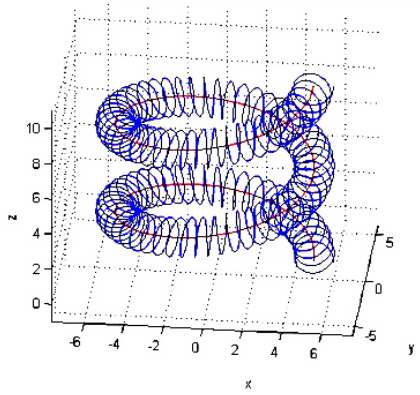

Fig. 5: Helical Solenoid Electron Model.

The trajectory of the electron can be parameterized with the equation of the helical solenoid:

$$\begin{cases} x(t) = (R + r\cos Nwt)\cos wt\,, \\ y(t) = (R + r\cos Nwt)\sin wt\,, \\ z(t) = r\sin Nwt + vt\,. \end{cases} \tag{52}$$

Like the other electron models discussed above, the Helical Solenoid Electron Model postulates that the tangential velocity of the electric charge matches the speed of light and that the electron's angular momentum matches the reduced Planck constant.

$$\begin{aligned} |r'(t)|^2 = c^2 &= (Rw)^2 + (rNw)^2 + v^2 \\ &+ rw(2Rw + rw\cos Nwt + 2vN)\cos Nwt\,. \end{aligned} \tag{53}$$

This equation can be obtained directly from the helical solenoid geometry without any approximation. This equation shows a component that oscillates at a very high frequency with an average value of zero. Consequently, the Helical Solenoid Electron Model implies that the electron's g-factor is oscillating, not fixed. Since the value oscillates, there is a maximum level of precision with which the g-factor can be measured. This prediction is completely new to this model and is directly opposite to previous QED predictions. For $R \gg rN$, this oscillating component can be negated, and the equation reduces to

$$c^2 = (Rw)^2 + (rNw)^2 + v^2. \tag{54}$$

The rotational velocity can be obtained as a function of the speed of light, the Lorentz factor, and the helical g-factor:

$$c^2 = (Rw)^2(1 + (rN/R)^2) + v^2, \tag{55}$$

$$c^2 = (v_r)^2 g^2 + v^2, \tag{56}$$

$$gv_r = c\sqrt{1 - v^2/c^2}\,, \tag{57}$$

$$v_r = c/g\gamma. \tag{58}$$

With this new value of the rotational velocity, the frequency, angular frequency, rotation time period and the wavelength (o pitch) of the helical solenoid electron are defined by:

$$f_e = \frac{v_r}{2\pi R} = \frac{mc^2}{g\gamma h}\,, \tag{59}$$

$$w_e = 2\pi f_e = \frac{mc^2}{g\gamma\hbar}\,, \tag{60}$$

$$T_e = \frac{1}{f_e} = \frac{g\gamma h}{mc^2}\,, \tag{61}$$

$$\lambda_e = H = \frac{v}{f_e} = g\gamma\beta\lambda_c\,. \tag{62}$$

In 2005, Michel Gouanère [18] identified this wavelength in a channeling experiment using a beam of ~80 MeV electrons aligned along the $< 110 >$ direction of a thick silicon crystal ($d = 3.84 \times 10^{-10}$ m). While this experiment has not had much impact on QM, both Hestenes [19] and Rivas [20] have indicated that the experiment provides important experimental evidence consistent with the Hestenes Zitterbewegung Model:

$$d = g\gamma\beta\lambda_c = (\gamma mv)\,\frac{gh}{(mc)^2} = p\,\frac{gh}{(mc)^2}\,, \tag{63}$$

$$p = d\,\frac{(mc)^2}{gh} = 80.874\ \text{MeV/c}. \tag{64}$$

In the Helical Solenoid Electron Model, the rotational velocity is reduced by both the helical g-factor and the Lorentz factor. In contrast, the equivalent radius compensates for the helical g-factor while the increasing mass compensates for the Lorentz factor. The angular momentum remains equal to the reduced Planck constant:

$$L = m'R'v_r = (\gamma m)(gR)(c/\gamma g) = mRc = \hbar. \tag{65}$$

3 Consequences of the Helical Solenoid Electron Model

3.1 Chirality and helicity

In 1956, an experiment based on the beta decay of a Cobalt-60 nucleus demonstrated a clear violation of parity conservation. In the early 1960s the parity symmetry breaking was used by Glashow, Salam and Weinberg to develop the Electroweak Model, unifying the weak nuclear force with the electromagnetic force. The empirical observation that electroweak interactions act differently on right-handed fermions and left-handed fermions is one of the basic characteristics of this theory.

In the Electroweak Model, chirality and helicity are essential properties of subatomic particles, but these abstract concepts are difficult to visualize. In contrast, in the Helical Solenoid Electron Model, these concepts are evident and a direct consequence of the model's geometry:

- Helicity is given by the helical translation motion ($v > 0$), which can be left-handed or right-handed. Helicity is not an absolute value; it is relative to the speed of the observer.
- Chirality is given by the secondary helical rotational motion, which can also be left-handed or right-handed. Chirality is absolute since the tangential velocity is always equal to the speed of light; it is independent of the velocity of the observer.

3.2 Quantum Hall resistance and magnetic flux

The movement of the electric charge causes an electrical current ($I = ef_e$) and a electric voltage ($V = E/e = hf_e/e$). Applying Ohm's law, we obtain a fixed value for the impedance of the electron equal to the value of the quantum Hall resistance. This value is quite surprising, since it is observable at the macroscopic level and was not discovered experimentally until 1980:

$$R = \frac{V_e}{I_e} = \frac{hf_e/e}{ef_e} = \frac{h}{e^2}\,. \tag{66}$$

According to Faraday's Law, voltage is the variation of the magnetic flux per unit of time. So, in a period of rotation, we obtain a magnetic flux value which coincides with the quantum of magnetic flux, another macroscopically observable value. This value was expected since, in this model, the electron behaves as a superconducting ring, and it is experimentally known that the magnetic flux in a superconducting ring is quantized:

$$V = \phi_e/T_e\,, \tag{67}$$

$$\phi_e = V_eT_e = \frac{hf_e}{e}\frac{1}{f_e} = \frac{h}{e}\,. \tag{68}$$

3.3 Quantum LC circuit

Both the electrical current and the voltage of the electron are frequency dependent. This means that the electron behaves as a quantum LC circuit, with a Capacitance (C) and a Self Inductance (L). We can calculate these coefficients for a electron at rest, obtaining values $L = 2.08 \times 10^{-16}$ H and $C = 3.13 \times 10^{-25}$ F:

$$L_e = \frac{\phi_e}{I_e} = \frac{h}{e^2f_e} = \frac{g\gamma h^2}{mc^2e^2}\,, \tag{69}$$

$$C_e = \frac{e}{V_e} = \frac{e^2}{hf_e} = \frac{g\gamma e^2}{mc^2}\,. \tag{70}$$

Applying the formulas of the LC circuit, we can obtain the values of impedance and resonance frequency, which coincide with the previously calculated values of impedance and natural frequency of the electron:

$$Z_e = \sqrt{\frac{L_e}{C_e}} = \frac{h}{e^2}\,, \tag{71}$$

$$f_e = \frac{1}{\sqrt{L_eC_e}} = \frac{mc^2}{g\gamma h} = f_e\,. \tag{72}$$

As the energy of the particle oscillates between electric and magnetic energy, the average energy value is

$$E = \frac{LI^2}{2} + \frac{CV^2}{2} = \frac{hf}{2} + \frac{hf}{2} = hf\,. \tag{73}$$

The above calculations are valid for any elementary particle with a unit electric charge, a natural frequency of vibration and an energy which match the Planck equation ($E = hf$).

From this result, we infer that the electron is formed by two indivisible elements: a quantum of electric charge and a quantum of magnetic flux, the product of which is equal to Planck's constant. The electron's magnetic flux is simultaneously the cause and the consequence of the circular motion of the electric charge:

$$e\phi = h. \tag{74}$$

3.4 Quantitative calculation of the helical G-factor

The g-factor depends on three parameters (R, r and N) but we do not know the value of two of them. We can try to figure out the value of the helical g-factor using this approximation [28]:

Using this expansion series:

$$\sqrt{1 + (a)^2} = 1 + 1/2(a)^2 + \ldots \tag{75}$$

The helical g-factor can be expressed as:

$$\sqrt{1+\left(\frac{rN}{R}\right)^2} = 1 + \frac{1}{2}\left(\frac{rN}{R}\right)^2 + \dots \tag{76}$$

QED also calculates the g-factor by an expansion series where the first term is 1 and the second term is the Schwinger factor:

$$g.factor(QED) = 1 + \frac{\alpha}{2\pi} + \dots \tag{77}$$

The results of the two series are very similar. Equaling the second term of the helical g-factor series to the Schwinger factor, we obtain the relationship between the radius of the torus and the thickness of the torus:

$$\frac{1}{2}\left(\frac{rN}{R}\right)^2 = \frac{\alpha}{2\pi}, \tag{78}$$

$$\frac{rN}{R} = \sqrt{\frac{\alpha}{\pi}}. \tag{79}$$

What gives a value of helical g-factor of

$$g = \sqrt{1+\alpha/\pi}. \tag{80}$$

This gives us a value of the helical g-factor = 1.0011607. This result is consistent with the Schwinger factor, and it offers a value much closer to the experimental value.

3.5 Toroidal moment

In 1957, Zel'dovich [23] discussed the parity violation of elementary particles and postulated that spin-1/2 Dirac particles must have an anapole. In the late 1960s and early 1970s, Dubovik [24, 25] connected the quantum description of the anapole to classical electrodynamics by introducing the polar toroidal multipole moments. The term toroidal derives from current distributions in the shape of a circular coil that were first shown to have a toroidal moment. Toroidal moments were not acknowledged outside the Soviet Union as being an important part of the multipole expansion until the 1990s. Toroidal moments became known in western countries in the late 1990s. Finally, in 1997, toroidal moment was experimentally measured in the nuclei of Cesium-133 and Ytterbium-174 [26].

In 2013, Ho and Scherrer [27] hypothesized that Dark Matter is formed by neutral subatomic particles. These particles of cold dark matter interact with ordinary matter only through an anapole electromagnetic moment, similar to the toroidal magnetic moment described above. These particles are called Majorana fermions, and they cannot have any other electromagnetic moment apart from the toroid moment. The model for these subatomic particles of dark matter is compatible with the Helical Solenoid Electron Model.

In an electrostatic field, all charge distributions and currents may be represented by a multipolar expansion using only electric and magnetic multipoles. Instead, in a multipolar expansion of an electrodynamic field new terms appear. These new terms correspond to a third family of multipoles: the toroid moments. The toroidal lower order term is the toroidal dipole moment. The toroidal moment can understood as the momentum generated by a distribution of magnetic moments. The simplest case is the toroidal moment generated by an electric current in a toroidal solenoid.

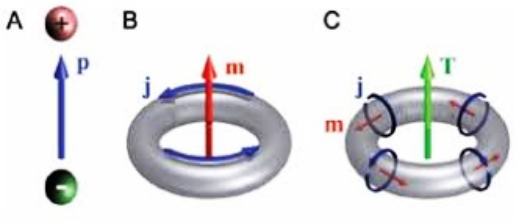

Fig. 6: Electric, Magnetic and Toroidal dipole moments.

The toroidal moment is calculated with the following equation [24]:

$$T = \frac{1}{10}\int \left[(\mathbf{j}\cdot\mathbf{r})\,\mathbf{r} - 2r^2\mathbf{j}\right] dV. \tag{81}$$

In the case of the toroidal solenoid, the toroidal moment can be calculated more directly as the B field inside the toroid by both the surface of the torus and the surface of the ring [25]:

$$\mu T = BsS = B\left(\pi r^2\right)\left(\pi R^2\right), \tag{82}$$

$$B = \frac{\mu NI}{2\pi R}. \tag{83}$$

Using B, the toroidal moment is obtained as [22]:

$$T = \frac{NI}{2\pi R}\left(\pi r^2\right)\left(\pi R^2\right) = \frac{NI\left(\pi r^2\right)R}{2}. \tag{84}$$

Rearranging and using the relation (79):

$$T = \mu_B \frac{R}{g2N}\left(\frac{rN}{R}\right)^2 = \mu_B \frac{\lambda\!\!\!^{-}_c}{gN}\left(\frac{\alpha}{2\pi}\right). \tag{85}$$

According the Helical Solenoid Electron Model, the electron's theoretical toroidal moment is about $T \simeq 10^{-40}$ Am^3. The theoretical toroidal moment value for the neutron and the proton should be one million times smaller. The existence of a toroidal moment for the electron (and for any other subatomic particle) is a direct consequence of this model, and it may be validated experimentally. Notably, QM does not predict the existence of any toroidal moments.

3.6 Nucleon model

By analogy to the theory underlying the Helical Solenoid Electron Model, we assume that all subatomic particles have the same structure as the electron, differing mainly by their

charge and mass. Protons are thought to be composed of other fundamental particles called quarks, but their internal organization is beyond the scope of this work.

The radius of a nucleon is equal to its reduced Compton wavelength. The Compton wavelength is inversely proportional to an object's mass, so for subatomic particles, as mass increases, size decreases. Both the proton and the neutron have a radius that is about 2000 times smaller than the electron. Historically, the proton radius was measured using two independent methods that converged to a value of about 0.8768 fm. This value was challenged by a 2010 experiment utilizing a third method, which produced a radius of about 0.8408 fm. This discrepancy remains unresolved and is the topic of ongoing research referred to as the Proton Radius Puzzle. The proton's reduced Compton wavelength is 0.2103 fm. If we multiple this radius by 4, we obtain the value of 0.8412 fm. This value corresponds nicely with the most recent experimental radius of the proton. This data supports our theory that the proton's radius is related to its reduced Compton radius and that our Helical Solenoid Electron Model is also a valid model for the proton.

The current of a nucleon is about 2000 times the current of an electron, and the radius is about 2000 times lower. This results in a magnetic field at the center of the nucleon's ring that is about four million times bigger than that of the electron or thousands of times bigger than a neutron star. This magnetic field is inversely dependent with the cube of the distance. This implies that while the magnetic field inside the neutron's ring is huge, outside the ring, the magnetic field decays much faster than the electric field. The asymmetrical behavior of the neutron's magnetic field over short and long distances leads us to suggest that the previously identified strong and weak nuclear forces are actually manifestations of this huge magnetic field at very short distances.

3.7 Spin quantum number

In 1913, Bohr introduced the Principal Quantum Number to explain the Rydberg Formula for the spectral emission lines of atomic hydrogen. Sommerfeld extended the Bohr theory with the Azimuthal Quantum Number to explain the fine structure of the hydrogen, and he introduced a third Magnetic Quantum Number to explain the Zeeman effect. Finally, in 1921, Landé put forth a formula (named the Landé g-factor) that allowed him to explain the anomalous Zeeman effect and to obtain the whole spectrum of all atoms.

$$g_J = g_L \frac{J(J+1) - S(S+1) + L(L+1)}{2J(J+1)} + g_S \frac{J(J+1) + S(S+1) - L(L+1)}{2J(J+1)}. \quad (86)$$

In this formula, Landé introduced a fourth Quantum Number with a half-integer number value (S = 1/2). This Landé g-factor was an empirical formula where the physical meaning of the four quantum numbers and their relationship with the motion of the electrons around the nucleus was unknown. Heisenberg, Pauli, Sommerfeld, and Landé tried unsuccessfully to devise a new atomic model (named the Ersatz Model) to explain this empirical formula. Landé proposed that his g-factor was produced by the combination of the orbital momentum of the outer electrons with the orbital momentum of the inner electrons. A different solution was suggested by Kronig, who proposed that the half-integer number was generated by a self-rotation motion of the electron (spin), but Pauli rejected this theory.

In 1925, Uhlenbeck and Goudsmit published a paper proposing the same idea, namely that the spin quantum number was produced by the electron's self-rotation. The half-integer spin implies an anomalous magnetic moment of 2. In 1926, Thomas identified a relativistic correction of the model with a value of 2 (named the Thomas Precession) that compensated for the anomalous magnetic moment of the spin. Despite his initial objections, Pauli formalized the theory of spin in 1927 using the modern theory of QM as set out by Schrödinger and Heisenberg. Pauli proposed that spin, angular moment, and magnetic moment are intrinsic properties of the electron and that these properties are not related to any actual spinning motion. The Pauli Exclusion Principle states that two electrons in an atom or a molecule cannot have the same four quantum numbers. Pauli's ideas brought about a radical change in QM. The Bohr-Sommerfeld Model's explicit electron orbitals were abandoned and with them any physical model of the electron or the atom.

We propose to return to the old quantum theory of Bohr-Sommerfeld to search for a new Ersatz Model of the atom where the four quantum numbers are related to electron orbitals. We propose that this new atomic model will be compatible with our Helical Solenoid Electron Model. We also propose that the half-integer spin quantum number is not an intrinsic property of the electron but a result of the magnetic fields generated by orbiting inner electrons.

Submitted on January 25, 2018

References

1. Parson L. A Magneton Theory of the Structure of the Atom. *Smithsonian Miscellaneous Collections*, 1915, v. 65, 2–80.
2. Compton A.H. The Size and Shape of the Electron. *Phys. Rev.*, 1917. v. 14(3), 247–259.
3. Allen H.S. The Case for a Ring Electron. *Proceedings of the Physical Society*, 1919, v. 31, 49–68.
4. Bergman D., Wesley J.P. Spinning Charged Ring Model of Electron Yielding Anomalous Magnetic Moment. *Galilean Electrodynamics*, 1990, v. 1, 63–67.
5. Lucas C.W. A Classical Theory of Elementary Particles Electromagnetic Part 2, intertwining Charge-Fibers. *The Journal of Common Sense Science*, 2005, v. 8(2), 1–7.
6. Kanarev P. Model of the Electron. *Apeiron*, 2000, v. 7(3–4), 184–194.
7. Jennison R.C. A new classical relativistic model of the electron. *Phys. Letters A.*, 1989, v. 141(8–9), 377–382.

8. Gauthier R. Superluminal Quantum Models of the Electron and the Photon. viXra:0703.0015.
9. Williamson J.G., van der Mark J.M.B. Is the electron a photon with toroidal topology? *Annales de la Fondation Louis de Broglie*, 1997, v. 22(2), 133–146.
10. Schwinger J. On Gauge Invariance and Vacuum Polarization. *Phys. Rev.*, 1951, v. 82, 664–679.
11. Huang K. On the Zitterbewegung of the Dirac Electron. *Am. J. Phys.*, 1952, v. 20, 479–484.
12. Bunge M. A picture of the electron. *Nuovo Cimento*, 1955, v. 1(6), 977–985.
13. Barut A.O., Bracken A.J. Zitterbewegung and the internal geometry of the electron. *Phys. Rev. D*, 1981, v. 23(10), 2454–2463.
14. Barut A.O., Zanghi N. Classical Model of the Dirac Electron. *Phys. Rev. Lett.*, 1984, v. 52, 2009–2012.
15. Hestenes D. The Zitterbewegung Interpretation of Quantum Mechanics. *Found. Phys.*, 1990, v. 20(10), 1213–1232.
16. Hestenes D. Zitterbewegung in Quantum Mechanics. arXiv:8002.2728.
17. Rivas M. Kinematical Theory of Spinning Particles. Kluwer, Dordrecht, 2001.
18. Gouanère M. A Search for the de Broglie Particle Internal Clock by Means of Electron Channeling. *Foundations of Physics*, 2008, v. 38, 659–664.
19. Hestenes D. Reading the Electron Clock. arXiv:0802.3227.
20. Rivas M. Measuring the internal clock of the electron. arXiv:0809.3635.
21. Bostick W. Mass, Charge and Current: The Essence and Morphology. *Physics Essays*, 1991, v. 4(1), 45–59.
22. Marinov K., Boardman A.D., Fedotov V.A. Metamaterial Toroidal. *New Journal of Physics*, 2007, v. 9, 324–335.
23. Zel'dovich Y. Electronic interaction with parity violation. *Zh. Eksp. Teor. Fiz.*, 1957, v. 33, 1184–1186.
24. Dubovik V.M., Tugushev. Toroid moments in electrodynamics and solid-state physics. *Physics Reports*, 1990, v. 187(4), 145–202.
25. Dubovik V.M., Kuznetsov. The toroid moment of Majorana neutrino. *Int. J. Mod. Phys.*, 1998, v. A13, 5257–5278.
26. Wood C.S. Measurement of parity nonconservation and an anapole moment in cesium. *Science*, 1997, v. 275, 1759–1763.
27. Ho C.M., Scherrer R.J. Anapole dark matter. *Phys. Lett. B*, 2013, v. 722, 341–346.
28. Consa O. G-factor and the Helical Solenoid Electron Model. viXra: 1702.0185.

Concerning the Dirac γ-Matrices Under a Lorentz Transformation of the Dirac Equation

G. G. Nyambuya

National University of Science and Technology, Faculty of Applied Sciences — Department of Applied Physics, Fundamental Theoretical and Astrophysics Group, P. O. Box 939, Ascot, Bulawayo, Republic of Zimbabwe
E-mail: physicist.ggn@gmail.com

We *embolden* the idea that the Dirac 4×4 γ-matrices are four-vectors where the space components (γ^i) represent spin and the forth component (γ^0) should likewise represent the time component of spin in the usual four-vector formalism of the Special Theory of Relativity. With the γ-matrices as four-vectors, it is seen that the Dirac equation admits two kinds of wavefunctions — (1) the usual four component Dirac bispinor ψ and (2) a scalar four component bispinor ϕ. Realizing this, and knowing forehand of the existing mystery as to why Leptons and Neutrinos come in pairs, we seize the moment and make the suggestion that the pair (ψ, ϕ) can be used as a starting point to explain mystery of why in their three generations $[(e^{\pm}, \nu_e), (\mu^{\pm}, \nu_\mu), (\tau^{\pm}, \nu_\tau)]$, Leptons and Neutrinos come in doublets. In this suggestion, the scalar-bispinor ϕ can be thought of as the Neutrino while the usual Dirac bispinor ψ can be thought of as the Lepton.

"We have found it of paramount importance that in order to progress we must recognize our ignorance and leave room for doubt."

— Richard Phillips Feynman (1918-1988)

1 Introduction

As taught to physics students through the plethora of textbooks available on our planet e.g., refs. [1–5], the Dirac 4×4 γ-matrices (γ^μ) are usually presented as objects that undergo a transformation during a Lorentz transformation of the Dirac [6, 7] equation. This issue of the transformation of these γ-matrices is not well represented in the literature [8]. There, thus, is a need to clear the air around this issue regarding the proper transformation properties of these matrices. To that end, we here argue in favour of these matrices as physical four-vectors and as such, they must under a Lorentz transformation transform as four-vectors. In-fact, it is well known that the γ^i-matrices ($i = 1, 2, 3$) represent spin (*i.e.*, $\vec{\mathcal{S}} = \frac{1}{2}\hbar\gamma^1\vec{i} + \frac{1}{2}\hbar\gamma^2\vec{j} + \frac{1}{2}\hbar\gamma^3\vec{k}$) because, together with the angular momentum operator ($\vec{\mathcal{L}}$), their sum total of the orbital angular momentum and spin ($\vec{\mathcal{J}} = \vec{\mathcal{L}} + \vec{\mathcal{S}}$) commutes with the Dirac Hamiltonian ($\mathcal{H}_D$), *i.e.* ($[\vec{\mathcal{J}}, \mathcal{H}_D] = 0$), implying that $\vec{\mathcal{J}}$ is a constant of motion.

For a particle whose rest-mass and Dirac [6, 7] wavefunction are m_0 and ψ respectively, the corresponding Dirac [6, 7] equation is given by:

$$\imath\hbar\gamma^\mu\partial_\mu\psi = m_0 c\psi, \tag{1}$$

where:

$$\gamma^0 = \begin{pmatrix} \mathcal{I}_2 & 0 \\ 0 & -\mathcal{I}_2 \end{pmatrix}, \quad \gamma^i = \begin{pmatrix} 0 & \sigma^i \\ -\sigma^i & 0 \end{pmatrix}, \tag{2}$$

are the 4×4 Dirac γ-matrices where $\mathcal{I}_2$ and 0 are the 2×2 identity and null matrices respectively, and $|\psi\rangle$ is the four component Dirac [6, 7] wave-function, $\hbar$ is the normalized Planck constant, c is the speed of light in vacuum, $\imath = \sqrt{-1}$, and:

$$\psi = \begin{pmatrix} \psi_0 \\ \psi_1 \\ \psi_2 \\ \psi_3 \end{pmatrix} = \begin{pmatrix} \psi_L \\ \\ \psi_R \end{pmatrix}, \tag{3}$$

is the 4×1 Dirac [6, 7] four component wavefunction and ψ_L and ψ_R are the Dirac [6,7] bispinors that are defined such that:

$$\psi_L = \begin{pmatrix} \psi_0 \\ \\ \psi_1 \end{pmatrix} \text{ and } \psi_R = \begin{pmatrix} \psi_2 \\ \\ \psi_3 \end{pmatrix}. \tag{4}$$

Throughout this reading — unless otherwise specified; the Greek indices will *here-and-after* be understood to mean ($\mu, \nu, \ldots = 0, 1, 2, 3$) and the lower case English alphabet indices ($i, j, k \ldots = 1, 2, 3$).

2 Lorentz Transformation of the Dirac as usually presented

To prove Lorentz Invariance (Covariance) two conditions must be satisfied:

1. *The first condition is that*: given any two inertial observers O and O′ anywhere in spacetime, if in the frame O we have:

$$[i\hbar\gamma^\mu\partial_\mu - m_0 c]\psi(x) = 0, \tag{5}$$

as the Dirac equation for the particle ψ, then:

$$[i\hbar\gamma^{\mu'}\partial_{\mu'} - m_0 c]\psi'(x') = 0 \tag{6}$$

is the equation describing the same state but in the frame O′.

2. *The second condition is that*: given that $\psi(x)$ is the wavefunction as measured by observer O, there must be a prescription for observer O′ to compute $\psi'(x')$ from $\psi(x)$ where $\psi'(x')$ describes to O′ the same physical state as that measured by O. The conserve must be true as-well, that is: there must exist a prescription such that starting from equation (6), one can arrive at (5).

In simpler mathematical terms, the above two requirements are saying that: starting from equation (5), there must exist some physically legitimate transformations within the framework of Lorentz transformations that can take (map) us from this equation (5) to equation (6) and *vice-versa*. If we can find these, then, the Dirac equation is said to be Lorentz Invariant (Covariant).

Now, since the Lorentz transformations are linear, it is to be required or expected of the transformations between $\psi(x)$ and $\psi'(x')$ to be linear too, *i.e.*:

$$\psi'(x') = \psi'(\Lambda x) = S(\Lambda)\psi(x) = S(\Lambda)\psi(\Lambda^{-1}x'), \qquad (7)$$

where $S(\Lambda)$ is a 4×4 matrix which depends only on the relative velocities of O and O′ and Λ is the Lorentz transformation matrix. $S(\Lambda)$ has an inverse if O $\rightarrow$ O′ and also O′ $\rightarrow$ O. The inverse is:

$$\psi(x) = S^{-1}(\Lambda)\psi'(x') = S^{-1}(\Lambda)\psi'(\Lambda x), \qquad (8)$$

or we could write:

$$\psi(x) = S(\Lambda^{-1})\psi'(\Lambda x) \Longrightarrow S(\Lambda^{-1}) = S^{-1}(\Lambda). \qquad (9)$$

We can now write equation (5), as:

$$\left[i\hbar\gamma^{\mu}\frac{\partial x^{\mu'}}{\partial x^{\mu}}\partial_{\mu'} - \mathrm{m}_0 c\right]S^{-1}(\Lambda)\psi'(x') = 0, \qquad (10)$$

and multiplying this from the left by $S(\Lambda)$, we have:

$$S(\Lambda)\left[i\hbar\gamma^{\mu}\frac{\partial x^{\mu'}}{\partial x^{\mu}}\partial_{\mu'} - \mathrm{m}_0 c\right]S^{-1}(\Lambda)\psi'(x') = 0, \qquad (11)$$

and hence:

$$\left[i\hbar S(\Lambda)\gamma^{\mu}\frac{\partial x^{\mu'}}{\partial x^{\mu}}S^{-1}(\Lambda)\partial_{\mu'} - \mathrm{m}_0 c\right]\psi'(x') = 0. \qquad (12)$$

Therefore, for the above equation to be identical to equation (6) (hence Lorentz Invariant), the requirement is that:

$$\gamma^{\mu'} = S(\Lambda)\gamma^{\mu}\frac{\partial x^{\mu'}}{\partial x^{\mu}}S^{-1}(\Lambda), \qquad (13)$$

hence, we have shown that — for as long as $S^{-1}(\Lambda)$ exists, equation (5) is Lorentz Invariant.

3 Dirac $4\vec{\times}4\,\vec{\gamma}$-matrices as a four-vector

The Dirac equation (1) can be re-written in the traditional Schrödinger formulation as ($\mathcal{H}\psi = \mathcal{E}\psi$) where $\mathcal{H}$ and $\mathcal{E}$ are the energy and Hamiltonian operators respectively. In this Schrödinger formulation, $\mathcal{H}$, will be such that it is given by:

$$\mathcal{H} = \gamma^0 \mathrm{m}_0 c^2 - \imath\hbar c\gamma^0\gamma^j\partial_j, \qquad (14)$$

and ($\mathcal{E} = i\hbar\partial/\partial t$).

Now, according to the quantum mechanical equation governing the evolution of any quantum operator Q, we know that:

$$\imath\hbar\frac{\partial Q}{\partial t} = Q\mathcal{H} - \mathcal{H}Q = [Q, \mathcal{H}], \qquad (15)$$

hence, if:

$$[Q, \mathcal{H}] \equiv 0, \qquad (16)$$

then, the quantum mechanical observable corresponding to the operator Q is a conserved physical quantity.

With this [equation (15)] in mind, Dirac asked himself the natural question — what the "strange" new γ-matrices appearing in his equation really represent. What are they? In-order to answer this question, he decided to have a "look" at or make a closer "inspection" of the quantum mechanical orbital angular momentum operator $\mathcal{L}_i$ which we all know to be defined:

$$\mathcal{L}_i = (\vec{r}\times\vec{p})_i = -\imath\hbar\epsilon_{ijk}x_j\partial_k, \qquad (17)$$

where, ϵ_{ijk} is the completely-antisymmetric three dimensional *Levi-Civita* tensor. In the above definition of $\mathcal{L}_i$, the momentum operator $\vec{p}$ is the usual quantum mechanical operator, *i.e.*:

$$\vec{p} = -\imath\hbar\vec{\nabla} \qquad \Rightarrow \qquad p_i = \imath\hbar\partial_i. \qquad (18)$$

From this definition of $\mathcal{L}_i$ given in equation (17), it follows from equation (15) that $\imath\hbar\partial\mathcal{L}_i/\partial t = [\mathcal{L}_i, \mathcal{H}]$, will be such that:

$$\imath\hbar\frac{\partial\mathcal{L}_i}{\partial t} = -\imath\hbar\mathrm{m}_0 c^2\epsilon_{ijk}\left[x_j\partial_k, \gamma^0\right] + \hbar^2 c\epsilon_{ijk}\left[x_j\partial_k, \gamma^0\gamma^l\partial_l\right]. \qquad (19)$$

Now, because the term $\gamma^0\mathrm{m}_0c^2$ is a constant containing no terms in p_i, it follows from this very fact that ($\epsilon_{ijk}\left[x_j\partial_k, \gamma^0\right] \equiv 0$), hence equation (19) will reduce to:

$$\begin{aligned}\imath\hbar\frac{\partial\mathcal{L}_i}{\partial t} &= \hbar^2 c\epsilon_{ijk}\gamma^0\gamma^l\left[x_j\partial_k, \partial_l\right] \\ &= \hbar^2 c\epsilon_{ijk}\gamma^0\gamma^l\left(x_j\partial_k\partial_l - \partial_l x_j\partial_k\right).\end{aligned} \qquad (20)$$

From the commutation relation of position (x_i) and momentum ($-\imath\hbar\partial_j$) due to the Heisenberg uncertainty principle [9], namely ($-\imath\hbar\left[x_i, \partial_j\right] = -\imath\hbar\delta_{ij}$) where δ_{ij} is the usual Kronecker-delta function, it follows that if in equation (20), we substitute ($\partial_l x_j = x_j\partial_l + \delta_{lj}$), this equation is going to reduce to:

$$\imath\hbar\frac{\partial\mathcal{L}_i}{\partial t} = \hbar^2 c\epsilon_{ijk}\gamma^0\gamma^l\underbrace{\left(x_j\partial_k\partial_l - x_j\partial_l\partial_k\right)} + \hbar^2 c\epsilon_{ijk}\gamma^0\gamma^l\delta_{lj}\partial_k. \qquad (21)$$

The term with the under-brace vanishes identically, that is to say: $(x_j\partial_k\partial_l - x_j\partial_l\partial_k \equiv 0)$; and $(\epsilon_{ijk}\gamma^0\gamma^j\delta_{lj} = \epsilon_{ilk}\gamma^0\gamma^j)$, it follows from this that equation (21), will reduce to:

$$\imath\hbar\frac{\partial\mathcal{L}_i}{\partial t} = \hbar^2 c\epsilon_{ilk}\gamma^0\gamma^j\partial_k. \tag{22}$$

Since this result [*i.e.*, equation (22) above] is non-zero, it follows from the dynamical evolution theorem [*i.e.*, equation (16)] of Quantum Mechanics (QM) that none of the angular momentum components $\mathcal{L}_i$ are — *for the Dirac particle* — going to be constants of motion. This result obviously bothered the great and agile mind of Paul Dirac. For example, a non-conserved angular momentum would mean spiral orbits *i.e.*, Dirac particles do not move in fixed and well defined orbits as happens with electrons of the Hydrogen atom for example; at the very least, this is very disturbing because it does not tally with observations. The miniature beauty that Dirac had — had the rare privilege to discover and, the first human being to "see" with his beautiful and great mind — this — had to be salvaged* somehow.

Now — *enter spin*! Dirac figured that "*Subtle Nature*" must conserve something redolent with orbital angular momentum, and he considered adding something to $\mathcal{L}_i$ that would satisfy the desired conservation criterion, *i.e.*: call this unknown, mysterious and arcane quantity $\mathcal{S}_i$ and demand that:

$$\imath\hbar\frac{\partial(\mathcal{L}_i + \mathcal{S}_i)}{\partial t} \equiv 0. \tag{23}$$

This means that this strange quantity $\mathcal{S}_i$ must be such that:

$$\imath\hbar\frac{\partial\mathcal{S}_i}{\partial t} = [\mathcal{S}_i, \mathcal{H}] = -\hbar^2 c\epsilon_{ilk}\gamma^0\gamma^j\partial_k. \tag{24}$$

Solving equation (24) for $\mathcal{S}_i$, Dirac arrived at:

$$\mathcal{S}_i = \frac{1}{2}\hbar\begin{pmatrix} \sigma_i & 0 \\ 0 & \sigma_i \end{pmatrix} = \frac{1}{2}\hbar\gamma^5\gamma^i, \tag{25}$$

where $(\gamma^5 = \imath\gamma^0\gamma^1\gamma^2\gamma^3)$, is the usual Dirac gamma-5 matrix.

Now, realising that:

1. The matrices σ_i are Pauli matrices and they had been *ad hocly* introduced in 1925 into physics to account for the spin of the Electron by the Dutch-American theoretical physicists, George Eugene Uhlenbeck (1900–1988) and his colleague, Samuel Abraham Goudsmit (1902–1978) [10].
2. His equation — when taken in the non-relativistic limit, it would account for the then unexplained gyromagnetic ratio (g = 2) of the Electron and this same equation emerged with σ_i explaining the Electron's spin.

*Such is the indispensable attitude of the greatest theoretical physicists that ever graced the face of planet Earth — beauty must and is to be preserved; this is an ideal for which they will live for, and if needs be, it is an ideal for which they will give-up their life by taking a gamble to find that unknown quantity that restores the beauty glimpsed!

The agile Paul Dirac seized the golden moment and forthwith identified $\mathcal{S}_i$ with the ψ-particle's spin. The factor $\frac{1}{2}\hbar$ in $\mathcal{S}_i$ implies that the Dirac particle carries spin $1/2$, hence, the Dirac equation (1) is an equation for a particle with spin $1/2$!

While in this esoteric way (*i.e.*, as demonstrated above) Dirac was able to explain and "demystify" Wolfgang Pauli (1900–1958)'s strange spin concept which at the time had only been inserted into physics by "*the sleight of hand*" out of an *unavoidable necessity*, what bothers us (*i.e.*, myself) the most is:

> *How it comes about that we (physicists) have had issues to do with the transformational properties of the γ-matrices? Why? Really — why? The fact that orbital angular momentum $\vec{\mathcal{L}}$ is a vector invariably leads to the indelible fact that $\vec{\mathcal{S}}$ is a vector as-well, because we can only add vectors to vectors.*

If $\vec{\mathcal{S}}$ is a vector, then the matrices γ^i must be components of a 3-vector, so must the matrix γ^0 be the component of the time-vector in the usual four-vector formalism, hence γ^μ must be a four-vector. So, right from the word go — with little or no resistance whatsoever, it must have been pristine clear that the γ-matrices must be four-vectors.

4 Dirac equation with the $\vec{\gamma}$-matrices as a four-vector

With γ-matrices now taken as a four-vector, the object $\gamma^\mu\partial_\mu$ is a scalar, the meaning of which is that the Dirac equation will now accommodate two types of spinors "*the usual Dirac bispinor*" and a new "*scalar-bispinor*", *i.e.*:

1. **A spinor that is a scalar**. Let us here call this a scalar-bispinor and let us denote it with the symbol ϕ and because of its scalar nature — under a Lorentz transformation, we will have $(\phi' = \phi)$. Just like the ordinary Dirac wavefunction ψ is a 4×1 component object, ϕ is also a 4×1 object, *i.e.*:

$$\phi = \begin{pmatrix} \phi_0 \\ \phi_1 \\ \phi_2 \\ \phi_3 \end{pmatrix} = \begin{pmatrix} \phi_L \\ \\ \phi_R \end{pmatrix}, \tag{26}$$

   where ϕ_L and ϕ_R are the scalar-spinors — which are like the ordinary left and right handed Dirac spinors (ψ_L, ψ_R); ψ_L and ϕ_R are defined:

$$\phi_L = \begin{pmatrix} \phi_0 \\ \\ \phi_1 \end{pmatrix} \text{ and } \phi_R = \begin{pmatrix} \phi_2 \\ \\ \phi_3 \end{pmatrix}. \tag{27}$$

   Consideration of the scalar-bispinor has been made in the past by others e.g., [11].
2. **The ordinary Dirac bispinor** ψ: that transforms linearly under a Lorentz transformation *i.e.* $(\psi' = S\psi)$,

where, a usual, Lorentz Invariance (Covariance) requires that the function $S = S(x^\mu, \dot{x}^\mu)$ be such that:

$$\gamma^{\mu'}\partial_{\mu'}S = \gamma^\mu\partial_\mu S = 0, \tag{28}$$

and:

$$\gamma^\mu = S^{-1}\gamma^\mu S, \tag{29}$$

which implies:

$$[S, \gamma^\mu] = 0. \tag{30}$$

Now, we certainly must ask "*What does this all mean*". That is to say, the fact that the Dirac equation allows for the existence of the usual Dirac bispinor ψ and in addition to that — a scalar-bispinor ϕ? Taken at the same level of understanding that the Dirac equation's prediction of the existence of antimatter is premised on the Dirac equation being symmetric under charge conjugation — on that very same level of understanding, this fact that the Dirac equation in its most natural and un-tempered state as presented herein — it, allows for the existence of the usual Dirac bispinor ψ and scalar-bispinor ϕ; in the same vein of logic, this naturally implies that for every Dirac bispinor ψ, there must exist a corresponding scalar-bispinor ϕ. That is, the Dirac bispinor ψ and the scalar-bispinor ϕ must come in pairs. There is no escape from this train of logic.

If we are thinking of Leptons and Neutrinos, the above pair-picture of (ψ, ϕ) makes perfect sense. Based on this picture, we can write the Dirac equation for this pair (ψ, ϕ) as:

$$\imath\hbar\gamma^\mu\partial_\mu \begin{pmatrix} \psi \\ \\ \phi \end{pmatrix} = \mathrm{m}_0 c \begin{pmatrix} 1 & 0 \\ 0 & \eta \end{pmatrix} \begin{pmatrix} \psi \\ \\ \phi \end{pmatrix}, \tag{31}$$

where η is a scalar-constant that we have introduced so as to accommodate the possibility that the particle-pair (ψ, ϕ), may have different masses. In this way, one can begin to entertain ideas on how to explain the Lepton-Neutrino pairing $[(e^\pm, \nu_e), (\mu^\pm, \nu_\mu), (\tau^\pm, \nu_\tau)]$. We have no intention of doing this or going any deeper on this matter but merely to point out — as we have just done — that, this idea may prove a viable avenue of research to those seeking an explanation of why this mysterious pairing occurs in nature.

5 General discussion

We must categorically state that — *what we have presented herein is not new at all*. All we have endeavoured is to make bold the point that the γ-matrices constitute a four-vector. Perhaps the only novelty there is — in the present contribution — is the suggestion that we have made — namely that, the resulting scalar-bispinor (ϕ) and the usual Dirac bispinor (ψ) can be used as a starting point to explain the currently open problem of the three generation Lepton-Neutrino pairing $(e^\pm, \nu_e)$, $(\mu^\pm, \nu_\mu)$ and $(\tau^\pm, \nu_\tau)$; where the scalar-bispinor can be assumed to be the Neutrino while the usual Dirac bispinor can be thought of the Lepton. In the sequatial reading [12], we will demonstrate how this formulation of the Dirac equation can be used to explain how massless neutrinos can oscillate.

Acknowledgements

We are grateful for the assistance rendered unto us by the National University of Science and Technology's Research Board toward our research endeavours.

Submitted on March 16, 2018

References

1. Itzykson C. and Zuber J.-B. Quantum Mechanics II. McGraw-Hill, New York, USA, 1980.
2. Messiah A. Quantum Mechanics II. North-Holland Publishing Company, Amsterdam, Netherland, second edition, 1962.
3. Sakurai J. J. Advanced Quantum Mechanics. Addison-Wesley Publishing Company, Massachusetts, USA, 1967.
4. Schweber S. S. An Introduction to Relativistic Quantum Field Theory. Row, Peterson and Company, New York, USA, 1961.
5. Zee A. Quantum Field Theory in a Nutshell. Princeton University Press, USA, second edition, 2010.
6. Dirac P. A. M. The Quantum Theory of the Electron. *Proceedings of the Royal Society of London A: Mathematical, Physical and Engineering Sciences*, 1928, v.117(778), 610–624.
7. Dirac P. A. M. The Quantum Theory of the Electron. Part II. *Proceedings of the Royal Society of London A: Mathematical, Physical and Engineering Sciences*, 1928, v. 118(779), 351–361.
8. Nikolić H. How (Not) To Teach Lorentz Covariance of the Dirac Equation. *European Journal of Physics*, 2014, v.35(3), 035003.
9. Heisenberg W. Ueber den anschaulichen Inhalt der quantentheoretischen Kinematik and Mechanik. *Zeitschrift für Physik*, 1927, v.43, 172–198. *Engilish Translation*: Wheeler J. A. and Zurek W. H. (eds) Quantum Theory and Measurement. Princeton (NJ), Princeton University Press, 1983, 62–84.
10. Uhlenbeck G. E. and Goudsmit S. Ersetzung der Hypothese vom unmechanischen Zwang durch eine Forderung bezüglich des inneren Verhaltens jedes einzelnen Elektrons. *Die Naturwissenschaften*, 1925, v.13(47), 953–954.
11. Chapman T. C. and Leiter D. J. On the Generally Covariant Dirac Equation. *American Journal of Physics*, 1976, v.44(9), 858–862.
12. Nyambuya G. G. Oscillating Massless Neutrinos. *Progress in Physics*, 2018, v. 14, 94–98.

Oscillating Massless Neutrinos

G. G. Nyambuya

National University of Science and Technology, Faculty of Applied Sciences — Department of Applied Physics, Fundamental Theoretical and Astrophysics Group, P. O. Box 939, Ascot, Bulawayo, Republic of Zimbabwe
E-mail: physicist.ggn@gmail.com

The phenomenon of neutrino oscillations requires that not only should neutrinos be massive but that these masses be unique. How they acquire this mass remains an *open question*. Various mechanisms have been proposed to explain this phenomenon of neutrino oscillations. Herein, we propose — *the simplest imaginable* — alternative mechanism which operates *via* coupling the massless neutrino to a massive Dirac scalar. This massive Dirac scalar is a new hypothetical particle that we — *unfortunately* — can not observe directly because of its point-particle nature. Further, this massive Dirac scalar comes in as an integral part of the neutrino system — it [massive Dirac scalar] oscillates between three states, thus leading to the observed neutrino oscillations. This model predicts neutrinos are Dirac in nature and not Majorana.

> "Just by studying mathematics we can hope to make a guess at the kind of mathematics that will come into the physics of the future."
>
> — Paul A. M. Dirac (1902-1984)

1 Introduction

According to Albert Einstein (1879–1955)'s Special Theory of Relativity (STR) [1], the energy E and momentum p of a massless ($m_0 = 0$) are related by the energy-momentum equation ($E = pc$), where c is the speed of Light in *vacuo*. In accordance with the dictates of wave mechanics/phenomenon, the group velocity, v_g:

$$v_g = \frac{\partial E}{\partial p}\,, \tag{1}$$

of a particle whose energy and momentum are related by ($E = pc$) is equal to the speed of Light in *vacuo*, *i.e.* ($v_g = c$). All indications are that the neutrino travels at the *vacuo* speed of Light, c, thus prompting physicists to assume that the neutrino is massless. Be that as it may, a massless neutrino pauses a problem to the physicist in that one can not explain the all-important experimentally [2–5] verified and common-place phenomenon of *neutrino oscillation*.

First predicted [6, 7] in 1957 by the Italian nuclear physicist — Bruno Pontecorvo (1913–1993), and observed in 1968 by the America chemist and physicist — Raymond Davis Jr. (1914–2006) et al. [8], neutrino oscillation is a quantum mechanical phenomenon whereby a neutrino created with a specific lepton flavour (electron ν_e, muon ν_μ, or tau ν_τ) can be measured at a latter time to have a different flavour. The probability of measuring a particular flavour for a neutrino varies between the three known flavour states (ν_e, ν_μ, ν_τ) as it propagates through the intestacies of space. From a theoretical standpoint, two conditions are necessary for neutrinos to oscillate — *i.e.*, to change from one type to the other, *e.g.*, from an Electron-neutrino (ν_e) to a Muon-neutrino (ν_μ) or *vice-verse*, and these conditions are:

1. Neutrinos *must* have a *non-zero mass*, and this mass *cannot be identical* for all the three neutrino flavours (ν_e, ν_μ, ν_τ).
2. There *must be no rigorous law forbidding* a transition between neutrino species, the meaning of which is that these transitions are purely probabilistic in nature.

Since the coming to light or since the "conception" of this important question *i.e.*, the question of how neutrino masses arise — this question, has not been answered conclusively [9]. In the *Standard Model* of particle physics, fermions only have mass because of interactions with the *Higgs Field*. Do neutrinos generate their mass *via* the *Higgs Mechanism* [10–12] as-well? This is a question that needs an answer. We here do not claim to give a definitive answer to this question, but merely a suggestion — *perhaps*, a suggestion that one might consider worthy of their attention.

That said, we must here at the penultimate of this introductory section make clear the scope of the present letter — *i.e.*, while this letter presents — *in our feeble view*, a new model whose endeavour is to explain neutrino oscillations, we present this model only as an alternative to existing explanations on this phenomenon. We deliberately avoid an in-depth comparative analysis of these models with the present and this we have done in-order that our ideas are clearly presented without overshadowing them with existing ideas on the same endeavour.

2 Massless Dirac particle

First considered by the German mathematician, mathematical physicist and philosopher — Hermann Klaus Hugo Weyl (1885–1955); a massless Dirac particle is described by the following Dirac-Weyl [13] equation:

$$\imath\hbar\gamma^\mu\partial_\mu\psi = 0, \tag{2}$$

where ($\imath = \sqrt{-1}$), ∂_μ is the four spacetime partial derivatives, $\hbar$ is the normalized Planck constant, γ^μ are the four 4×4 Dirac matrices and ψ is the usual 4×1 component Dirac wavefunction.

In this letter, the gamma matrices shall be assumed to be four vectors the meaning of which is that they transform like vectors *i.e.*:

$$\gamma^{\mu'} = \frac{\partial x^{\mu'}}{\partial x^\mu}\,\gamma^\mu. \tag{3}$$

This assumption of treating the γ-matrices as four vectors may appear strange and if not completely and outright wrong. Be that as it may, in the letter [14], this idea of treating the γ-matrices as vectors as been justified. As argued therein the said letter [14], once the γ-matrices are four vectors, ψ can take three forms:

1. It [ψ] can be a zero ranks scalar.
2. It [ψ] can be a four 4×1 component scalar where the four components are zero ranks scalar objects.
3. Provided a certain transformational condition is met [*i.e.*, the condition given in equation (28) of [14]], it [ψ] can be the typical Dirac spinor.

In the subsequent section, we shall look at the scalar version.

3 Scalar coupled massive Dirac particle

For a moment, suppose we couple the massless ψ-particle to a massive ϕ-scalar particle, that is to say, we have ψ interfere with ϕ in such a way that the resulting 4×1 component Dirac wavefunction of the interference Ψ, is such that:

$$\Psi = \phi\psi. \tag{4}$$

The ϕ-particle is a simple (zero-rank) scalar, *i.e.*, unlike the ψ-particle which is a 4×1 component object, ϕ has no components, it is a zero rank mathematical object. Together, ϕ and ψ make a complete quantum mechanical particle *i.e.*, they satisfy the quantum probability normalization condition:

$$\iiint_{\forall\, S\,pace} (\phi\psi)^\dagger\,(\phi\psi)\,dxdydz = 1, \tag{5}$$

and as individuals (ϕ, ψ), they do not satisfy the quantum probability normalization condition required for a complete quantum mechanical particle *i.e.*:

$$0 < \iiint_{\forall\, S\,pace} \phi^\dagger\phi dxdydz < 1, \tag{6}$$

and:

$$0 < \iiint_{\forall\, S\,pace} \psi^\dagger\psi dxdydz < 1. \tag{7}$$

Now, substituting ($\Psi = \phi\psi$) into equation (2), we will have:

$$\imath\hbar\gamma^\mu\phi\partial_\mu\psi = -\imath\hbar\gamma^\mu\left(\partial_\mu\phi\right)\psi. \tag{8}$$

If ϕ is a massive particle satisfying the equation:

$$-\imath\hbar\gamma^\mu\partial_\mu\phi = m_0 c\phi, \tag{9}$$

where ($m_0 \neq 0$), then, equation (8), becomes:

$$\imath\hbar\gamma^\mu\phi\partial_\mu\psi = m_0 c\phi\psi, \tag{10}$$

hence:

$$\imath\hbar\gamma^\mu\partial_\mu\psi = m_0 c\psi. \tag{11}$$

Equation (11) is the Dirac [15, 16] equation describing a massive particle of mass m_0 and it is this equation that is used to describe neutrino oscillations. Thus, the neutrino as described by Ψ is now a massive particle — the meaning of which is that one can now describe neutrino oscillations which require a non-zero mass. It is important at this juncture that we state the obvious, namely that — just as the ψ-particle is a spin-1/2 particle, the ϕ-particle is likewise a spin-1/2 particle. As pointed out in the pernultimate of the previous section, we must remind the reader at this point that equation (9) with ϕ as a scalar has been justified in the letter [14]. That is to say, as justified therein the letter [14], the γ-matrices have here been assumed to be four vectors, hence equation (9).

While neutrino oscillations strongly point to the existence of unique non-zero mass for the three neutrino flavours, these oscillations do not directly mean the mass of these neutrinos is non-zero (*e.g.*, [17]). Only direct experimental observations as deliver a definitive answer to the question (*e.g.*, [17]). A number of experiments have been dedicated to this effect and these experiments place upper limits with not definitive and precise value being pinned down.

4 Dirac scalar particle

While the ϕ-scalar particle is operated on by the usual Dirac operator, it is not an ordinary Dirac particle because an ordinary Dirac particle is described by a 4×1 component wavefunction and not a zero rank scalar. Consequently, the question that naturally and immediately comes to mind is whether this Dirac [15, 16] equation (9) describing this scalar particle is a valid equation. To answer this — just as is the case with the Dirac [15, 16] equation, the validity of this equation is to judged on whether or not this equation (9) yields reasonable energy solutions for the case of a free scalar. As usual, the free particle solution of the new hypothetical Dirac scalar is:

$$\phi = \phi_0 e^{\imath p_\mu x^\mu/\hbar}, \tag{12}$$

where ϕ_0 is a normalization constant, p_μ and x^μ are the four momentum and position of this scalar particle. Substituting ϕ as given in equation (12) into equation (9), and thereafter performing some algebraic operations and clean-up, one obtains the following set of four simulations equations:

$$\begin{aligned}
&(E - \mathrm{m}_0c^2) - c(p_x - ip_y) - cp_z = 0 \quad \ldots \quad \text{(a)}\\
&(E - \mathrm{m}_0c^2) - c(p_x + ip_y) + cp_z = 0 \quad \ldots \quad \text{(b)}\\
&(E + \mathrm{m}_0c^2) - c(p_x - ip_y) - cp_z = 0 \quad \ldots \quad \text{(c)}\\
&(E + \mathrm{m}_0c^2) - c(p_x + ip_y) + cp_z = 0 \quad \ldots \quad \text{(d)}
\end{aligned} \tag{13}$$

Adding together equations (13a) and (13b), one obtains:

$$E = p_x c + m_0 c^2, \tag{14}$$

and likewise, adding together equations (13c) and (13d), one obtains:

$$E = p_x c - m_0 c^2. \tag{15}$$

Undoubtedly, the solutions (14) and (15), are indeed acceptable solutions — hence, the scalar Dirac [15,16] equation (9), is as a result, an acceptable equation describing this hypothetical Dirac scalar particle. The question now is what do these solutions (14) and (15) mean?

First — we must notice that these solutions (14) and (15) tell us that the energy of the ϕ-scalar particle is determined by this particle's momentum along the x-axis. If this particle did have a non-zero momentum along the other two axis *i.e.*, the y and z-axis, what the equations (14) and (15) are telling us, is that this momentum is of no consequence whatsoever in determining the energy of this particle. This does not make sense. The only reasonable solution to this dilemma is to assume that ($p_y = p_z = 0$) and ($p_x \neq 0$). This means that the ϕ-particle only moves along the x-axis and nothing else. If this is the case that it only moves along the x-axis, then — clearly, this ϕ-particle can not be an extended particle, but a point-particle. If the ϕ-particle is indeed a point-particle, it must be invisible hence non-detectable. This not only a natural conclusion to reach, but a logical one.

Second — we have the two solutions equation (14) and (15) having different energies. What does this mean? One way to look at this is to assume that there exists two such particles with each having different energies. The other would be to assume that there is just one ϕ-particle — *albeit*, with the mass *discretely fluctuating* between the two mass extremums *i.e.*, $(-m_0)$ and $(+m_0)$. That is to say, the ϕ-particle is unstable and its instability is naturally transmitted to the neutrino *via* the $(\phi - \psi)$-coupling. As the unobservable ϕ-particle changes its energy state, it will excite and de-excite the observable neutrino into the energy states of the other two flavours. If the mass only fluctuated between the two mass extremums *i.e.*, $(-m_0)$ and $(+m_0)$, it would mean the neutrino would fluctuate between two states only, without it returning to its natural state. We know that a neutrino of any type will fluctuate between all the three states. In-order for the neutrino to enter its natural state, there is need for ϕ to enter into a third eigenstate of is mass. Naturally, this must be the eigenstate ($m_0 = 0$). Therefore, the ϕ-particle will discretely fluctuate between the three states $(-m_0, 0, +m_0)$ and each of these states corresponds to a particular value of energy which switches the neutrino to the right energy state of a given neutrino state.

5 The neutrino oscillations

How do these oscillations in the particle's state occur in the present model? Just as happens in *quantum gauge transformations* — for an answer to this very important question, we envisage a discrete *gauge-transformation-like* spontaneous and random change in the state of the ϕ-particle occurs in the phase *i.e.*:

$$\phi \longmapsto e^{i\chi_i}\phi, \tag{16}$$

where χ is some continuous and differentiable smooth function of the four position x^μ and or four momentum p^μ. In-order to preserve the composite-state ψ, such a change as that given in equation (16) is to be simultaneously met with a corresponding conjugate change in the phase of the neutrino, *i.e.*:

$$\psi \longmapsto e^{-i\chi_i}\psi, \tag{17}$$

and these two changes, leave the ψ-state unchanged, *i.e.*:

$$\psi \longmapsto \left(e^{i\chi_i}\phi\right)\left(e^{-i\chi_i}\psi\right) = \phi\psi = \psi. \tag{18}$$

We expect that there be three phase changes corresponding to the three mass states $(-m_0, 0, +m_0)$, hence three energy states.

The phase change given in equation (16) leads the scalar Dirac equation (9), to transform and become:

$$-\imath\hbar\gamma^\mu\partial_\mu\phi = \left(m_0 + m_j^*\right)c\phi, \tag{19}$$

while the phase change given in equation (17) leads to the Dirac equation (11) for the neutrino, to transform and become:

$$\imath\hbar\gamma^\mu\partial_\mu\psi = \left(m_0 + m_j^*\right)c\psi, \tag{20}$$

where the three-state fluctuating mass m_j^* is such that:

$$m_j^* = \frac{\hbar\gamma^\mu\partial_\mu\chi_i}{c}. \tag{21}$$

In the following subsections, we discuss the possible oscillations of the neutrino for all the three neutrino flavours.

5.1 Oscillations of the Electron-neutrino state

Presented in the self-explanatory diagram in Figure (1) is a graphic visual of the six possible transitions of the natural Electron-neutrino. That is, when the ϕ-particle's mass is zero ($m_0 = 0$), the Electron-neutrino is in its natural state of being an Electron-neutrino. Further, when the mass of the ϕ-particle is negative $(-m_0)$, the Electron-neutrino is in enters the μ-neutrino state and likewise, when mass of the ϕ-particle is positive $(+m_0)$, Electron-neutrino enters the τ-neutrino state.

5.2 Oscillations of the Muon-neutrino state

Just as in Figure (1), we have in Figure (2) a graphic visual of the four possible transitions of natural Muon-neutrino. When the ϕ-particle's mass is zero ($m_0 = 0$), the Muon-neutrino is in its natural state of being an Muon-neutrino. When the mass of the ϕ-particle is negative $(-m_0)$, the Muon-neutrino is in enters the Electron-neutrino state and likewise, when mass of the ϕ-particle is positive $(+m_0)$, Muon-neutrino enters the τ-neutrino state.

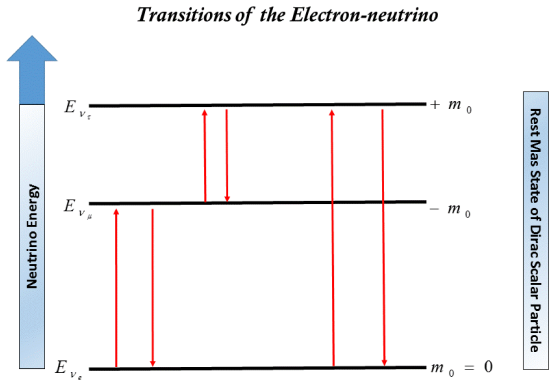

Fig. 1: The six possible transitions of the Electron-neutrino.

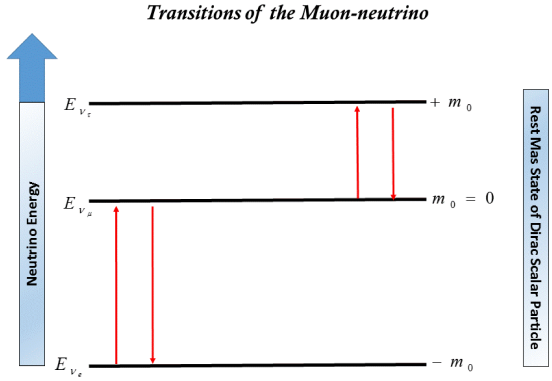

Fig. 2: The four possible transitions of the Muon-neutrino.

5.3 Oscillations of the Tau-neutrino state

Again, just as is the case in the previous cases, Figure (3) is a graphic presentation of the six possible transitions of natural Tau-neutrino. When the ϕ-particle's mass is zero ($m_0 = 0$), the Tau-neutrino is in its natural state of being an Tau-neutrino and when the mass of the ϕ-particle is negative ($-m_0$), the Tau-neutrino enters the Electron-neutrino state and likewise, when mass of the ϕ-particle is positive ($+m_0$), Muon-neutrino enters the μ-neutrino state.

6 General discussion

Clearly, without casting away any of the existing theories (*e.g.*, [17–19]) whose endeavour is to explain the mystery behind the neutrino oscillations, we here have provided an alternative explanation *via* what appears to us to be a mathematically permissible mechanism whereby the massless neutrino is coupled to an unobservable and unstable scalar Dirac point-particle. The resulting mathematics thereof requires that this hypothetical Dirac scalar must be a point-particle. From a physics standpoint, this point-particle nature of the ϕ-scalar implies that this particle can not be observed in nature because it is not an extended particle like the Electron, Proton, Neutrino *etc*. So, we should not expect to observe this particle

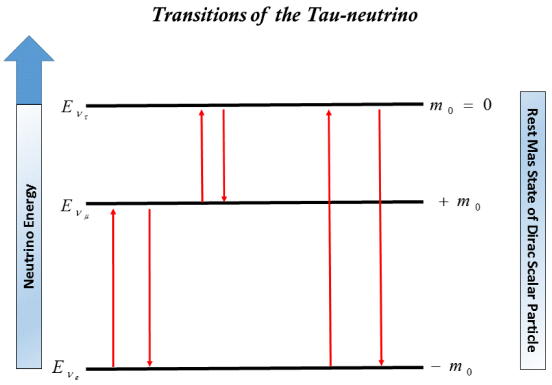

Fig. 3: The six possible transitions of the Tau-neutrino.

at all. We can only assign it to be a property of the neutrino particle — with it, being the "*culprit*" behind the observed phenomenon of neutrino oscillation.

Interestingly, within the context of the present model, one can answer the paramount question of whether of not neutrinos are Majorana or Dirac in nature. Majorana neutrinos satisfy the Majorana [20] equation while Dirac neutrinos satisfy the usual massive Dirac equation (11). In the present model, for these neutrinos to be Majorana, the Dirac scalar must be Majorana too, that is to say, the scalar Dirac equation (9), will have to be such that:

$$-\imath\hbar\gamma^\mu\partial_\mu\phi = m_0 c\gamma^2\phi. \tag{22}$$

With equation (22) in place, equation (11) will as a consequence thereof, reduce to the [20] equation, *i.e.*:

$$\imath\hbar\gamma^\mu\partial_\mu\psi = m_0 c\gamma^2\psi, \tag{23}$$

Now, substituting the free particle solution of the ϕ-scalar given in equation (12) into equation (22), just as in equation (13), one obtains the following set of four simulations equations:

$$\begin{aligned}
&(E + \imath m_0c^2) - c(p_x - ip_y) - cp_z = 0 \quad \ldots \quad \text{(a)}\\
&(E + \imath m_0c^2) - c(p_x + ip_y) + cp_z = 0 \quad \ldots \quad \text{(b)}\\
&(E - \imath m_0c^2) - c(p_x - ip_y) - cp_z = 0 \quad \ldots \quad \text{(c)}\\
&(E - \imath m_0c^2) - c(p_x + ip_y) + cp_z = 0 \quad \ldots \quad \text{(d)}
\end{aligned} \tag{24}$$

Adding together equations (24a) and (24b), corresponding to equation (14), one obtains:

$$E = p_x c - \imath m_0 c^2, \tag{25}$$

and likewise, adding together equations (24c) and (24d), corresponding to equation (15), one obtains:

$$E = p_x c + \imath m_0 c^2. \tag{26}$$

In contrast to the solutions given in equations (14) & (15), these solutions equation (25) & (26), are complex. As a rule

of quantum mechanics, energy eigenvalues must be real. What this means is that we must reject these solutions [*i.e.*, equations (25) & (26)], and with them, the premise on which they are founded, namely that neutrinos are Majorana. One can try and save the Majorana model by invoking an imaginary mass so that the energy is real, but this will sure not work for so long as mass is a quantum mechanical observable because quantum mechanics will require that the mass be real thus leaving us exactly where we started off *i.e.*, with complex energy states, hence, in-accordance with the present model, neutrinos can not be Majorana, but can only be Dirac in nature.

7 Conclusion

Assuming that what has been presented in the present letter is acceptable, one can put forward the following as the conclusion to be drawn thereof:

1. In addition to the existing theories on neutrino oscillations, the present model is an alternative explanation, where these neutrino oscillations are explained by assuming that the massless neutrino is intrinsically coupled to a hypothetical, massive three-state unstable, invisible, unobservable point-particle which is a Dirac zero-rank scalar. The three-state unstableness of this Dirac scalar is what leads to the observed neutrino oscillations.
2. If complex energy states are physically non-permissible and/or forbidden — be they for the case of observable or non-observable particle(s) — then, according to the present model, neutrinos can not be Majorana in nature as this directly leads to complex energy eigenvalues for the Dirac ϕ-particle. On this basis and this alone, one is to reject this and with it, the idea of Majorana neutrinos.

Acknowledgements

We are grateful for the assistance rendered unto us by the National University of Science and Technology's Research Board toward our research endeavours.

Submitted on March 16, 2018

References

1. Einstein A. Zur Elektrodynamik Bewegter Körper. *Annalen der Physik*, 1905, v. 322(10), 891–921.
2. Agafonova A., Aleksandrov A., Altinok O., Ambrosio M. and et al. Observation of a First ν_τ Candidate Event in the OPERA Experiment in the CNGS Beam. *Physics Letters B*, 2010, v. 691(3), 138–145.
3. Ahmad Q. R., Allen R. C. , Andersen T. C., and et al. Measurement of the Rate of $\nu_e + d \rightarrow p + p + e^-$ Interactions Produced by ^8B Solar Neutrinos at the Sudbury Neutrino Observatory. *Phys. Rev. Lett.*, 2001, v. 87, 071301.
4. An F. P., Bai J. Z., Balantekin A. B., Band H. R., and et al. Observation of Electron-Antineutrino Disappearance at Daya Bay. *Phys. Rev. Lett.*, 2012, v. 108, 171803.
5. Fukuda Y., Hayakawa T., Ichihara E., Inoue K., and et al. Evidence for Oscillation of Atmospheric Neutrinos. *Phys. Rev. Lett.*, 1998, v. 81, 1562–1567.
6. Pontecorvo B. Mesonium and anti-Mesonium. *Zh. Eksp. Teor. Fiz.*, 1957, v. 33(2), 549–551. Reproduced and translated in: Pontecorvo, B. Mesonium and Anti-mesonium. *Sov. Phys. JETP*, 1957, v. 6(2), 429–431.
7. Pontecorvo B. Neutrino Experiments and the Problem of Conservation of Leptonic Charge. *Zh. Eksp. Teor. Fiz.*, 1968, v. 53, 1717–1725. Reproduced and translated in: Pontecorvo, B. Neutrino Experiments and the Problem of Conservation of Leptonic Charge. *Sov. Phys. JETP*, 1968, v. 26, 984–988.
8. Davis R., Harmer D. S. and Hoffman K. C. Search for Neutrinos from the Sun. *Phys. Rev. Lett.*, 1968, v. 20, 1205–1209.
9. Murayama H. The Origin of Neutrino Mass. *Physics World (Magazine)*, 2002, May Issue, 35–39.
10. Englert F. and Brout R. Broken Symmetry and the Mass of Gauge Vector Mesons. *Phys. Rev. Lett.*, 1964, v. 13, 321–323.
11. Guralnik G. S., Hagen, C. R. and Kibble T. W. B. Global Conservation Laws and Massless Particles. *Phys. Rev. Lett.*, 1964, v. 13, 585–587.
12. Higgs P. W. Broken Symmetries and the Masses of Gauge Bosons. *Phys. Rev. Lett.*, 1964, v. 13, 508–509.
13. Weyl H. K. H. Gravitation and the Electron. *Proceedings of the National Academy of Sciences*, 1929, v. 15(4), 323–334.
14. Nyambuya G. G. Concerning the Dirac γ-Matrices Under a Lorentz Transformation of the Dirac Equation. *Progress in Physics*, 2018, v. 14, 90–93.
15. Dirac P. A. M. The Quantum Theory of the Electron. *Proc. Roy. Soc. (London)*, 1928, v. A117, 610–612.
16. Dirac P. A. M. The Quantum Theory of the Electron II. *Proc. Roy. Soc. (London)*, 1928, v. A118, 351–361.
17. Weinheimer C. and Zuber K. Neutrino Masses. *Annalen der Physik*, 2013, v. 525(8-9), 565–575.
18. Amsler C., Doser M., Antonelli M., Asner D. M. and et al. Review of Particle Physics. *Physics Letters B*, 2008, v. 667(1), 1–6.
19. Eidelman S., Hayes K. G., Olive K. A., Aguilar-Benitez M., and et al. Review of Particle Physics. *Physics Letters B*, 2004, v. 592(1), 1–5.
20. Majorana E. Theory of the Symmetry of Electrons and Positrons. *Nuovo Cimento*, 1937, v. 5, 171–184.

Global Scaling of Planetary Systems

Hartmut Müller

E-mail: hm@interscalar.com

The paper introduces a scale-invariant model of matter as fractal chain system of oscillating protons and electrons that is applied to the analysis of the solar system and extrasolar planetary systems. Based on global scaling, an explanation of the large number of coincident metric characteristics in different planetary and moon systems is proposed.

Introduction

The formation and evolution of the solar system is caused by very different processes and it is a complex field of research that considers electromagnetic, thermodynamic, hydrodynamic, nuclear physical and chemical factors in their complex interaction. Advanced models were developed [1–5] in the last century which explain essential features of the solar system formation. Gravity is treated as dominant force at macroscopic scales that forms the shape and trajectory (orbit) of astronomical bodies including stars and galaxies. Indeed, if numerous bodies are gravitationally bound to one another, classic models predict long-term highly unstable states that contradict with the astrophysical reality in the solar system.

Furthermore, many metric characteristics of the solar system are not predicted in standard models. A remarkably large number of coincidences are considered to be casual and are not even topics of theoretical research. For example, Mars and Mercury, but also Uranus and Venus have the same surface gravity acceleration. Such dissimilar bodies like Jupiter and Ceres, but also Earth, Mars and Eris have similar rotation periods. Various moons of very different planets in the solar system have the same orbital periods as have various planets in different extrasolar systems like Trappist 1 or Kepler 20.

In this paper we apply our scale-invariant model [6–8] of matter as fractal chain system of oscillating protons and electrons to the analysis of the solar system and extrasolar planetary systems. Based on our hypothesis of global scaling we propose an explanation of the large number of coincidences of the metric characteristics of the systems.

Methods

As result of measurement, real numbers build the bridge that connects theoretical models with the physical reality [9]. The classification of real numbers, in particular the difference between rational and irrational numbers is not only a mathematical task. It is also an essential aspect of stability in real systems. Parameter relations corresponding to rational numbers of small quotients support resonance interactions inside the system and make the system unstable. On the contrary, irrational relations correspond to minimum resonance interaction inside the system and to its stability [10].

Indeed, this stability can be lasting only if a given irrational relation cannot be transformed into a rational by elementary arithmetic operations. In the case of algebraic numbers, an irrational relation of wavelengths can lead to rational relations of surfaces, volumes, masses or energies and nevertheless can make the system unstable.

Transcendental numbers cannot be represented as roots of algebraic equations. Therefore, no elementary arithmetic operation like addition or multiplication can transform a transcendental number into a rational. This is not valid for irrational, but non transcendental numbers, including the so-called golden number $\phi = (\sqrt{5}+1)/2$.

It is remarkable that only continued fractions deliver biunique representations of all real numbers, rational and irrational. Finite continued fractions represent always rational numbers, whereas infinite continued fractions represent irrational numbers. That is why any irrational number can be approximated by finite continued fractions - the convergents which deliver always the best and quickest approximation [11]. It is notable that the best rational approximation of an irrational number by a finite continued fraction is not a task of computation, but only an act of termination of the fractal recursion.

Alas, transcendental numbers can be approximated exceptionally well by rational numbers, because their continued fractions contain large denominators and can be truncated with minimum loss of precision. For instance, the fourth denominator in the simple continued fraction of π = [3; 7, 15, 1, 292, ...] = 3.1415927... is quite big, so that the ratio 355/113 $\approx$ 3.1415929 delivers a very good approximation. Euler's number e = 2.71828... is also transcendental and can be represented as continued fraction with quickly increasing denominators, so that already the ratio 193/71 $\approx$ 2.71831 gives a good approximation.

In the consequence, transcendental numbers define the preferred relations of parameters which sustain the stability of a complex system. In this way, the system avoids destabilizing resonance. At the same time, a good rational approximation can be induced quickly, if resonance interaction is required. Furthermore, if stability is provided concerning all derivatives of a process, Euler's number is the only choice, because of the self-similarity of the natural exponential function regarding its derivatives:

$$\frac{d}{dx}\, e^x = e^x.$$

Property	Electron	Proton
rest mass m	$9.10938356(11)\cdot 10^{-31}$ kg	$1.672621898(21)\cdot 10^{-27}$ kg
energy $E = mc^2$	0.5109989461(31) MeV	938.2720813(58) MeV
angular frequency $\omega = E/\hbar$	$7.76344071\cdot 10^{20}$ Hz	$1.42548624\cdot 10^{24}$ Hz
angular oscillation period $\tau = 1/\omega$	$1.28808867\cdot 10^{-21}$ s	$7.01515\cdot 10^{-25}$ s
angular wavelength $\lambda = c/\omega$	$3.8615926764(18)\cdot 10^{-13}$ m	$2.1030891\cdot 10^{-16}$ m
angular acceleration $a = c/\omega$	$2.327421\cdot 10^{29}$ ms^{-2}	$4.2735\cdot 10^{32}$ ms^{-2}

Table 1: The basic set of physical properties of the electron and proton. (c is the speed of light in a vacuum, $\hbar$ is the reduced Planck constant, k_B is the Boltzmann constant). Data taken from Particle Data Group [20]. Frequencies, oscillation periods, accelerations and the proton wavelength are calculated.

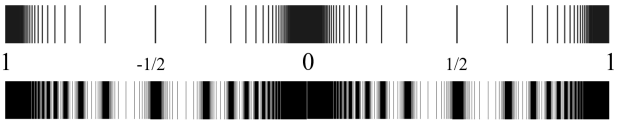

Fig. 1: The distribution of eigenvalues of $\mathcal{F}$ for $k = 1$ (above) and for $k = 2$ (below) in the range $-1 \leqslant \mathcal{F} \leqslant 1$.

In [12] we have shown that the set of natural frequencies (eigenstates) of a fractal chain system of harmonic oscillators can be described as set (1) of finite continued fractions $\mathcal{F}$, which are natural logarithms:

$$\mathcal{F} = \ln(\omega_{jk}/\omega_{00}) = [n_{j0}; n_{j1}, n_{j2}, \ldots, n_{jk}] \qquad (1)$$

where ω_{jk} is the set of angular frequencies and ω_{00} is the fundamental frequency of the set. The denominators are integer: $n_{j0}, n_{j1}, n_{j2}, \ldots, n_{jk} \in \mathbb{Z}$, the cardinality $j \in \mathbb{N}$ of the set and the number $k \in \mathbb{N}$ of layers are finite. In the canonical form, all numerators equal 1.

Any finite continued fraction represents a rational number. Therefore, all frequency ratios ω_{jk}/ω_{00} in (1) are irrational, because for rational exponents the natural exponential function is transcendental [13]. This circumstance provides for high stability of the eigenstates (1) of a chain system of harmonic oscillators because it prevents resonance interaction between the elements of the system. In [14–16] we have applied continued fractions of the type (1) as criterion of stability in engineering.

In the canonical form, the distribution density of eigenvalues of finite continued fractions reaches maxima near reciprocal integers 1, 1/2, 1/3, 1/4, ... which are the attractor points in the fractal set $\mathcal{F}$ of natural logarithms (fig. 1).

Shorter continued fractions (1) with smaller denominators correspond with more stable eigenstates of the chain system, because the logarithmic distance between their eigenvalues is maximum. Considering the existence of two complementary fractals on the sets of rational and irrational numbers accordingly [17], the probability that small variations (fluctuations) lead to coincidences between irrational and rational numbers of small quotients is minimum. Therefore, integer and half logarithms represent the most stable eigenstates.

Already in 1950 Gantmacher and Krein [18] have demonstrated that continued fractions are solutions of the Euler-Lagrange equation for low amplitude harmonic oscillations in simple chain systems. Terskich [19] generalized this method for the analysis of oscillations in branched chain systems. In [6] the continued fraction method was extended to the analysis of chain systems of harmonic quantum oscillators.

In the case of harmonic quantum oscillators, the continued fractions (1) define not only fractal sets of natural angular frequencies ω_{jk}, angular accelerations $a_{jk} = c \cdot \omega_{jk}$, oscillation periods $\tau_{jk} = 1/\omega_{jk}$ and wavelengths $\lambda_{jk} = c/\omega_{jk}$ of the chain system, but also fractal sets of energies $E_{jk} = \hbar \cdot \omega_{jk}$ and masses $m_{jk} = E_{jk}/c^2$ which correspond with the eigenstates of the system [8].

In this way, the continued fractions (1) generate the fundamental fractal $\mathcal{F}$ of eigenstates in chain systems of harmonic quantum oscillators.

As the cardinality and number of layers of the continued fractions (1) are finite but not limited, in each point of the space-time occupied by the chain system of harmonic quantum oscillators the scalar $\mathcal{F}$ is defined. Therefore, any chain system of harmonic quantum oscillators can be seen as source of the fractal scalar field $\mathcal{F}$, the fundamental field of the system. The scalar potential difference $\Delta\mathcal{F}$ of sequent equipotential surfaces at a given layer k is defined by the difference of continued fractions (1). In the canonical form:

$$\Delta\mathcal{F} = \mathcal{F}(\mathrm{j,k}) - \mathcal{F}(\mathrm{j+1,k}) = \\ = [n_{j0}; n_{j1}, n_{j2}, \ldots, n_{jk}] - [n_{j0}; n_{j1}, n_{j2}, \ldots, n_{j+1,k}].$$

In [7] we have introduced a scale-invariant model of matter as fractal chain system of harmonically oscillating protons and electrons that generates the fundamental field $\mathcal{F}$. Normal matter is formed by nucleons and electrons because they are exceptionally stable quantum oscillators. In the concept of isospin, proton and neutron are viewed as two states of the

same quantum oscillator. Furthermore, they have similar rest masses. However, a free neutron decays into a proton, an electron and antineutrino within 15 minutes while the lifespans of the proton and electron top everything that is measurable, exceeding 10^{29} years [20].

The exceptional stability of electron and proton predestinate their physical characteristics as fundamental units. Table 1 shows the basic set of electron and proton units that can be considered as a fundamental metrology. In [8] was shown that it is compatible with Planck units [21].

Within our model, the proton-to-electron ratio (tab. 1) is caused by the fundamental field $\mathcal{F}$. In fact, the natural logarithm is close to rational:

$$\ln \frac{938.2720813 \text{ MeV}}{0.5109989461 \text{ MeV}} \approx 7 + \frac{1}{2}.$$

As a consequence, the fundamental field of the proton is complementary to that of the electron, because integer logarithms of the proton $\mathcal{F}$ correspond to half logarithms of the electron $\mathcal{F}$ and vice versa, so that the scaling factor $\sqrt{e}$ connects similar equipotential surfaces of the proton field with those of the electron field in alternating sequence [8].

We hypothesize that scale invariance of the fundamental field $\mathcal{F}$ calibrated on the physical properties of the proton and electron (tab. 1) is a universal characteristic of organized matter and criterion of stability. This hypothesis we have called Global Scaling [22].

Results

Within our scale-invariant model of matter [7], atoms and molecules emerge as eigenstates of stability in fractal chain systems of harmonically oscillating protons and electrons.

Andreas Ries [23] demonstrated that this model allows for the prediction of the most abundant isotope of a given chemical element. From this point of view, any physical body, being solid, liquid or gas can be seen as fractal chain system of oscillating molecules, atoms, ions, protons and electrons that follows the fundamental field $\mathcal{F}$.

Therefore, in the framework of our fractal model of matter, the fundamental field $\mathcal{F}$ affects any type of physical interaction, regardless of its complexity.

In [24] we applied our model to the analysis of gravimetric and seismic characteristics of the Earth and could show that our estimations [25] correspond well with established empiric models of the Earth interior.

In [26] we did demonstrate that the vertical sequence of stable atmospheric layers corresponds with the sequence of main spatial equipotential surfaces of the fundamental field $\mathcal{F}$, not only at Earth, but also at Venus, Mars and Titan.

In [27] was demonstrated that the mass distribution in the solar system and the mass distribution of elementary particles follow the same scaling law. In [8] was shown that the distribution of rotation and orbital periods in the solar system corresponds with main temporal equipotential surfaces of the fundamental field $\mathcal{F}$.

For verification of Global Scaling in this paper we consider only direct measurements and refer on data that should not contain systematic errors. As such data we consider the rotation and orbital periods, but also the majority of estimated body radii and orbital distances in the solar system.

Fig. 2 shows the correspondence of orbital periods for planets and planetoids of the solar system with equipotential surfaces of the fundamental field $\mathcal{F}$. Tab. 2 contains the corresponding data. Integer numbers in the bottom of the graphic are natural logarithms of main equipotential surfaces $[n_0; \infty]$ of the fundamental field $\mathcal{F}$ calibrated on the proton (bold) and electron (thin). For example, Jupiter's orbital period [28] corresponds with the main temporal equipotential surface [66; ∞] of the fundamental field $\mathcal{F}$ calibrated on the oscillation period of the electron:

$$\ln\left(\frac{T_{\text{Jupiter}}}{\tau_{\text{electron}}}\right) = \ln\left(\frac{4332.59 \cdot 86400 \text{ s}}{2\pi \cdot 1.28808867 \cdot 10^{-21} \text{ s}}\right) = 66.00$$

The logarithmic scale in fig. 2 covers a range of 79 to 235000 days $\approx$ 640 years.

Fig. 3 shows the correspondence of orbital periods for moons of the solar system and planets of the systems Trappist 1 [29] and Kepler 20 [30] with temporal equipotential surfaces of the fundamental field $\mathcal{F}$. Tab. 3 and 4 contain the corresponding data. It is remarkable that the orbits of Trappist 1b, c, d and e correspond with main equipotential surfaces of the fundamental field $\mathcal{F}$. This is also valid for Kepler 20b, c, d and e and for many other exoplanetary systems we did not include in this paper.

Because of the complementarity of the fundamental field of the proton to that of the electron, equipotential surfaces of the type $[n_{j0}; \pm 2]$ coincide always with complementary

body	**orbital period T, d**	**ln (T/2$\pi\,\tau_e$)**	$\mathcal{F}$
Eris (P)	203830	69.86	[70; -6]
Pluto (P)	90560	69.04	[69; ∞]
Neptune	60182	68.64	[69; -3]
Uranus	30688.5	67.96	[68; ∞]
Saturn	10759.22	66.91	[67; ∞]
Jupiter	4332.59	66.00	[66; ∞]
Ceres (P)	1681.63	65.06	[65; ∞]
Mars	686.971	64.16	[64; 6]
Earth	365.256363	63.53	[63; 2]
Venus	224.701	63.04	[65; ∞]
Mercury	87.9691	62.12	[62; 6]

Table 2: Natural logarithms of the orbital period-to-electron oscillation period ratios for planets and heaviest planetoids (P) of the solar system and the corresponding equipotential surfaces of the fundamental field $\mathcal{F}$. Data: [28]

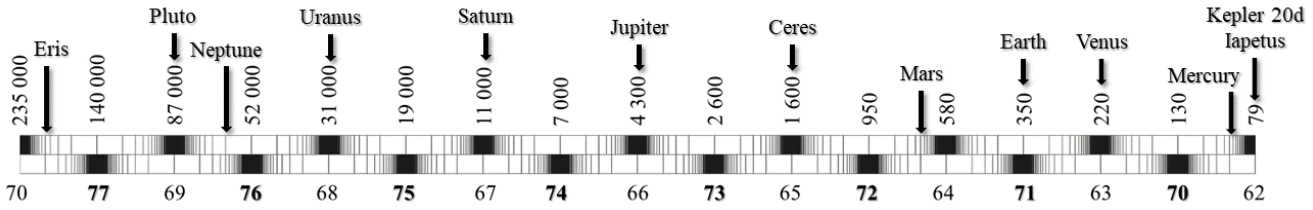

Fig. 2: Correspondence of orbital periods of planets and planetoids of the solar system with temporal equipotential surfaces of the fundamental field $\mathcal{F}$. Integers in the bottom of the graphic are natural logarithms of main equipotential surfaces $[n_{j0}; \infty]$ of the fundamental field $\mathcal{F}$ calibrated on the proton (bold) and electron (thin). The logarithmic scale covers a range of 79 to 235 000 days ≈ 640 years. Tab. 2 contains the corresponding data.

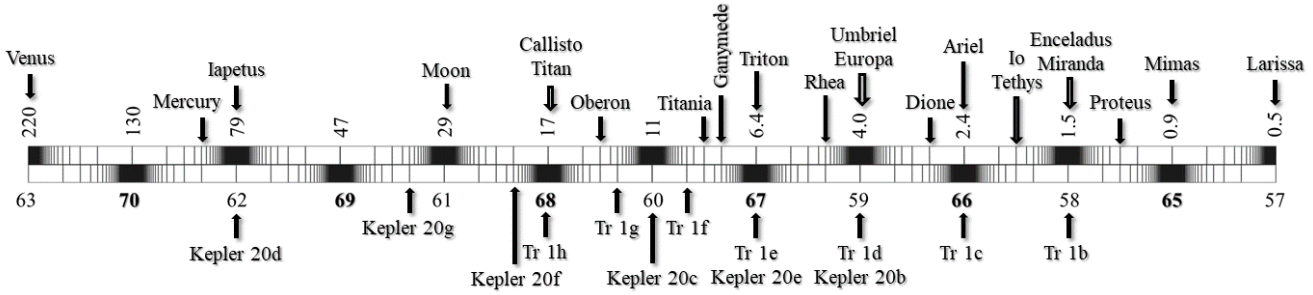

Fig. 3: Correspondence of orbital periods of moons of the solar system and planets of the systems Trappist 1 and Kepler 20 with temporal equipotential surfaces of the fundamental field $\mathcal{F}$. The logarithmic scale covers a range of 0.5 to 220 days. Tab. 3 and 4 contain the corresponding data.

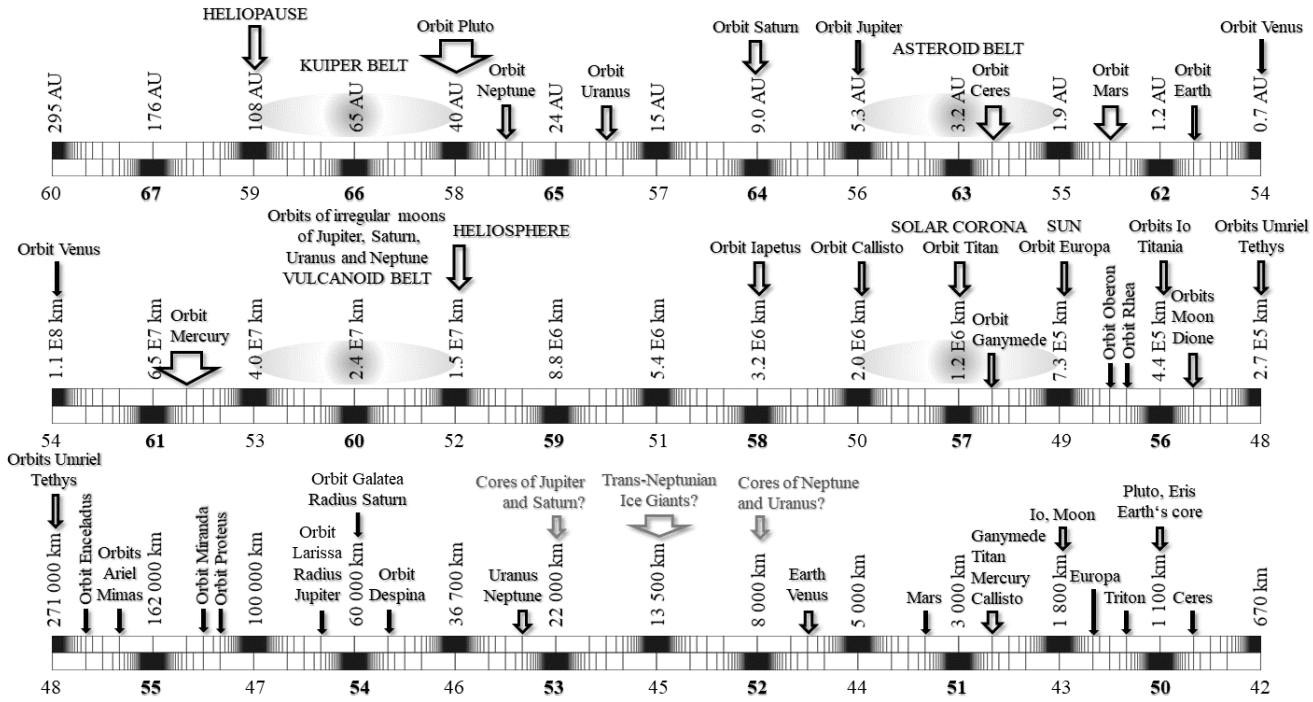

Fig. 4: Correspondence of metric characteristics of large structures in the solar system with spatial equipotential surfaces of the fundamental field $\mathcal{F}$. The logarithmic scale covers a range of 670 km to 295 AU. The width of the arrows is a measure of data dispersion or eccentricity of an orbit. Grey arrows and descriptions are hypothetical. The corresponding data are published in [8, 25].

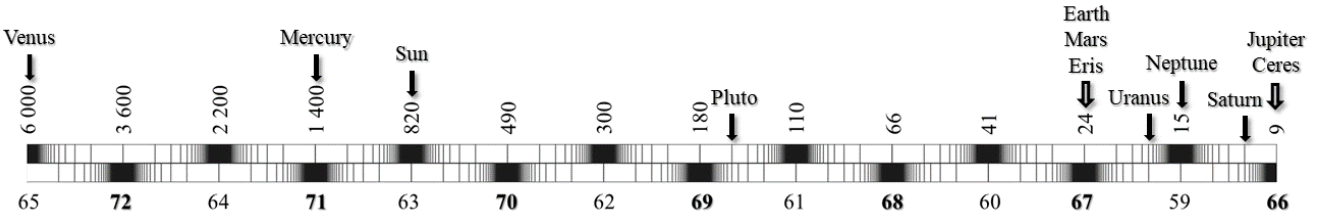

Fig. 5: Correspondence of rotation periods of planets and some planetoids of the solar system with temporal equipotential surfaces of the fundamental field $\mathcal{F}$. The logarithmic scale covers a range of 9 to 6000 hours. Tab. 5 contains the corresponding data.

main equipotential surfaces $[n_{j0}; \infty]$, so that the remaining orbits correspond mostly with equipotential surfaces of the type $[n_{j0}; \pm 3]$. This distribution is a consequence of the fractal hierarchy 1/2, 1/3, 1/4, ... of stability layers (see fig. 1) given by the continued fraction (1) of natural logarithms.

Fig. 4 shows the correspondence of metric characteristics of large structures in the solar system with spatial equipotential surfaces of the fundamental field $\mathcal{F}$. The corresponding data are published in [8, 25]. For example, the visible equatorial radius of Saturn [32] corresponds with the main spatial equipotential surface $[54; \infty]$ of the fundamental field $\mathcal{F}$ calibrated on the wavelength of the proton (tab. 1):

$$\ln\left(\frac{r_{\text{Saturn}}}{\lambda_{\text{proton}}}\right) = \ln\left(\frac{6.0268 \cdot 10^{7}\ \text{m}}{2.1030891 \cdot 10^{-16}\ \text{m}}\right) = 54.01$$

The logarithmic scale in fig. 4 covers a range of 670 km to 295 AU. In general, the width of the arrows is a measure of data dispersion or eccentricity of an orbit. Grey arrows and descriptions are hypothetical.

Fig. 4 shows that the orbits of Venus, Jupiter, Saturn and Pluto correspond with main equipotential surfaces $[n_{j0}; \infty]$ of the fundamental field $\mathcal{F}$.

It is notable that Jupiter's orbit represents the logarithmic mean between the orbits of Venus and Pluto. The orbits of

moon of	**orbital period T, d**	**ln (T/2π τ_e)**	$\mathcal{F}$
EARTH			
Moon	27.321661	60.94	[61; ∞]
JUPITER			
Callisto	16.689	60.45	[60; 2]
Ganymede	7.1546	59.61	[60; -3]
Europa	3.5512	58.91	[60; ∞]
Io	1.7691	58.21	[58; 4]
SATURN			
Iapetus	79.3215	62.00	[62; ∞]
Titan	15.945	60.41	[60; 2]
Rhea	4.5182	59.14	[59; 6]
Dione	2.7369	58.65	[59; -3]
Tethys	1.8878	58.26	[58; 4]
Enceladus	1.3702	57.95	[58; ∞]
Mimas	0.942	57.57	[57; 2]
URANUS			
Oberon	13.4632	60.24	[60; 4]
Titania	8.7062	59.78	[60; -4]
Umbriel	4.144	59.05	[59; ∞]
Ariel	2.52	58.54	[58; 2]
Miranda	1.4135	57.98	[58; ∞]
NEPTUNE			
Nereid	360.1362	63.52	[63; 2]
Triton	5.877	59.41	[59; 2]
Proteus	1.1223	57.75	[58; -4]
Larissa	0.555	57.04	[57; ∞]

Table 3: Natural logarithms of the orbital period-to-electron oscillation period ratios for the largest moons of in the solar system and the corresponding equipotential surfaces of the fundamental field $\mathcal{F}$. Data: [31]

planet of	**orbital period T, d**	**ln (T/2π τ_e)**	$\mathcal{F}$
TRAPPIST 1			
H	18.767953	60.56	[60; 2]
G	12.354473	60.15	[60; 6]
F	9.205585	59.86	[60; ∞]
E	6.099615	59.45	[59; 2]
D	4.04961	59.03	[59; ∞]
C	2.4218233	58.51	[58; 2]
B	1.51087081	58.04	[58; ∞]
KEPLER 20			
D	77.61130017	61.98	[62; ∞]
G	34.94	61.17	[61; 6]
F	19.57758478	60.61	[61; -3]
C	10.85409089	60.01	[60; ∞]
E	6.09852281	59.45	[59; 2]
B	3.69611525	58.94	[59; ∞]

Table 4: Natural logarithms of the orbital period-to-electron oscillation period ratios for exoplanets of the systems Trappist 1 and Kepler 20 with the corresponding equipotential surfaces of the fundamental field $\mathcal{F}$. Data: [29, 30]

body	rotation period τ, h	ln (τ/τ_p)	$\mathcal{F}$
Venus	5816.66728	72.48	[72; 2]
Mercury	1407.5	71.05	[71; ∞]
Sun	823.346	70.51	[70; 2]
Pluto (P)	152.87496	68.83	[69; -6]
Eris (P)	25.9	67.06	[67; ∞]
Mars	24.62278	67.01	[67; ∞]
Earth	23.93444	66.98	[67; ∞]
Uranus	17.24	66.66	[67; -3]
Neptune	16.11	66.57	[66; 2]
Saturn	10.55	66.16	[66; 6]
Jupiter	9.925	66.09	[66; ∞]
Ceres (P)	9.07417	66.01	[66; ∞]

Table 5: Natural logarithms of the rotation period-to-proton oscillation period ratios for planets and heaviest planetoids (P) of the solar system and the corresponding equipotential surfaces of the fundamental field $\mathcal{F}$. Data: [28].

Mercury, Earth, Mars, Ceres correspond all with equipotential surfaces of the type $[n_{j0}; \pm 3]$. This is valid also for the orbits of Ganymede, Rhea, Dione and the Moon. The orbits of Uranus and Neptune correspond with equipotential surfaces $[n_{j0}; \pm 4]$.

The orbits of Callisto, Europa, Io and Titan correspond with main equipotential surfaces $[n_{j0}; \infty]$. This is also valid for the orbits of Tethys, Umbriel, Titania and Iapetus.

The radius of the photosphere of the Sun and the visible radius of Saturn correspond with main spatial equipotential surfaces $[n_{j0}; \infty]$.

The visible radii of Jupiter, Uranus and Neptune, but also the radii of the solid bodies Mars, Mercury, Ganymede, Titan, Callisto, Europa and Ceres correspond all with equipotential surfaces of the type $[n_{j0}; \pm 3]$. Only the radii of Earth and Venus correspond with equipotential surfaces $[n_{j0}; \pm 4]$. The radii of Io, the Moon, Pluto and Eris correspond with main equipotential surfaces $[n_{j0}; \infty]$.

It is remarkable that the orbit of Europa coincides with the radius of the Sun (boundary of the photosphere), the orbit of Galatea (Neptune VI) coincides with Saturn's radius (stratopause) and the orbit of Larissa (Neptune VII) with the radius of Jupiter.

Fig. 5 shows the correspondence of rotation periods of planets and large planetoids of the solar system with temporal equipotential surfaces of the fundamental field $\mathcal{F}$. The logarithmic scale in fig. 5 covers a range of 9 to 6000 hours. Tab. 5 contains the corresponding data.

The rotation periods of Venus, Mercury, the Sun, Earth, Mars, Eris, Neptune, Jupiter and Ceres coincide with main equipotential surfaces while the rotation periods of Saturn, Uranus and Pluto correspond with temporal equipotential surfaces of the type $[n_{j0}; \pm 3]$.

Although the rotation of Venus [31] is retrograde, its rotation period of 5816.66728 hours fits perfectly with the main temporal equipotential surface $[65; \infty]$ of the electron $\mathcal{F}$:

$$\ln\left(\frac{\tau_{\text{Venus}}}{\tau_{\text{electron}}}\right) = \ln\left(\frac{5816.66728 \cdot 3600 \text{ s}}{1.28808867 \cdot 10^{-21} \text{ s}}\right) = 64.96$$

Concluding our analysis of the solar system and exoplanetary systems we assume that planetary systems preferentially occupy main equipotential surfaces of the fundamental field $\mathcal{F}$. This circumstance makes possible the calculation of remaining orbits in exoplanetary systems.

Conclusion

The logarithmic projection of the fundamental field $\mathcal{F}$ reveals the remarkable scale symmetry of the solar system and suggests that it could hardly be the consequence of random collisions. Within our cosmological hypothesis of Global Scaling [8], the formation of the solar system as well as exoplanetary systems can be understood in terms of harmonic oscillations in chain systems.

Movement along equipotential surfaces requires no work. That's why stable orbits correspond with equipotential surfaces of the fundamental field $\mathcal{F}$ and orbital eccentricity is always limited by neighboring equipotential surfaces [8].

Equipotential surfaces of the fundamental field $\mathcal{F}$ define not only stable planetary orbits, but also the metric characteristics of stratification layers in planetary atmospheres [26] and lithospheres [25]. From this point of view, metric characteristics of stable structures origin from the same fundamental field $\mathcal{F}$ and different only in scale.

The conceptual core of our model are harmonic oscillations in chain systems. These oscillations remain stable only if resonance interaction inside the system can be avoided. As solution survives a logarithmically fractal set (1) of transcendental frequency ratios. Note it is not a simple power law.

We suppose that basic power rules like the Titius-Bode [33], Dermott's rule [34] as well as the discovered golden number [35] and Fibonacci ratios [36] in solar planetary and satellite systems and in exoplanetary systems reflect a local feature of the fundamental field $\mathcal{F}$, because $\sqrt{e}$ = 1,648... is close to the golden number ϕ = 1.618... and for small exponents, the rounded up powers of the square root of Euler's number deliver the sequence of Fibonacci numbers.

Another essential aspect of our cosmological model [8] is Global Scaling, the hypothesis that in the universe there is only one global fundamental field $\mathcal{F}$. In fact, it was demonstrated that scale relations in particle physics [6, 7, 37] and nuclear physics [23, 38, 39], astrophysics [8, 27, 40–43], geophysics [25, 26] and biophysics [44, 45] follow always the same fundamental field $\mathcal{F}$ calibrated on the proton and electron, without any additional or particular settings. The universality and unity of the fundamental field $\mathcal{F}$ might signify that everything in the universe is part of one giant oscillating chain system.

Acknowledgements

The author is thankful to Oleg Kalinin, Alexej Petrukhin, Viktor Panchelyuga and Erwin Müller for valuable discussions and to Leili Khosravi for permanent support on all stages of the study.

Submitted on March 27, 2018

References

1. Williams I. O., Cremin A.W. A survey of theories relating to the origin of the solar system. *Qtly. Rev. RAS*, 1968, v. 9, 40–62.
2. Alfven H. Band Structure of the Solar System. Dermot S.F. Origin of the Solar System. pp. 41–48. Wiley, (1978).
3. Woolfson M.M. The Solar System: Its Origin and Evolution. *Journal of the Royal Astronomical Society*, 1993, v. 34, 1–20.
4. Van Flandern T. Our Original Solar System - a 21st Century Perspective. MetaRes. Bull. 17: 2–26, (2008). D21, 475–491, 2000.
5. Woolfson M. M. Planet formation and the evolution of the Solar System. arXiv:1709.07294, (2017).
6. Müller H. Fractal Scaling Models of Natural Oscillations in Chain Systems and the Mass Distribution of Particles. *Progress in Physics*, 2010, no. 3, 61–66.
7. Müller H. Emergence of Particle Masses in Fractal Scaling Models of Matter. *Progress in Physics*, 2012, v. 4, 44–47.
8. Müller H. Scale-Invariant Models of Natural Oscillations in Chain Systems and their Cosmological Significance. *Progress in Physics*, 2017, no. 4, 187–197.
9. International Vocabulary of Metrology – Basic and General Concepts and Associated Terms. International Bureau of Weights and Measures, 2008, p. 16.
10. Dombrowski K. Rational Numbers Distribution and Resonance. *Progress in Physics*, 2005, no. 1, 65–67.
11. Khintchine A.Ya. Continued fractions. University of Chicago Press, Chicago, 1964.
12. Müller H. Fractal Scaling Models of Resonant Oscillations in Chain Systems of Harmonic Oscillators. *Progress in Physics*, 2009, no. 2, 72–76.
13. Hilbert D. Über die Transcendenz der Zahlen e und π. *Mathematische Annalen*, 1893, v. 43, 216–219.
14. Müller H. The general theory of stability and objective evolutionary trends of technology. Applications of developmental and construction laws of technology in CAD. Volgograd, VPI, 1987 (in Russian).
15. Müller H. Superstability as a developmental law of technology. Technology laws and their Applications. Volgograd-Sofia, 1989.
16. Müller H., Otte R. Verfahren zur Stabilisierung von technischen Prozessen. PCT, WO 2005/071504 A2.
17. Panchelyuga V. A., Panchelyuga M. S. Resonance and Fractals on the Real Numbers Set. *Progress in Physics*, 2012, no. 4, 48–53.
18. Gantmacher F.R., Krein M.G. Oscillation matrixes, oscillation cores and low oscillations of mechanical systems. Leningrad, 1950.
19. Terskich V.P. The continued fraction method. Leningrad, 1955.
20. Olive K.A. et al. (Particle Data Group), *Chin. Phys. C*, 2016, v. 38, 090001. Patrignani C. et al. (Particle Data Group), *Chin. Phys. C*, 2016, v. 40, 100001.
21. Planck M. Über Irreversible Strahlungsvorgänge. *Sitzungsberichte der Königlich Preußischen Akademie der Wissenschaften*, 1899, v. 1, 479–480.
22. Müller H. Scaling as Fundamental Property of Natural Oscillations and the Fractal Structure of Space-Time. Foundations of Physics and Geometry. Peoples Friendship University of Russia, 2008 (in Russian).
23. Ries A. Qualitative Prediction of Isotope Abundances with the Bipolar Model of Oscillations in a Chain System. *Progress in Physics*, 2015, v. 11, 183–186.
24. Müller H. Gravity as Attractor Effect of Stability Nodes in Chain Systems of Harmonic Quantum Oscillators. *Progress in Physics*, 2018, v. 14, 19–23.
25. Müller H. Quantum Gravity Aspects of Global Scaling and the Seismic Profile of the Earth. *Progress in Physics*, 2018, v. 14, 41–45.
26. Müller H. Global Scaling of Planetary Atmospheres. *Progress in Physics*, 2018, v. 14, 66–70.
27. Müller H. Fractal scaling models of natural oscillations in chain systems and the mass distribution of the celestial bodies in the Solar System. *Progress in Physics*, 2010, no. 4, 44–47.
28. Jupiter Fact Sheet. nssdc.gsfc.nasa.gov
29. Gillon M. et al. Seven temperate terrestrial planets around the nearby ultracool dwarf star TRAPPIST-1. Nature, 2017, 21360.
30. Hand E. Kepler discovers first Earth-sized exoplanets. Nature, 2011, 9688.
31. Venus Fact Sheet. nssdc.gsfc.nasa.gov
32. Saturn Fact Sheet. nssdc.gsfc.nasa.gov
33. Hayes W. Fitting random stable solar systems to Titius-Bode laws. arXiv: astro-ph/9710116v1 10 Oct 1997.
34. Dermott S.F. On the origin of commensurabilities in the solar system - II: The orbital period relation. *Mon. Not. R. Astron. Soc.*, 1968, v. 141(3), 363–376.
35. Butusov K. P. The Golden Ratio in the Solar System. Problems of Cosmological Research, v. 7, Moscow – Leningrad, 1978 (in Russian).
36. Pletser V. Orbital Period Ratios and Fibonacci Numbers in Solar Planetary and Satellite Systems and in Exoplanetary Systems. arXiv:1803.02828 [physics.pop-ph], 2018.
37. Ries A., Fook M. Fractal Structure of Nature's Preferred Masses: Application of the Model of Oscillations in a Chain System. *Progress in Physics*, 2010, no. 4, 82–89.
38. Ries A. A Bipolar Model of Oscillations in a Chain System for Elementary Particle Masses. *Progress in Physics*, 2012, no. 4, 20–28.
39. Ries A. The Radial Electron Density in the Hydrogen Atom and the Model of Oscillations in a Chain System. *Progress in Physics*, 2012, no. 3, 29–34.
40. Müller H. Scaling of Body Masses and Orbital Periods in the Solar System. *Progress in Physics*, 2015, no. 2, 133–135.
41. Müller H. Scaling of Moon Masses and Orbital Periods in the Systems of Saturn, Jupiter and Uranus. *Progress in Physics*, 2015, no. 2, 165–166.
42. Müller H. Scaling of body masses and orbital periods in the Solar System as consequence of gravity interaction elasticity. Abstracts of the XII. International Conference on Gravitation, Astrophysics and Cosmology, dedicated to the centenary of Einstein's General Relativity theory. Moscow, PFUR, 2015.
43. Müller H. Global Scaling as Heuristic Model for Search of Additional Planets in the Solar System. *Progress in Physics*, 2017, no. 4, 204–206.
44. Müller H. Chain Systems of Harmonic Quantum Oscillators as a Fractal Model of Matter and Global Scaling in Biophysics. *Progress in Physics*, 2017, no. 4, 231–233.
45. Müller H. Astrobiological Aspects of Global Scaling. *Progress in Physics*, 2018, v. 14, 3–6.

Progress in Physics is an American scientific journal on advanced studies in physics, registered with the Library of Congress (DC, USA): ISSN 1555-5534 (print version) and ISSN 1555-5615 (online version). The journal is peer reviewed and listed in the abstracting and indexing coverage of: Mathematical Reviews of the AMS (USA), DOAJ of Lund University (Sweden), Scientific Commons of the University of St.Gallen (Switzerland), Open-J-Gate (India), Referential Journal of VINITI (Russia), etc. Progress in Physics is an open-access journal published and distributed in accordance with the Budapest Open Initiative: this means that the electronic copies of both full-size version of the journal and the individual papers published therein will always be accessed for reading, download, and copying for any user free of charge. The journal is issued quarterly (four volumes per year).

Electronic version of this journal: http://www.ptep-online.com

Postal address:
Department of Mathematics and Science, University of New Mexico,
705 Gurley Avenue, Gallup, NM 87301, USA